



POSTERS SESSION I

- 1**
Gamma Scintillator System Enhancement for Neutron Detection using Boron Carbide for Homeland Security
Yuval Ben-Galim¹, Udi Wengrowicz², Itzhak Orion¹, Avi Raveh³
¹*Department of Nuclear Engineering, Ben Gurion University (BGU) of the Negev, Israel*
²*NRC-Negev, Israel*
³*Advanced Coatings Center, Rotem Industries Ltd, Israel*
- 2**
Zero Time of Transitory Nuclear Events Derived by Parent-Daughter Systems
Yoram Nir-El
Reut, Israel
- 3**
Optimized Activity Concentration Monitoring System for Ventilation Duct at Positron Emitters Production Center
Eran Vax¹, Vlad Bronfenmacher², Amir Broide¹, Dimitry Ginzburg², Vitaly Pushkarsky², Lawrence Kaplan², Tzahi Mazor¹, Yagil Kadmon¹, Alon Osovizky²
¹*NRCN, Israel*
²*ROTEM Industries Ltd., Israel*
- 4**
Flattening the Energy Response of a Scintillator Based Gamma Dose Rate Meter Coupled to SiPM
Y. Knafo¹, A. Manor¹, D. Ginzburg¹, M. Ellenbogen¹, A. Osovizky¹, U. Wengrowicz², M. Ghelman², R. Seif², T. Mazor², Y. Kadmon², Y. Cohen²
¹*ROTEM Industries Ltd., Beer-Sheva, Israel*
²*Nuclear Research Center-Negev, Beer-Sheva, Israel*
- 5**
Neutron Dose Measurement Using a Cubic Moderator
M. Sheinfeld¹, T. Mazor¹, Y. Cohen¹, Y. Kadmon¹, I. Orion²
¹*Electronics R&D, NRCN, Israel*
²*Ben Gurion University of the Negev, Beer-Sheva, Israel*
- 6**
Composites Based on Fly Ash and Clay
Emilija Fidancevska¹, Vojo Jovanov¹, Biljana Angusheva¹, Vineta Srebrenkoska²
¹*Faculty of Technology and Metallurgy, Ss Cyril and Methodius University, Macedonia*
²*Faculty of Technology, Goce Delcev University, Macedonia*
- 7**
Glass Ceramics Fabricated from Coal Fly Ash and Waste Glass
Biljana Angjusheva¹, Vojo Jovanov¹, Vineta Srebrenkoska², Emilija Fidancevska¹
¹*Faculty of Technology and Metallurgy, Ss Cyril and Methodius University, Macedonia*
²*Faculty of Technology, Goce Delcev University, Macedonia*
- 8**
Narrow Lead Aprons under Medical Fluoroscopy Procedures
Avi Ben-Shlomo
Safety Division, Soreq NRC, Israel
- 9**
Medical Staff X-Ray Dose Reduction by Changing the Patient Examination Side
Avi Ben-Shlomo
Safety Division, Soreq NRC, Israel
- 10-20**
"ORCHID" Project

- 1**
DNA Topoisomerase-I Inhibition due to Exposure to X-Rays
Rotem Daudee¹, Rafi Gonen¹, Uzi German¹, Itzhak Orion², Esther Priel²
¹*Nuclear Research Center Negev, Israel*
²*Ben-Gurion University of the Negev, Israel*
- 2**
A Program for Follow-Up and Quality Assurance of Electret Results
Beny Sarusy¹, Shmuel Levinson¹, Natan Lavi², Uzi German¹
¹*NRCN, Israel*
²*Environmental Lab, Ben-Gurion University of the Negev, Beer Sheva, Israel*
- 3**
Application of the "GammaGen" Computer Code for NORM Synthetic Spectra Analysis
Beny Sarusi¹, Shmuel Levinson¹, Uzi German¹, Sergey Antropov², Konstantin Kovler³
¹*NRCN, Israel*
²*Amplituda, Israel*
³*Technion - Israel Institute of Technology, Haifa 32000, Israel*
- 4**
Matrix Materials for Preparation of Marinelli Calibration Standards
Shmuel Levinson¹, Natan Lavi², Uzi German¹
¹*NRCN, Israel*
²*Environmental Lab BGU, Israel*
- 5**
Radioactivity in Soils and Foodstuff Samples in Israel
Shmuel Levinson¹, Natan Lavi², Hisham Nassar³, Uzi German¹
¹*NRCN, Israel*
²*Environmental Lab BGU, Israel*
³*Ministry of Environmental Protection, Israel*
- 6**
Using Cherenkov Counting For Fast Determination of ⁹⁰Sr/⁹⁰Y Activity in Milk
Shimon Tsroya¹, Bella Dolgin¹, Uzi German¹, Omer Pelled¹, Zeev Benjamin Alfassi²
¹*NRCN, Israel*
²*Ben-Gurion University of the Negev, Israel*
- 7**
Study of Cleanup Procedures for Contaminated Area: Examination of Rubidium as a Surrogate to Cesium
Ofra Paz Tal, Ronen Bar Ziv, Roni Hakmon, Eitan Borojovich, Andrey Nikoloski, Tsion Ohaion, Rinat (Yanosh) Levi, Ilan Yaar
Nuclear Research Center Negev, Israel
- 8**
A Computerized QC Analysis of TLD Glow Curves for Personal Dosimetry Measurements Using TagQC Program
Sabi Primo¹, Hanan Datz¹, Amit Dar²
¹*Radiation Safety Division, Soreq Nuclear Research Center, Israel*
²*Empiric Technologies consulting, Israel*
- 9**
Electronic and Magnetic Properties of NpNi5
 A. Hen^{1,2}, E. Colineau¹, R. Eloirdi¹, J. - C. Griveau¹, J. - P. Sanchez⁴, A. B. Shick^{1,5}, I. Halevy^{2,3}, I. Orion², R. Caciuffo¹
¹*Institute for Transuranium Elements, European Commission, Joint Research Centre, Germany*
²*Nuclear Engineering Department, Ben Gurion University, Israel*
³*Physics Department, Nuclear Research Center Negev, Israel*
⁴*UMR-E CEA/UJF-Grenoble, SPSMS, UMR-E, France*
⁵*Academy of Sciences of the Czech Republic, Institute of Physics, Czech Republic*
- 10**
Radioactive Contamination Estimation from micro-copters or helicopter Airborne survey: Simulation and Real Measurements
Itzhak Halevy, M. Ghelman, Y. Yehuda-Zada, A. Manor, A. Sharon, I. Yaar
Physics Department, Nuclear Research Center – Negev, Israel

11

Prospects for the SMR Technology

Barak Tavron, Dan Rene Marouani
Israel Electric Corporation, Israel

12

Mechanical properties characterization for a cylindrical fuel clad using the segmented expanding cone-mandrel (SEM) method

Matan Tubul, Barak Ostraich, Eugene Shwageraus,
Nuclear Engineering, Ben Gurion University, Israel

13

Ground Shock Resistant of Buried Nuclear Power Plant Facility

David Ornai, Amir Adar, Erez Gal
Structural Engineering, Ben-Gurion University of the Negev, Israel

14

Performance of SNRC in MAPEP Proficiency Tests During 2005-2013

Ofer Aviv, Zohar Yungrais, Sharon Moscovici, Michal Brandis, Carmela Tzur, Lea Broshi, Tal Reimer, Reut Oren-Shemesh, Gustavo Haquin
Radiation Safety, Soreq Nuclear Research Center, Israel

15

Natural Circulation Modeling in MTR Fuel Geometry in Research Reactors

Yosef Aharon
NRCN, Israel

16

A New Approach to Analyze the Effect of Initial Conditions on Steam Explosion in Coolant Injection Mode

Idan Baruch¹, Galit Widenfeld²
¹*Nuclear Engineer, Ben Gurion University of the Negev, Israel*
²*NRCN, Israel*

17

Geological Disposal of Radioactive Waste

Ofra Klein Ben David, Avraham Dody
NRCN, Israel

18

Safety Issues of the LORELEI Test Device

Roni Sarusi¹, L. Ferry², D. Drapeau², M. Szanto³, N. Moran, M. Katz¹, Y. Weiss¹
¹*Safety, NRCN, Israel*
²*CEA, Cadarache, France*
³*Rotem Industries LTD, Israel*

Posters (Wednesday, February 12, 2014 10:15)

Gamma Scintillator System Enhancement for Neutron Detection using Boron Carbide for Homeland Security

Y. Ben-Galim¹, U. Wengrowicz², I. Orion¹, A. Raveh³
¹Ben Gurion University (BGU) of the Negev, Beer Sheva, Israel
²NRC-Negev, P.O. Box 9001, Beer-Sheva 84190, Israel
³Rotem Industries Ltd, Mishor Yamin D.N. Arava 86800, Israel

INTRODUCTION

An efficient and low cost ^{10}B based thermal neutron detector as a replacement for ^3He based neutron detectors is suggested. The detection is based on an enhancement to a scintillator gamma-rays detector. ^3He supply for neutron detectors is gradually become harder to obtain⁽¹⁾ since the commercial production of this isotope has been practically ended. The $^{10}\text{B}(n,\alpha)^7\text{Li}$ interaction is characterized with two energetic ion and a 478 keV gamma photon which is emitted from the excited ^7Li in 94% of the interactions⁽²⁾. A tailored Monte-Carlo code for the detector model was written in MATLAB in order to assess the detector's efficiency. The simulation model is based on ENDF/B-VII.0⁽³⁾ libraries for neutrons cross sections, and XCOM⁽⁴⁾ database for gamma absorption coefficients. By varying the B_4C thickness, optimal efficiency was obtained both for natural occurring ^{10}B compound with atomic abundance of 19.8% as well as for boron-10 enriched to 96%.

RESULTS

The simulation results showed intrinsic thermal neutron efficiency (ITNE) of about 40-45% both for natural and enriched compounds. This suggests that a coupling of natural B_4C converting layer with an existing gamma-rays scintillator detector will produce an effective low cost neutron detector. This coupling enables neutron detection by capturing the 478 keV gamma-photon. Validation of the MATLAB code for the suggested detector was accomplished through comparison with a Monte Carlo N Particle (MCNP4C2⁽⁵⁾) simulation results for the same detector configuration. An experimental model was assembled for verification of the simulation results. The boron used for the experiment was a B_4C disc (2" diameter, 0.125" thick) supplied by PLASMATERIALS (USA) coupled with a CsI scintillator detector with dimensions of 3" diameter and height of 3" and a photomultiplier (PMT). The experiment configuration is pictured in figure 1.

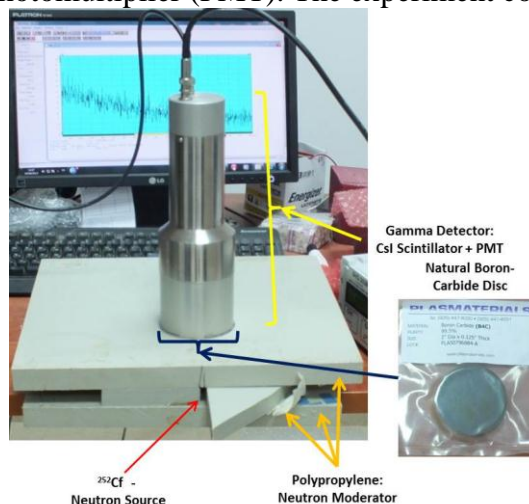


Figure 1: The experiment set-up configuration.

The measured efficiency from the experiment shows good agreement with both model's approximations and yielded a total measured efficiency of ~12.4% (count spectrum in figure 2).

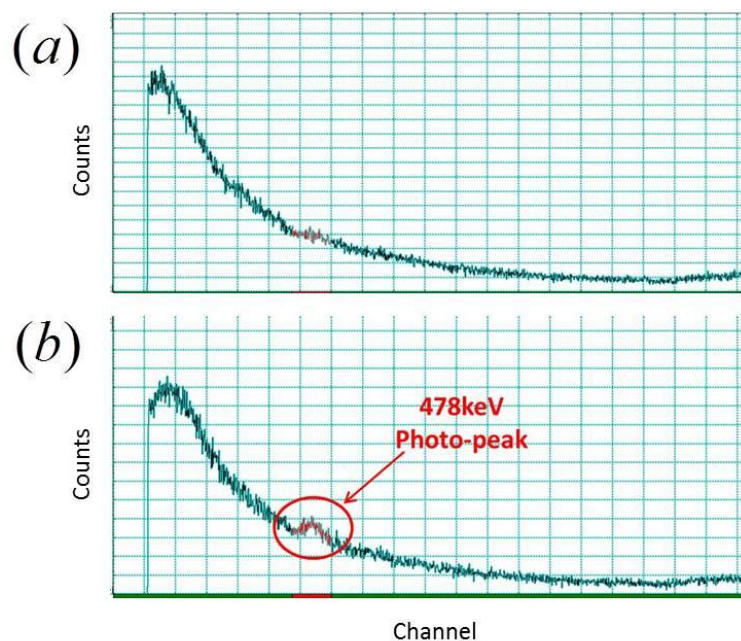


Figure 2: Spectrum of intensity vs. energy. (a) the scintillator positioned in front of the ^{252}Cf source. (b) B_4C disc was added as a neutron absorber.

CONCLUSIONS

The implementation of natural B_4C rather than enriched boron-10 compounds and the usage of an existing gamma-ray detector makes this detector easy to assemble and relatively inexpensive. Moreover, since B_4C is virtually transparent to gamma, thick neutron converting layers may be applied in order to increase neutron absorption probability without degrading the overall efficiency as oppose to ion capture methods. The analysis for various applications where gamma detectors are widely available such as Homeland Security can be performed by subtracting the signals from two similar scintillator detectors; one is a reference and the second is coupled with a B_4C converting layer. For other applications, it is feasible to develop an electronic circuit that can collect only the desired photo-peak counts.

REFERENCES

1. R. T. Kouzes, *The ^3He Supply Problem*, Pacific Northwest National Laboratory, 2009.
2. G. F. Knoll, *Radiation Detection and Measurement*, third edition, John Wiley & Sons, Inc, 2000.
3. *ENDF/B-VII.0 Libraries*, Organisation for Economic Co-Operation and Development (OECD) - Nuclear Energy Agency (NEA) - JANIS 3.4. [Online]. Available: <https://www.oecd-nea.org/janis/>
4. *XCOM - Photon Cross Sections Database*, National Institute of Standards and Technology (NIST), [Online]. Available: <http://www.nist.gov/pml/data/xcom/index.cfm>
5. *Monte Carlo N-Particle Transport Code System*, version 4C2, Technical Report LA-13 709-M, Los Alamos National Laboratory, NM, USA, 2001.

Zero Time of Transitory Nuclear Events Derived by Parent-Daughter Systems

Y. Nir-El

125 Lilac Street, P.O.Box 1476, Reut 71799, Israel

INTRODUCTION

The detection and identification of a nuclear event that results in the dissemination of radioactive products into the environment can be realized by dating the age of the event. In order to correct observed activities for the decay since the occurrence of the event, the age must be known to a high level of confidence. Previous papers^(1,2) described the method to date the age of a nuclear event by measuring the activity of two fission products, which constitute the clock in this application.

Within the proficiency test programme for radionuclide laboratories supporting the CTBT, a simulated gamma spectrum with the characteristics of an atmospheric test of a Chinese thermonuclear device, was used to determine the zero time by calculating the theoretical peak area ratio of $^{95}\text{Nb}/^{95}\text{Zr}$ ⁽³⁾. Their approach used only the main gamma lines at 766 and 757 keV and assigned the same detection efficiency to both these close lines. Their methodology of calculating the uncertainty of zero time is subject to comments because it takes the sum of two components (nuclide ratio and activity ratio as function of time) in quadrature.

In another paper⁽⁴⁾, the activity of ^{95}Nb as a function of time was presented without any development or expression for the zero time.

Analytical equations for zero time and the associated uncertainty calculations were derived in a recent paper⁽⁵⁾ using a measured activity ratio of two nuclides and illustrating the procedure by data from the Chinese test. The evaluation of the zero time uncertainty was performed by a very large set of very complicated analytical equations.

The present paper aims at developing a procedure to determine the zero time and its uncertainty in a transitory nuclear event by treating a parent-daughter system of 3 nuclides, where one daughter feeds the other one, in addition to its direct feeding by the decay of the parent.

ACTIVITY OF PARENT AND DAUGHTERS

Transitory (brief duration) nuclear events are e.g. an explosion of a nuclear device, or an accidental release of radioactivity due to a start-up failure in a reactor loaded with fresh nuclear fuel. An accurate and precise age of a nuclear event can be determined by the gamma spectrometric measurement of activities of a parent-daughter system and their dependence on time. This relation excludes the complications and misleading results arising from physicochemical fractionation effects in non-isobaric fission products.

The analysis of measured parent and daughters that are not in equilibrium is non-trivial and a wrong decay correction of the daughter activity can be an explanation for discrepancies in proficiency test exercises. Some commercial softwares perform an on-line analysis for merely two members, e.g. ^{140}Ba (parent)- ^{140}La (daughter). Hence, the analysis of parent-daughter cases of 3 members should be performed off-line solving differential equations that express the rate of change of the number of atoms.

At the time $t = 0$, only the parent ^{95}Zr (nuclide #1 in the decay chain) is present in the sample and the number of atoms of both daughters $^{95\text{m}}\text{Nb}$ (nuclide #2) and ^{95}Nb (nuclide #3) is assumed to be zero. This is the case of a radiochemical separation of ^{95}Zr which takes place at $t = 0$, or the situation of the transitory nuclear events, i.e. device explosion or reactor start-up failure, where the direct (independent) fission production of both #2 and #3 is practically null compared to the direct fission production of ^{95}Zr .

Parent ^{95}Zr , nuclide #1, $T_{1/2} = 64.032(6)$ d

$$\frac{dN_1(t)}{dt} = -\lambda_1 N_1(t)$$

$$A_1(t) = A_1(0)e^{-\lambda_1 t}$$

Daughter $^{95\text{m}}\text{Nb}$, nuclide #2, $T_{1/2} = 3.61(3)$ d

$$\frac{dN_2(t)}{dt} = -\lambda_2 N_2(t) + a\lambda_1 N_1(t) \quad a = 0.0108(7)$$

$$A_2(t) = \frac{aA_1(0)}{1 - \frac{\lambda_1}{\lambda_2}} (e^{-\lambda_1 t} - e^{-\lambda_2 t})$$

Daughter ^{95}Nb , nuclide #3, $T_{1/2} = 34.991(6)$ d

$$\frac{dN_3(t)}{dt} = -\lambda_3 N_3(t) + (1-a)\lambda_1 N_1(t) + b\lambda_2 N_2(t) \quad b = 0.944(6)$$

$$A_3(t) = A_1(0) (f_1 e^{-\lambda_1 t} + f_2 e^{-\lambda_2 t} + f_3 e^{-\lambda_3 t})$$

$$f_1 = \frac{1}{1 - \frac{\lambda_1}{\lambda_3}} \left(1 - a + \frac{ab}{1 - \frac{\lambda_1}{\lambda_2}} \right)$$

$$f_2 = -\frac{ab}{\left(1 - \frac{\lambda_1}{\lambda_2}\right) \left(1 - \frac{\lambda_2}{\lambda_3}\right)}$$

$$f_3 = \frac{ab}{1 - \frac{\lambda_1}{\lambda_2}} \left(\frac{1}{1 - \frac{\lambda_2}{\lambda_3}} - \frac{1}{1 - \frac{\lambda_1}{\lambda_3}} \right) - \frac{1-a}{1 - \frac{\lambda_1}{\lambda_3}}$$

The reference time of activity is the start of measurement t_1 , as required in many applications, e.g. proficiency test exercises, and t_2 is its end. Integration of the count rate gives

$$A_3(t_1) = \frac{\lambda_3 I_3}{\varepsilon_3 P_3 C_3} - A_1(t_1) f_1 \left(\frac{\lambda_3 C_1}{\lambda_1 C_3} - 1 \right) - \left[A_2(t_1) - \frac{aA_1(t_1)}{1 - \frac{\lambda_1}{\lambda_2}} \right] \frac{b}{1 - \frac{\lambda_2}{\lambda_3}} \left(\frac{\lambda_3 C_2}{\lambda_2 C_3} - 1 \right)$$

$$C_i = 1 - e^{-\lambda_i(t_2-t_1)}, \quad i = 1, 2, 3.$$

Private case

$a = 0$, that is no feeding of $^{95\text{m}}\text{Nb}$.

$$A_3(t_1) = \frac{\lambda_3 I_3}{\varepsilon_3 P_3 [1 - e^{-\lambda_3(t_2-t_1)}]} - \frac{A_1(t_1)}{1 - \frac{\lambda_1}{\lambda_3}} \cdot \left\{ \frac{\lambda_3 [1 - e^{-\lambda_1(t_2-t_1)}]}{\lambda_1 [1 - e^{-\lambda_3(t_2-t_1)}]} - 1 \right\}$$

This is exactly the equation of a ‘one parent-one daughter’ case, see e.g. in the Genie 2000 software. A similar equation is used to calculate the activity of $^{95\text{m}}\text{Nb}$,

$$A_2(t_1) = \frac{\lambda_2 I_2}{\varepsilon_2 P_2 [1 - e^{-\lambda_2(t_2-t_1)}]} - \frac{A_1(t_1)}{1 - \frac{\lambda_1}{\lambda_2}} \cdot \left\{ \frac{\lambda_2 [1 - e^{-\lambda_1(t_2-t_1)}]}{\lambda_1 [1 - e^{-\lambda_2(t_2-t_1)}]} - 1 \right\}$$

Private case

$a = 1$, that is ^{95}Zr decays entirely to $^{95\text{m}}\text{Nb}$.

$$A_3(t) = b\lambda_2\lambda_3 A_1(0) \left[\frac{e^{-\lambda_1 t}}{(\lambda_2 - \lambda_1)(\lambda_3 - \lambda_1)} + \frac{e^{-\lambda_2 t}}{(\lambda_1 - \lambda_2)(\lambda_3 - \lambda_2)} + \frac{e^{-\lambda_3 t}}{(\lambda_1 - \lambda_3)(\lambda_2 - \lambda_3)} \right]$$

This is identical to the Bateman solution for $n = 3$, where the branching of member #2 towards member #3 is b .

ZERO TIME

The ratio of the activity of ^{95}Nb to ^{95}Zr is given by

$$\frac{A_3(t)}{A_1(t)} = 2.204892(541) + 0.001243(82) \cdot e^{-0.181183t} - 2.206135(549) \cdot e^{-0.008984t}$$

Table 1 shows calculated activities of A_1 and A_3 , and their ratio A_3/A_1 , as a function of the time t , for $A_1(0) = 1$ Bq.

Table 1. Activities of ^{95}Zr and ^{95}Nb

t (d)	A_1 (Bq)	A_3 (Bq)	A_3/A_1
0	1.0000	0.0000	0.0000
10	0.8974	0.1692	0.1885
20	0.8053	0.2912	0.3616
30	0.7227	0.3758	0.5200
40	0.6486	0.4311	0.6648

The equation of $A_3(t)/A_1(t)$ is transcendental and can be solved to give the age t of the event by a numerical analysis method, e.g. the method of *Regula Falsi*⁽⁶⁾ requiring several iterations until a target convergence criterion is accepted.

As an example for applying the method, the data of the Chinese test in Ref. (3) are used:

$A_1(t) = 17.668$ Bq; $A_3(t) = 5.396$ Bq; Reference Time(= start measurement) = 25/09/2003 08:58.

Then, $A_3(t)/A_1(t) = 0.3054$ and therefore, by Table 1, the age is in the interval 10 to 20 d. Four iterations by *Regula Falsi* give 16.75247, 16.65740, 16.65464, and 16.65456 d. The fourth iteration changes the third by 7 time seconds. Hence, 3 iterations are sufficient for a 5×10^{-6} convergence at 16.6546 d. The zero time is found to be 08/09/2003 17:15, in perfect agreement with Ref (3), where the difference is approximately 1 time minute.

UNCERTAINTY OF ZERO TIME

The standard ($k = 1$) uncertainty $u(t)$ of the age t is given by

$$u^2(t) = \sum_{i=1}^n \left(\frac{\partial t}{\partial x_i} \right)^2 u^2(x_i)$$

where t is a function of n independent variables x_i , $i = 1, 2, \dots, n$, $\frac{\partial t}{\partial x_i}$ is the partial derivative of t with

respect to x_i , and $u(x_i)$ is the standard uncertainty ($k = 1$) of x_i . The equation of the activity ratio $R(t) = A_3(t)/A_1(t)$ cannot be solved analytically to render an explicit function of t . Hence, we cannot determine partial derivatives. Our approach is to invert the relationship, that is to calculate the uncertainty $u(R)$ according to

$$u^2(R) = \sum_{i=1}^6 \left(\frac{\partial R}{\partial v_i} \right)^2 u^2(v_i)$$

where $u(R)$ is known from the measurement, the 6 variables v_i are λ_1 , λ_2 , λ_3 , a , b , and t . The age $t = 16.6546$ d had been already found and the unknown is $u(t)$. By Ref. (3), $u(R)$ is 0.002932 (0.96%). Then, $u(t)$ is calculated to be 0.168 d = 4.037 h. This value disagrees with 0.26 d = 6.2 h in Ref. (5) which presents a rather complex procedure of calculating the uncertainty of zero time. On the other hand, Ref.(3) presents the value $u(t) = 0.17$ d, but their prescription of uncertainty budget and computing the combined uncertainty is questionable. It is worthwhile to note that the 0.17 d uncertainty is obtained by ignoring the $^{95\text{m}}\text{Nb}$ nuclide and using the equation of one parent-one daughter⁽¹⁾

$$t = \frac{1}{\lambda_1 - \lambda_2} \ln \left[1 - \left(1 - \frac{\lambda_1}{\lambda_2} \right) \left(\frac{A_3}{A_1} \right) \right]$$

This equation gives $t = 16.60$ d.

REFERENCES

1. Nir-El Y. *Dating the age of a nuclear event by gamma spectrometry*, Appl. Radiat. Isot. **60**, p.197-201, (2004).
2. Nir-El Y. *Dating the age of a recent nuclear event by gamma-spectrometry*, J. Radioanal. Nucl. Chem. **267**, p.567-573, (2006).
3. Karhu P., De Geer L.-E., McWilliams E., Plenteda R., Werzi R. *Proficiency test for gamma spectroscopic analysis with a simulated fission product reference spectrum*, Appl. Radiat. Isot. **64**, p.1334-1339, (2006).
4. Harms A., Johansson L., MacMahon D. *Decay correction of ^{95}Nb* , Appl. Radiat. Isot. **67**, p.641-642, (2009).
5. Pan P., Ungar R. K. *Nuclear event zero-time calculation and uncertainty evaluation*, J. Environ. Radioactivity **106**, p.65-72, (2012).
6. Hildebrand F. B. *Introduction to Numerical Analysis*, McGraw-Hill, New York, NY, 1956.

Optimized Activity Concentration Monitoring System for Ventilation Duct at Positron Emitters Production Center

E. Vax¹, V. Bronfenmacher², A. Broide¹, D. Ginzburg², V. pushkarsky², L. Kaplan², T. Mazor¹, Y. Kadmon¹,
A. Osovizky²

¹ Nuclear Research Center Negev, Beer Sheva, Israel

² Rotem Industries Ltd, Israel

INTRODUCTION

Monitoring the radioactive isotopes concentration released from cyclotron center is mandatory for complying with the site operational license and federal regulations. Cyclotrons are commonly used for production of radioactive isotopes for Positron Emission Tomography (PET). The isotopes are short half life β^+ emitters used for medical imaging purposes. There exist routine releases of small amounts of isotopes during the production process. The possibility of uncontrolled isotopes emission through the ventilation system, in case of malfunction, increases the radiation hazard potential to nearby population. Since the relatively short time decay of these isotopes made the wide use of cyclotrons next to populated areas possible. As a protection, any factory license requires activity release management for compliance with the total radionuclides activity emission limit. The limit is set to ensure no member of the public receives an effective dose equivalent above 10 mrem/year⁽¹⁾.

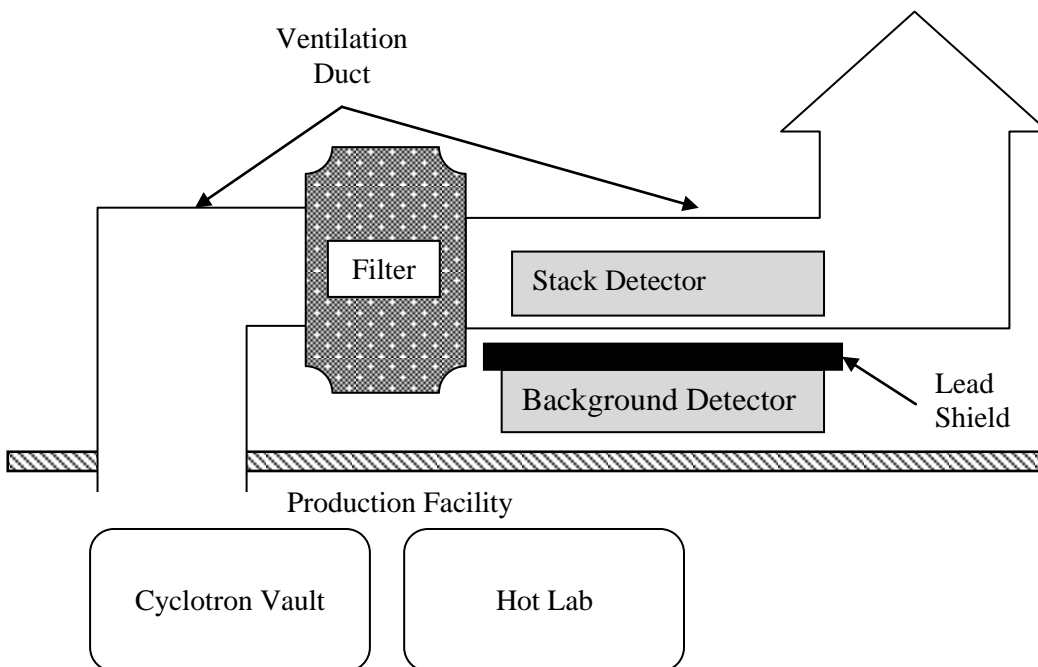


Figure 1: System block diagram. The stack detector location enables a high sensitivity to the activity concentration releases however it also sensitive to radiation field caused by the site routine activity, the shining filters and releases at neighbored stacks.

The design of a system that monitors the total activity released should address two main requirements: (1) adequate sensitivity (2) accurate report about the emitted activity. The sensitivity should comply with detection of very low concentration level of PET isotopes. In addition the report should provide an accurate estimation of the released activity based on the detector's gross counts reading and the air volume flow. These two requirements are in a contradiction. The best sensitivity is achieved by installing the detector inside the ventilation duct. On the other hand, correct release identification and accurate activity calculation, require a distant and shielded measuring point, where the effect of the shining filters or radioactive sources movement at the hot-lab can be reduced and even eliminated.

METHOD

Mapping the obstacles for accurate release calculation is a necessary step in designing a system with the ability to suppress the different noises while identifying and calculate correctly the activity release. The noise is comprised of statistical fluctuations, external radiation source readings not caused by activity concentration that flows inside the ventilation duct, and background changes due to absorption of isotopes in the filter and their decay. Table 1 lists all the noise sources and the methods chosen to overcome it.

Table 1: Obstacles for accurate activity release calculation and the overcome methods

radiation field source	Solution
Shining filter	Background detector has higher readings,
Site Routine activity	Background detector has higher readings + atypical rise shape
Natural background	Electronic energy window + accumulate only fast rise
Chemical absorption	software algorithm local background subtraction
Release through a neighboring duct	Background detector
Routine maintenance	Calibration point

The analysis of these noises led to the following system design. The configuration is based on two scintillation based radiation detectors (2"x2" NaI(Tl)) with an electronic discriminator for the 511keV energy window and software interface with implemented algorithm used to identify the release itself. The first detector (stack detector) is located inside the ventilation duct for maximum proximity to the isotopes release, thus accomplish the required sensitivity. The second detector (background detector) is located just below the ventilation duct and shielded from above, as shown in Figure 1. The combination of the data from the two detectors infers about the source of the radiation field, e.g. whenever the signal is stronger in the background detector (Figure 2), one can eliminate this as an external activity.

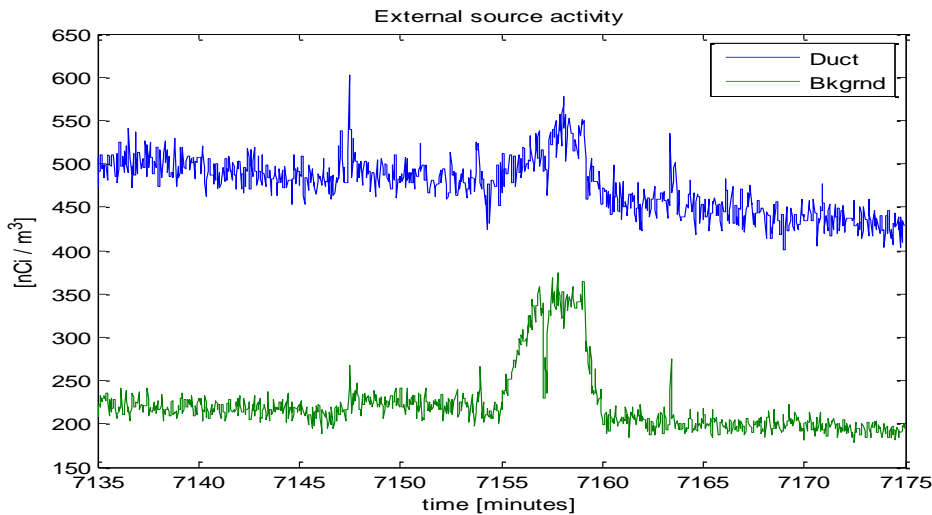


Figure 2: External source signal

RESULTS

The experimental data demonstrates the ^{18}F isotope, which is the most common PET isotope. The nature of the emission can be characterized as pulsed release or as slow release. A pulsed release of a gassed $^{18}\text{F}_2$ isotope causes a fast rise in the detector readings spread for about a minute, due to the air flow. This is followed by a small rise of the steady state reading caused by the air filter absorbing a small amount of the $^{18}\text{F}_2$. A slow release, on the other hand, shows a rise of the readings for 10-40 minutes, indicating that most of the ^{18}F particles released were absorbed in the air filter. Following the release one can see a slow decrease in the raw reading of the detector fitting the 110 minutes half life time of the isotope. A case study (Figure 3) shows a 20 minutes rise due to slow release of ^{18}F accumulated in the air filter, followed by the slow decrease in the readings due to the isotope activity decay. Two fast releases can be observed riding the tail of the decay. Zooming in on these pulses (Figure 5), shows a step rise in the readings of the detector

followed by a fast return to the previous level, indicating that nearly all of the isotopes passed through the filters and close to the detector.

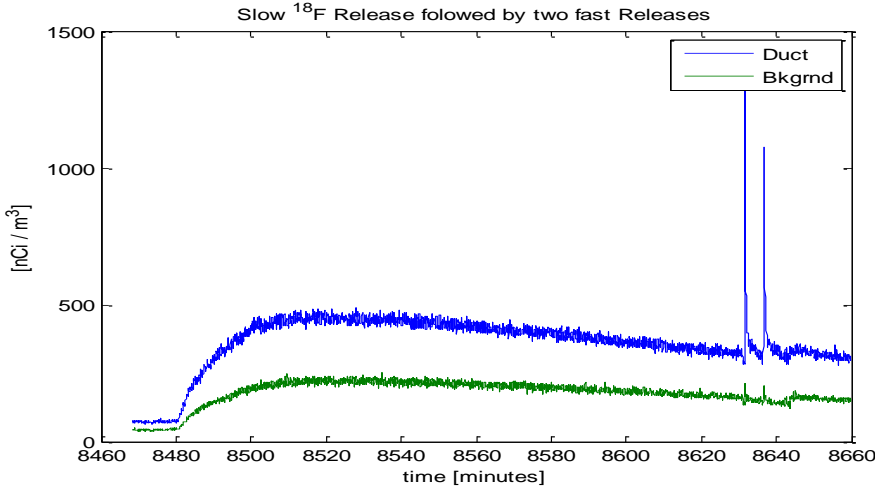


Figure 3: Slow Release of 18F followed by two fast Releases

In order to suppress the statistical fluctuations, detect peaks of the right shape and eliminate the local bias, we used a correlation of the detector readings with the correlation function shown at Figure 4. This function has zero mean and one unit power. It is designed to locate 20 seconds peaks, and subtract the local average excluding the peak. It also takes into account that there is a small background elevation following the release. The correlation function should be fine tuned for each stack detector according to its unique installation. One can modify the pulse length, its shape (exponential, symmetric or non-symmetric triangle) and the background averaging time, before and after the pulse, which effects the background elevation expected. These parameters are equivalent to a change in air speed, filter efficiency and the detector proximity to the filter.

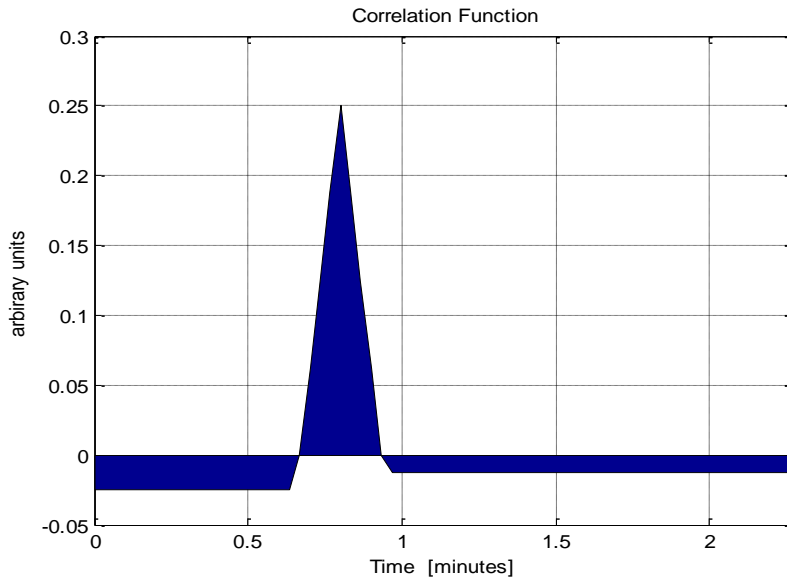


Figure 4: Slow correlation function for finding peaks

After locating the peaks, logic was constructed to determine whether the peaks were caused by a release or by a source outside the ventilation duct. For each release peak, we find its boundaries and accumulate the total readings (Figure 5) subtracting the background trapezoid total reading estimation (below the red line). This translates into the total activity emitted from the air duct.

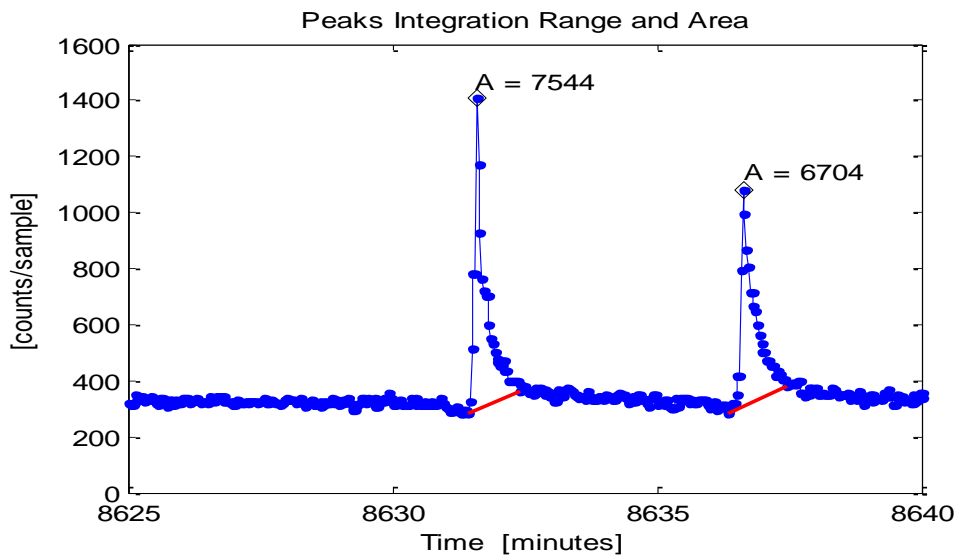


Figure 5: The algorithm final results: Peaks found (black marker), their boundaries (red) and the accumulated readings (above the red line) for each peak (black 'A')

DISCUSSION

The main obstacle of the radiation stack monitoring system is to define accurately the activity release out of the gross detector readings. As discussed, the stack detector readings originate in the activity flowing in the ventilation duct and several other sources which should not be accumulated as part of the activity release. The described system designed to overcome this complication by using the double detectors configuration and smart algorithm analyzing the data offline. Table 1 summarizes all the optional reasons for the detector reading that should not count as an activity release, and the methods used for improving the activity release documentation.

REFERENCES

1. *National Emission Standards for Emissions of Radionuclides Other Than Radon from Department of Energy Facilities*, National Emission Standard for Hazardous Air Pollutants (NESHAPS) 40 CFR 61 Subpart H,
2. D. Ginzburg, et al., *Methods for Determining the Activity Concentration Calibration Factor for Ventilation Duct in Cyclotron Sites*, The 24th Conference of the Nuclear Societies, p.151-153, Dead-Sea, Isreal, Feb. (2008)

Flattening the Energy Response of a Scintillator Based Gamma Dose Rate Meter Coupled to SiPM

Y. Knafo¹, A. Manor¹, D. Ginzburg¹, M. Ellenbogen¹, A. Osovizky¹
U. Wengrowicz², M. Ghelman², R. Seif², T. Mazor², Y. Kadmon², Y. Cohen²

¹*ROTEM Industries Ltd., Beer-Sheva, Israel*

²*Nuclear Research Center-Negev, Beer-Sheva, Israel*

INTRODUCTION

Among the newest emerging technologies that are used in the design of personal gamma radiation detection instruments, the silicon photomultiplier (SiPM) light sensor is playing an important role. This type of photo sensor is characterized by low power consumption, small dimensions and high gain. These special characteristics present applicable alternatives for the replacement of traditional gamma sensors based on scintillator coupled to Photomultiplier tubes (PMT) or on Geiger-Muller(G.M.) sensors. For health physics applications, flat energy response is required for a wide range of radio-nuclides emitting gamma rays of different energies. Scintillation based radiation instrumentation provides count rate and amplitude of the measured pulses. These pulses can be split in different bins corresponding to the energy of the measured isotopes and their intensity. The count rate and the energy of the measured events are related to the dose rate. The conversion algorithm applies a different calibration factor for each energy bin in order to provide an accurate dose rate response for a wide range of gamma energies. This work describes the utilization of an innovative approach for dose rate conversion by using the abilities of newest 32-bit microcontroller based ARM core architecture.

METHODS

Radiation survey meters that are based on G.M tubes are widely used for the measurement of gamma levels. In these types of instruments, a single pulse is obtained for each gamma photon interaction in the sensitive volume of the sensor. The counting efficiency for gamma rays depends on the probability of a gamma photon interacting with the cathode wall and producing an electron, and also on the probability that the electron will ionize the gas in the sensitive volume of the sensor. These probabilities drastically reduce the detection efficiency and are usually not related to the energy of the measured photons. The gamma field intensity depends on the source distance, on his activity and the energy of the emitted photons. Neglecting the distance and the medium material within the source and the detector, it is possible to assume that 1 gamma/s from 662 keV ¹³⁷Cs source produce a similar field response [mR/h] to the one produced by 11 gamma/s from 59.5 keV ⁶⁰Am source. In order to obtain a flat energy response, the G.M is usually enclosed into a mechanical filter which surrounds the tube. The filter absorbs most of the low energy gamma rays in order to reduce the low energy over response. The intrinsic sensitivity is the ratio between the detected pulses and the gamma rays fluency within the sensor active volume. For G.M. based sensor, the intrinsic sensitivity for high energy photons such as gamma rays is about 1% [1].

In order to increase the gamma rays detection efficiency while maintaining or even reducing the detector dimensions scintillation based sensors are used. These sensors usually provide a high stopping power. The scintillator light pulses intensity depends on the energy absorbed within the crystal. The light emitted by the interaction of gamma photons with scintillation material is determined by the photon energy and the scintillation material properties. Those pulses can be measured using a sensitive light detector such as a photodiode, a PMT or a SiPM. The intrinsic efficiency depends on the gamma energy, the crystal density and the dimensions. The light sensor optical properties and the photo-coupling to the crystal influence also on the intrinsic efficiency. A small 1cc CsI(Tl) crystal, has nearly 100% intrinsic efficiency for 100keV photons. For a similar dimensions crystal, the efficiency of rapidly drops to a few percents for higher gamma energy such as 662keV ¹³⁷Cs gamma rays.

The output pulse amplitude of scintillator based detectors is related to the energy deposited in the crystal by the gamma photons. Accurate dose rate measurement is achieved by splitting the measured pulses into

various bins related to their amplitude. Then, dose rate is calculated according to the count rate and a calibration factor for each bin. For low count rate, this procedure enables a flat energy response.

In modern instrumentation, a microcontroller unit (MCU) implements the flat energy response algorithm for the obtained pulses. Usually, the output signal is sampled by a digital to analog converter (DAC). This approach can last a relative long time and is power consuming for hand held instrumentation requirements. To overcome these obstacles, we implement the approach using an array of voltage comparators. Each comparator with his appropriate threshold is connected to a hardware counter. Due to the lack of many hardware counters in older families of 8-bit MCUs, the traditional way to perform the accumulation is to configure some general purpose input/output ports (GPIO) of the MCU to an interrupt port. By the MCU software, every measured pulse is accumulated in the according bin. In this way, a lot of processing time is required to manage the interrupt routine. For high count rate applications, the processing time limits the available resources required for other algorithms real-time tasks.

Newest 32-bit MCU ARM based cortex-M3 architectures provide at least 4 hardware counters. Among many other features, this type of MCU provides: more communication peripherals, like 3xUSART(universal synchrony/asynchrony receive transmit), 2xSPI, 2xI2C, 10 timers, 128KB Flash memory for the application code, internal 4KB EEprom for calibration parameters storage and event log accumulation. All of these features are achievable without external components reducing energy consumption and instrument dimensions. The dose rate is calculated by measuring the hardware counters even for high count rates. By this approach, essential processing time and resources are released from the MCU to focus in real-time algorithms. For accurate dose rate calculations, many energy bins are required. Sometimes, the number of measured bins is higher than the available counters in the MCU. In this case, low energy output pulses are measured by hardware counters and high energy pulses which occurs seldom, are measured by the traditional method of software counters under interrupt routines without consuming MCU processing time.

RESULTS

The described algorithm was satisfactory implemented in the new Rotem Ind. survey meter named PDS-GO (Figure 1). The new PDS-GO (presented here), is based on 32-bit MCU ARM. His sensor, consists of a 3 cc CsI(Tl) crystal coupled to SiPM. The instrument was originally designed to meet the scope of specifications defined by Home-Land Security (HLS) standards for Personal Radiation Detector (PRD). For HLS applications, it is mandatory that the device will be highly sensitive, small, and robust and width long operating hours. Yet, regarding dose rate accuracy, the HLS standards are more tolerable than survey meter standards. The new PDS-GO, includes five different energy windows (bins) for improved dose rate calculation. The energy response (related to ^{137}Cs), is within $\pm 15\%$ from 60 keV up to 1.3 MeV gamma rays. This response, meets standard requirement for survey meters instrumentation. This improvement has been achieved while maintaining the existing capabilities for HLS applications.



Figure 1. PDS-GO survey meter

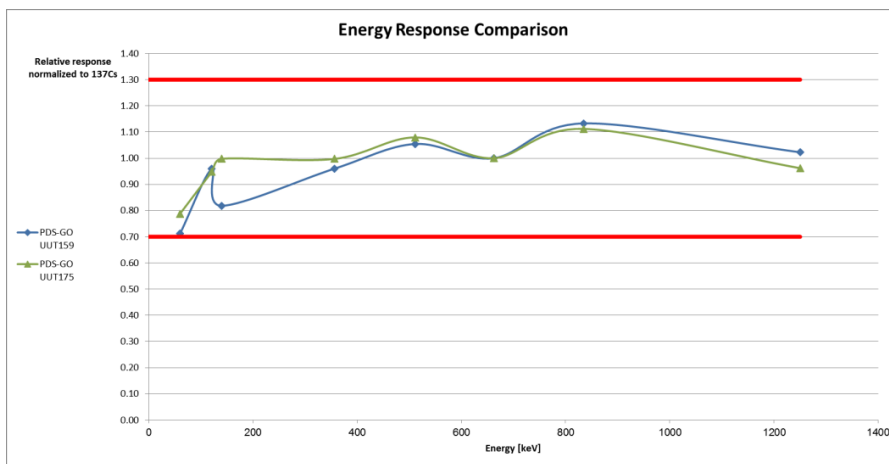


Figure 2. Energy response of the PDS-GO as measured for the following isotopes: ^{241}Am , ^{152}Eu , $^{99\text{m}}\text{Tc}$, ^{133}Ba , ^{22}Na , ^{137}Cs , ^{54}Mn , ^{60}Co

CONCLUSIONS

A new approach for high sensitive scintillator based gamma radiation survey meter is presented. The new PDS-GO meets the requirements for gamma survey meters and the specifications of PRDs for HLS applications as well. The ^{137}Cs relative response for different gamma sources is presented in Figure 2. The new electronics that maintain a larger number of hardware counters enable an improved accurate energy response over a wider gamma energy range.

REFERENCES

1. Centronic. Geiger Muller Tubes Data book, Croydon, England.
2. Rotem Ind. PDS-GO user manual, doc. No.17, rev. 1, Oct. 2013.
3. A. Osovizky et al. SENTIRAD – An innovative personal radiation detector based on a scintillation detector and a silicon photomultiplier, Nuclear Instruments and Methods in Physics Research A, 652, Issue 1, pp. 41-44 (2011).
4. D. Ginzburg et al. Optimizing the design of a silicon photomultiplier-based radiation detector, Nuclear Instruments and Methods in Physics Research A, 652, Issue 1, pp. 474-478 (2011).

Neutron Dose Measurement Using a Cubic Moderator

M. Sheinfeld¹, T. Mazor¹, Y. Cohen¹, Y. Kadmon¹, I. Orion²

¹ Nuclear Research Center-Negev, P.O.Box. 9001, Beer Sheva 84190, Israel

² Ben Gurion University of the Negev, Beer-Sheva, Israel

INTRODUCTION

The Bonner Sphere Spectrometer (BSS), introduced In July 1960⁽¹⁾ by a research group from Rice University, Texas, is a major approach to neutron spectrum estimation. The BSS, also known as multi-sphere spectrometer, consists of a set of a different diameters polyethylene spheres, carrying a small LiI(Eu) scintillator in their center. What makes this spectrometry method such widely used, is its almost isotropic response, covering an extraordinary wide range of energies, from thermal up to even hundreds of MeVs.

One of the most interesting and useful consequences of the above study is the 12" sphere characteristics, as it turned out that the response curve of its energy dependence, have a similar shape compared with the neutron's dose equivalent as a function of energy⁽²⁾. This inexplicable and happy circumstance makes it virtually the only monitoring device capable providing realistic neutron dose estimates over such a wide energy range. However, since the detection mechanism is not strictly related to radiation dose, one can expect substantial errors when applied to widely different source conditions.

Although the original design of the BSS included a small 4mmx4mmØ ⁶Li(Eu) scintillator, other thermal neutron detectors has been used over the years: track detectors⁽³⁾, activation foils⁽⁴⁾, BF₃⁽⁵⁾ filled proportional counters, etc. In this study we chose a Boron loaded scintillator, EJ-254⁽⁶⁾, as the thermal neutron detector. The neutron capture reaction on the boron ¹⁰B(n,αγ)⁷Li has a Q value of 2.78 MeV of which 2.34 MeV is shared by the alpha and lithium particles.

The high manufacturing costs, the encasement issue, the installation efficiency and the fabrication complexity, led us to the idea of replacing the sphere with a cubic moderator.

This article describes the considerations, as well as the Monte-Carlo simulations done in order to examine the applicability of this idea.

THE METHOD

The Monte-Carlo simulations were implemented on the MCNP-4C platform, using the cross-section tables obtained from the ENDF/B-VI library. The reference system included a polyethylene sphere, having a 5% natural boron loaded scintillator detector in its center irradiated by a surface neutron source shaped as a 12" diameter disk. The source was placed 5 meters from the detector, perpendicular to an imaginary line connecting both centers. Since neutron creation probability is uniform all over the disk source, the probability density function will be proportional to r, with no dependence on the polar angle θ⁽⁸⁾:

$$p(r, \theta) dA = \frac{dA}{\pi R^2} = \frac{r dr d\theta}{\pi R^2}$$

$$p(r) dr = \int_0^{2\pi} \frac{r dr d\theta}{\pi R^2} = \frac{2r dr}{R^2}$$

$$p(r) = \frac{2r}{R^2} \propto r$$

Therefore, the source distribution can be programmed into its probability function as a linear function of the radius, by inclusion of a bias function to the source which will minimize the variance of the detector response.

In order to acquire meaningful results, Tally 4 and Tally multiplier FM4 have been used to obtain the average neutron flux in the scintillator. Theoretically, F4 is calculated by ⁽⁷⁾:

$$F4 = \int_V \int_t \int_E E \cdot \Phi(\vec{r}, E, t) dE dt \frac{dV}{V} = \int_V \int_E \int_s E \cdot \frac{N(\vec{r}, E, t) ds}{\text{Track Length Density}} dE \frac{dV}{V}$$

Where: $\Phi(\vec{r}, E, t)$ - Particles flux
 E - Particle energy
 V - The volume in which particles interactions occur

Tally FM4 card was used to normalize the result obtained by the F4 card with the multiplicative constant acquired by:

$$(^{12}\text{C}_{\text{Atomic Density}} + \text{H}_{\text{Atomic Density}} + ^{10}\text{B}_{\text{Atomic Density}} + ^{11}\text{B}_{\text{Atomic Density}}) \times \text{barn} \times \text{Volume}_{\text{Plastic Scintillator}}$$

Substituting EJ254 manufacturer data with the above parameters, gives the constant the value: 0.61092751. Moreover, this card was also used to select only the reactions contributing to the EJ254 total photon production.

The necessity for the long distance between the detector and the neutron source was derived from the assumption that the detector will respond differently when encompassed in a sphere rather than in a cube, especially due to differences in spatial angular response. All that was left was to verify the theory that when the distance between the source and the detector is long enough, the behavior of cube moderator will resemble the spheres.

The following 3 criterions for cube's side length were examined:

1. **Cube's side length equals the sphere diameter:** under this criterion it appeared that although the resemblance between graphs was satisfying, the comparison of total counts ratio at 22 neutron energies, gave:

$$0.90 \leq \frac{\text{Sphere Counts}}{\text{Cube Counts}} \leq 3.39$$

Meaning an average of 1.73 and standard deviation 0.893.

2. **Equal volumes for the cube and the sphere:** in this case the counts ratio gave:

$$0.46 \leq \frac{\text{Sphere Counts}}{\text{Cube Counts}} \leq 0.71$$

Meaning an average of 0.6 and standard deviation 0.092.

Where cube side length was Calculated by:

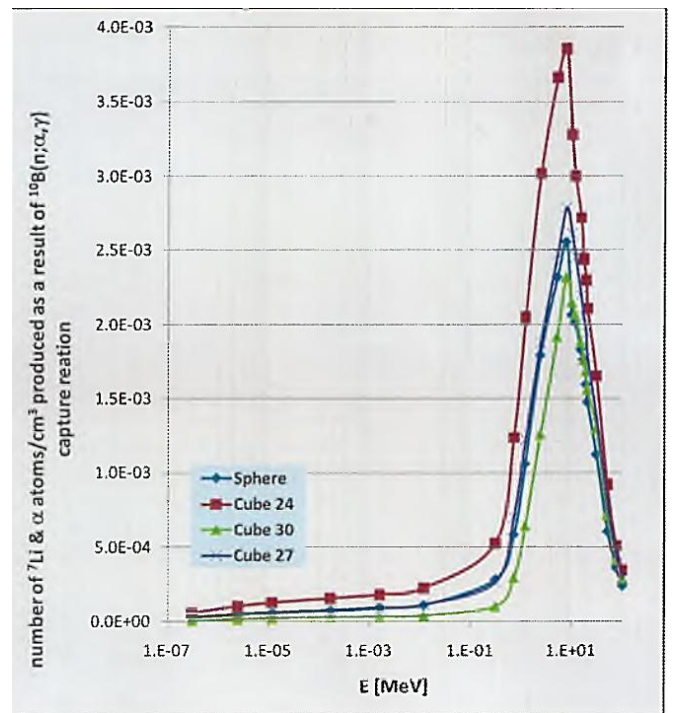


Fig. 1: Comparison between the sphere and cubes

$$a = \sqrt[3]{\text{Sphere Volume}} = \sqrt[3]{\frac{4}{3}\pi(6'')^3} = 24.566\text{cm}$$

3. Equal cross-section area at the detector's location: cube side length was calculated by:

$$a = \sqrt{\pi(6'')^2} = 27.012\text{cm}$$

in this case the counts ratio gave $0.46 \leq \frac{\text{Sphere Counts}}{\text{Cube Counts}} \leq 0.71$ Meaning an average of 0.9528 and standard deviation 0.124.

The 3rd criterion brought the highest behavioral compatibility between the cube and the sphere, but the cube was irradiated only from one of its facets. To prove a higher level of compatibility we needed to examine the cube's behavior when irradiated from other directions. To accomplish this goal, the coordinate's transformation card, TR, was used.

It has been decided that the neutron disk source will be diverted by 45° with respect to XYZ axes (see fig. 2), while the distance between the source's and the detector's centers will remain 5 meters.

Using the Pythagorean and the Cosine theorems, the rotation matrix was found to contain the following angles:

$$\begin{aligned} \angle_{xx'} &= 60^\circ, \angle_{yx'} = 60^\circ, \angle_{zx'} = 45^\circ, \\ \angle_{xy'} &= 135^\circ, \angle_{yy'} = 45^\circ, \angle_{zy'} = 90^\circ, \angle_{xz'} = 120^\circ, \\ \angle_{yz'} &= 120^\circ, \angle_{zz'} = 45^\circ. \end{aligned}$$

All MCNP simulations were repeated under the rotation data and the 3rd criterion above.

The counts ratio this time was:

$$0.82 \leq \frac{\text{Sphere Counts}}{\text{Cube Counts}} \leq 1.35$$

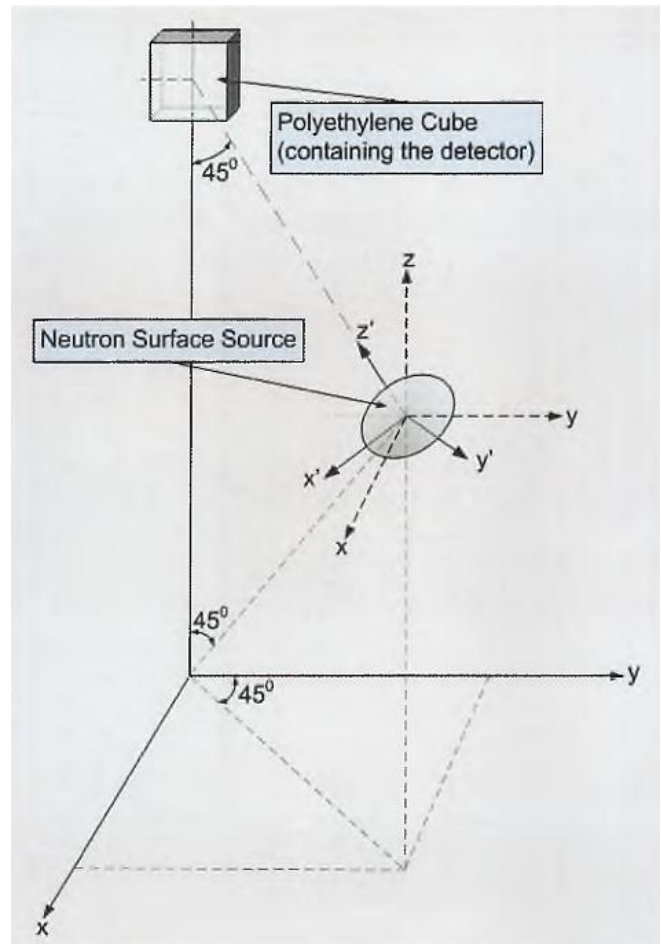


Fig. 2: Source shifting with respect to the irradiated cube

Having an average of 1.0163 with standard deviation 0.12991.

SUMMARY AND CONCLUSIONS

After confirming the correctness of the MCNP input file, by comparison to the literature ⁽²⁾, other MCNP simulations were conducted using a cubical neutron moderator.

Three criteria for cube side length were studied, where the optimum was set as the closest Resemblance to the behavior of the sphere moderator over a wide energy range. Therefore, the 3rd criterion was selected, giving

$$\frac{\text{Sphere Counts}}{\text{Cube Counts}} \cong 1$$

The angular dependency of the cube configuration has been studied too, giving satisfactory results.

The conclusion from this study is that whenever the measurement of neutron's dose equivalent is required, one can always use the cubic moderator, under the conditions stated in this paper (distance from source, accuracy demands, manufacturing costs, installation limitations etc.).

Furthermore, this study was just theoretical, requiring extensive laboratory experiments in order to confirm the commercial usage of the cubic configuration.

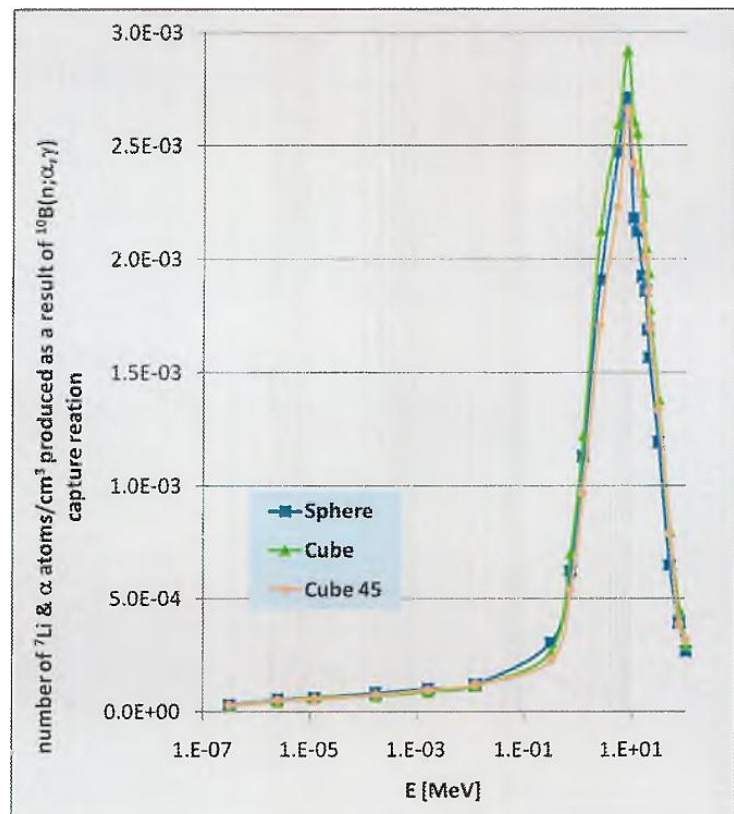


Fig. 3: The spatial dependency of neutron detection using cube moderator in comparison to sphere moderator

REFERENCES

1. R. L. Bramblett, R. I. Ewing and T. W. Bonner, *A Type of Neutron Spectrometer*, Nuclear Instrumentation and Methods 9(1), July 1960.
2. Glen F. Knoll, *Radiation Detection and Measurement*, 3rd edition, pp. 539-540.
3. M. P. Dhairyawan, P. S. Nagarajan and G. Venketaraman, *Further Studies on the Response of Spherical Moderated Neutron Detectors*, Nucl. Instrum. Methods 175,1980, pp 561-564.
4. W. G. Alberts et al., *European Workshop on Neutron Dosimetry for Radiation Protection*, Physikalisch Technische Bundesanstalt Report PTB-ND-17, Braunschweig, Germany, 1979, pp. 1-43.
5. A. V. Alevra and D. J. Thomas, *Radiation Protection Dosimetry*107, 2003, p. 36.
6. www.eljentechnology.com, *EJ-254 Datasheet*, ELGEN Technology.
7. *Monte Carlo N-Particle Transport Code System*, Version 4C2, Technical Report LA-13 709-M, Los Alamos National Laboratory, NM, USA, 2001.
8. B. J. Macdougall, *The effect of Bonner Sphere Borehole Orientation on Neutron Detector Response*, Master's Thesis, University of Tennessee, 2010

Composites Based on Fly Ash and Clay

E.Fidancevska¹, V.Jovanov¹, B.Angusheva¹, V.Srebrenkoska²

¹Faculty of Technology and Metallurgy, Ruger Boskovic 16, 1000 Skopje, Republic of Macedonia

²Faculty of Technology, Krste Misirkov, 2000 Stip, Republic of Macedonia

INTRODUCTION

Fly ash is a waste generated from the coal combustion during the production of electricity in the thermal power plants. It presents industrial by-product containing Technologically Enhanced Natural Occurring Radioactive Materials (TENORM) with the great potential for valorisation⁽¹⁾. Fly ash is successfully utilized in cement and concrete industry⁽²⁾, also in ceramics industry⁽³⁾ as component for manufacturing bricks and tiles, and recently there are many investigations for production of glass-ceramics⁽⁴⁾ from fly ash. Although the utilization of fly ash in construction and civil engineering is dominant, the development of new alternative application for its further exploitation into new products is needed. This work presents the possibility for fly ash utilization for fabricating dense composites based on clay and fly ash with the potential to be used in construction industry.

RESULTS

Fly ash (from the thermal power plant REK Bitola, Republic of Macedonia) with the chemical composition (SiO₂:52.00wt.%, Al₂O₃:23.61wt.%, Fe₂O₃:7.31wt.%, CaO:7.42wt.%, MgO:2.11wt.%, Na₂O:0.90wt.%, K₂O:1.67wt.%, SO₃:1.20wt.%, LOI: 3.12wt.%) was used as raw material for fabricating composites. The particle size distribution of the fly ash showed that the content of the fine fraction (less than 0.063mm) was dominant (47.10wt.%) and it was used in this investigation. The phase compositions of the fly ash consisted of: quartz, albite, hematite, anorthite, anhydrite and an amorphous phase. The concentrations of the natural radionuclides in fly ash as industrial by product were: ²⁶⁶Ra:59±6 Bq/kg; ²³²Th:76±8 Bq/kg; ⁴⁰K:376±29Bq/kg and are in accordance with the reported⁽⁵⁾. The typical morphology of the fly ash is presented in the figure 1. It is evident the presence of spherical particles and particles with irregular geometry and dimensions. The evident presence of diatomite can be seen from the honey sake morphology (fig. 1 b).

Clay (with granulometry less than 0.063mm) from the same region with the similar chemical composition (SiO₂:58.48wt.%, Al₂O₃:19.18wt.%, Fe₂O₃:7.44wt.%, CaO:6.18wt.%, MgO:1.43wt.%, Na₂O:2.10wt.%, K₂O:2.51wt.%, LOI: 2.05wt.%) was introduced to fly ash varying the quantity from 10 to 90wt.%. Quartz, feldspar, aragonite, illite, chlorite and calcite were the major crystalline phases present in clay. The composites were consolidated by uniaxially pressing at 45 MPa and the green samples were dried (105^oC) prior to sintering. Sintered composites were fabricated by firing at temperatures: 900, 1000, 1050, 1100^oC in chamber furnace with heating rate of 10^oC/min with a 60 min dwell at maximum firing temperature.

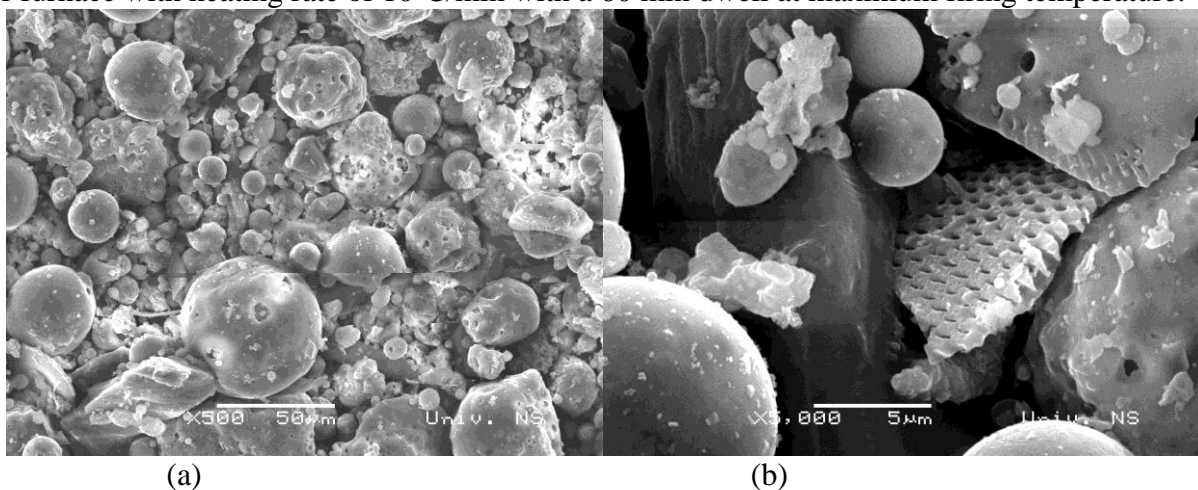


Figure 1. Morphology of the fly ash (a). bar 50µm, (b). bar 5 µm

The dependence of density and water absorption from the temperature for different fly ash –clay composites is presented in figure 2 and figure 3 presents the dependence of bending strength and E-modulus from temperature for the same composites.

Chemical durability of composites (sintered at 1050 and 1100⁰C) was tested using the standard methods for glass and ceramics. It was determined as mass lost after treatment in neutral (H₂O) and aggressive mediums (0.1M HCl and 0.1M Na₂CO₃) during the period of 24, 168 and 720 hours. The results of the leach testing of the composites in acid medium (0.1MHCl) are presented in figure 4.

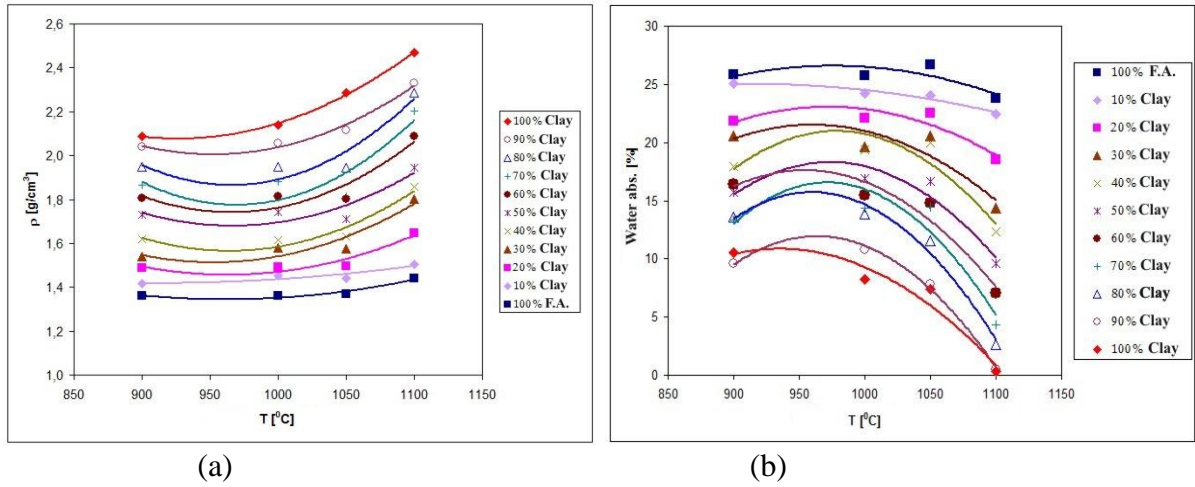


Figure 2. Dependence of : a. density from sintering temperature; b. water absorption from temperature

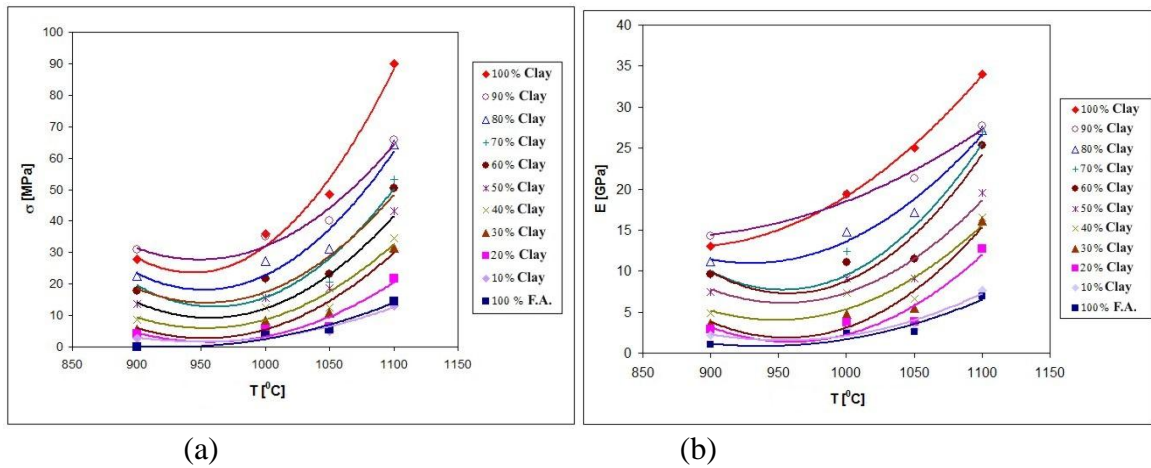


Figure 3. Dependence of: a. bending strength from temperature; b. E-modulus from temperature

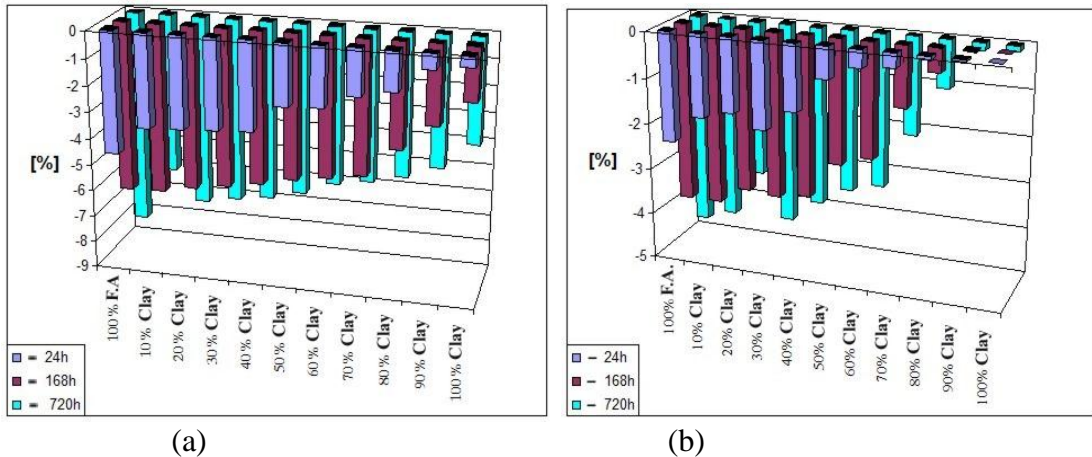


Figure 4. Leaching of the composites in acid medium (0.1MHCl) a. composites sintered at 1050⁰C, b. composites sintered at 1100⁰C

It is evident from the the figure 2 that clay content generally influences on the incensement of density and decrease mant the water absorption. Significant densification of the compacts was achieved by increasing the temperature from 1050⁰C to 1100⁰C. The mechanical properties (bending strength and E-modulus), figure 3, of the composites also increase with the addition of clay and the rapid densification was at temperature of 1100⁰C.

The clay content influenced positively on the durability of the compacts and it is directly connected to the density of the compacts. Namely, the densest composites i.e composites with higher content of clay have lower mass lost i.e. higher durability.

From the above investigation, as an optimal was chosen a composite containing 60wt.% clay and 40wt.% fly ash sintered at 1100⁰C. The density and water absorption of the composite were 2.09 g/cm³ and 7.02%, respectively, and the mechanical properties i.e bending strength and E-modulus were 50.47 MPa and 25.35GPa, respectively.

The microstructures of the composites with fly ash content of 40wt.%, sintered at 1050 and 1100⁰C are presented in figure 5.

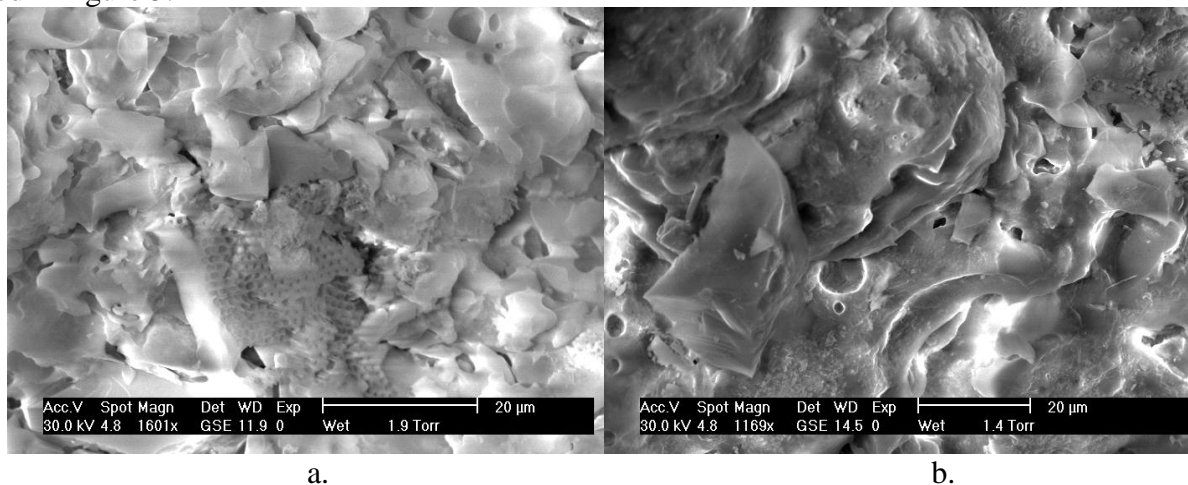


Figure 5. Microstructures of composites with 40wt.% fly ash content (bar 20µm) a. sintered at 1050⁰C
b. sintered at 1100⁰C

The degree of densification is evident, namely at temperature of 1050⁰C the morphology of diatomite is still present, but at 1100⁰C the composite is extensively sintered (more homogenous and smoother) with the evident appearance of small closed pores.

CONCLUSION

Fly ash as industrial by product can successfully replace certain quantity of clay as naturally occurring raw material to fabricate composites which can be potentially used as dense ceramics in construction industry.

REFERENCES

1. Somlai J., Jobbágy V., Kovács J., Tarján S., Kovács T. *Radiological aspects of the usability of red mud as building material additive*. J. Haszard. Mater. **150(3)**, p.541-546, (2008)
2. Kockal N U., Ozturan T. [*Effects of lightweight fly ash aggregate properties on the behavior of lightweight concretes.*](#) J. Hazar. Mater., **179(1-3)**, p. 954-965 (2010)
3. Queralt I., Querol X., Lopez-Soler A., Plana F. *Use of coal fly ash for ceramics: a case study for a large Spanish power station*, Fuel **76** p.787-791 (1997)
4. Barbieri L., Lancellotti I., Manfredini T., Queralt I., Rincon J.M., Romero M. *design obtainment and properties of glasses and glass-ceramics from coal fly ash*. Fuel **78** p.271-276 (1999)
5. http://www.irpa12.org.ar/KL/III.4.4/Haquin_fp.pdf (accessed on 30.12.2013)

Glass Ceramics Composites Fabricated from Coal Fly Ash and Waste Glass

B. Angjusheva¹, V. Jovanov¹, V. Srebrenkoska², E. Fidancevska¹

¹University "Ss Cyril and Methodius" Rudjer Boskovic 16, Skopje, Republic of Macedonia

²University Goce Delcev, Krste Misirkov bb, 2000 Stip, Republic of Macedonia

INTRODUCTION

Great quantities of coal ash are produced in thermal power plants which present a double problem to the society: economical and environmental. This waste is a result of burning of coal at temperatures between 1100-1450°C. Fly ash available as fine powder presents a source of important oxides SiO₂, Al₂O₃, Fe₂O₃, MgO, Na₂O, but also consist of small amount of ecologically hazardous oxides such as Cr₂O₃, NiO, MnO. The combination of the fly ash with waste glass under controlled sintering procedure gave bulk glass-ceramics composite material. The principle of this procedure is presented as a multi barrier concept⁽¹⁾. Many researches have been conducted the investigations for utilization of fly ash as starting material for various glass-ceramics production⁽²⁻⁴⁾. Using waste glass ecologically hazardous components are fixed at the molecular level in the silicate phase and the fabricated new glass-ceramic composites possess significantly higher mechanical properties.

The aim of this investigation was to fabricate dense glass ceramic composites using fly ash and waste glass with the potential for its utilization as building material.

RESULTS

Fly ash from the thermal power plant REK Bitola, Republic of Macedonia (from forth zone of electro filter with particle size lower than 63µm) and a type of waste glass from laboratory inventory (particle size lower than 63µm) were used as raw materials for this investigation. The compacts were coded as follows: fly ash - FA, waste glass - WG, FA50WG – glass ceramics composite with glass content from 10 to 50wt.% i.e. FA10WG – composite consisted of fly ash with 10wt.% waste glass). Chemical analysis of the fly ash was carried out by X-ray fluorescence (model ARL 9900XP) and the chemical composition of the waste glass was declared from the manufacturer Pyrex⁽⁵⁾. The chemical compositions of the investigated waste materials are given in Table 1.

Table 1. Chemical compositions of the industrial wastes

	SiO ₂	Al ₂ O ₃	Fe ₂ O ₃	CaO	MgO	Na ₂ O	K ₂ O	SO ₃	B ₂ O ₃	LOI	Σ
FA [wt%]	49.51	17.62	7.91	13.77	3.36	0.69	1.46	3.52	/	1.57	99.41
WG [wt%]	83.34	1.33	/	0.03	/	4.08	0.04	/	11.19	/	100

Fly ash belongs to the silicates due to the evident presence of the SiO₂, Al₂O₃ and Fe₂O₃ as basic oxides constituencies. The level of CaO and SO₃ are relatively high, while the level of MgO and other alkali metal oxides are typical as the other ashes.

The morphology of the fly ash is presented in figures 1. It is evident the presence of primary spherical particles with dimension cca 10µm and particles with irregular geometry with dimensions from 5 to 20µm. Also the presence of agglomerates is evident. The particles of waste glass are with irregular geometry and dimensions from 10 to 60µm, figure 2.

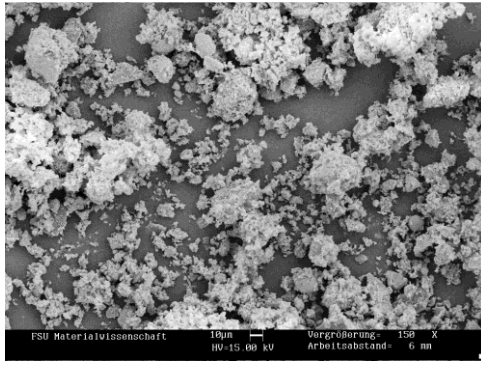


Figure 1. SEM micrograph of the FA, (bar 10µm)

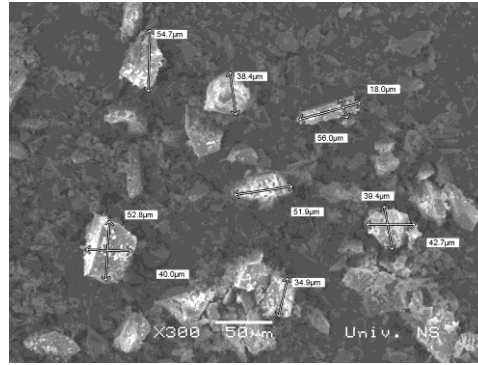


Figure 2. SEM micrograph of the WG, (bar 50µm)

Glass-ceramics composites were fabricated by adding waste glass in quantity from 10 to 50wt.% to the fly ash. One of the reasons was to increase mechanical properties of the composites and secondly to encapsulate the particles of industrial wastes into matrix. Prior to the consolidation the milling and homogenization of the fly ash and waste glass were realized in the planetary mill (Fritsch pulverisette 5) during 60 min. Pressing of the samples was performed by uniaxial press (Weber Pressen KIP 100) at P=45 MPa using PVA as a binder. Dense composites with different densities were obtained by varying the sintering temperatures: 900, 1000 and 1050°C with the holding time at a maximum temperature of 1 hour. The applied heating rate was 10⁰/min. FA50WG composites sintered at 1000°C and 1050°C were deformed. The sintered glass ceramics composites were tested using three point bending tester (Netzsch 401/3) to determine mechanical properties (bending strength and E-modulus).

According the obtained results in this investigation the whole spectrum of the glass ceramics composites were fabricated, but the properties (density, bending strength, E-modulus, porosity and linear shrinkage) of WG (sintered at 700°C), FA and the optimal glass ceramics composites (FA10WG, FA40WG) sintered at 1000°C (chosen as optimal sintering temperature) are presented in Table 2.

Table 2. Sintering temperature, density, bending strength, E –modulus, porosity, and linear shrinkage of fly ash, waste glass and the optimal glass ceramics composites

Compacts	Sinter.temp./ time[°C/h]	ρ [g/cm ³]	σ [MPa]	E [GPa]	Θ [%]	$\Delta L/L$ [%]
FA	1000/1h	1.433	9.41	4.90	43.69	1.96
WG	700/1h	2.233	69.08	27.31	14.43	15.77
FA10WG	1000/1h	1.470	17.98	7.34	42.21	3.05
FA40WG	1000/1h	2.214	63.62	32.31	10.65	13.84

It is evident that glass addition influenced on the incensement of the mechanical properties. Namely, the bending strength of FA is 9.41MPa, but for the glass ceramics composites FA10WG and FA40WG it increased to 17.98MPa and 63.62MPa, respectively. The E-modulus for the composites FA10WG and FA40WG increased to 7.34 and 32.3GPa, respectively in comparison to the pure FA (4.90GPa). The porosity of the FA compacts and FA40WG composites decreases from 43.69 to 10.65%, respectively and the shrinkage increased from 1.96 to 13.84% .

The microstructure of the fractured surface and EDS analysis of the FA10WG composite are presented in figure 3.

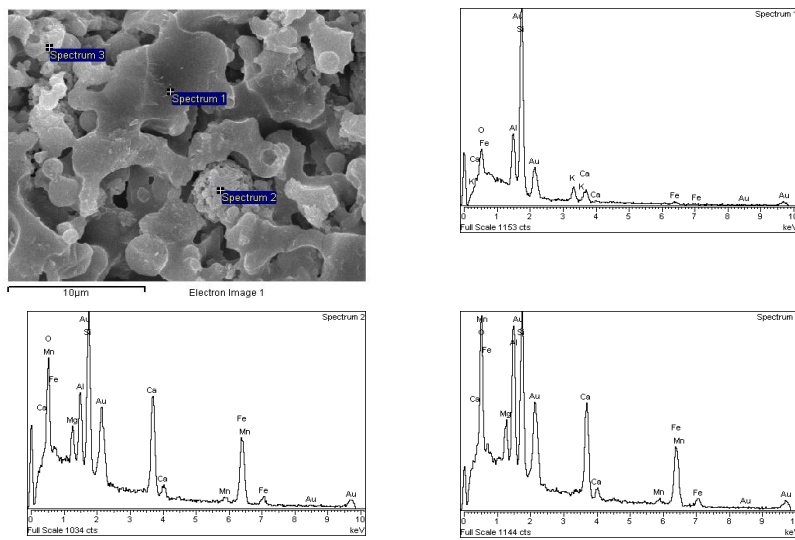


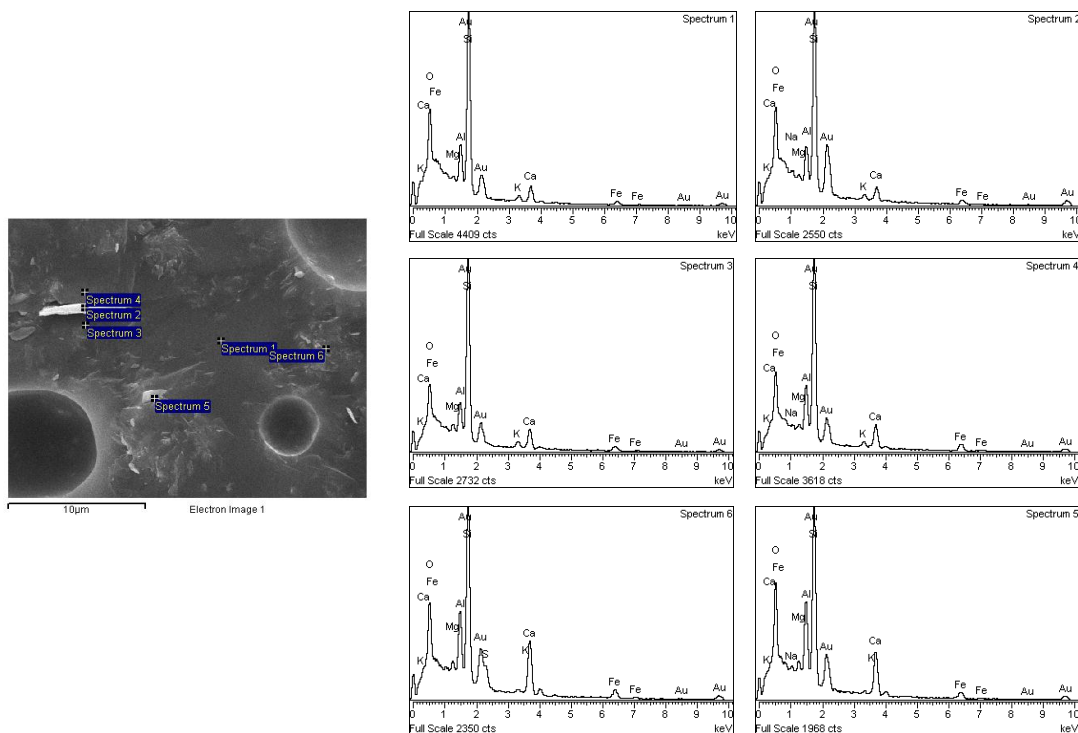
Figure 3. SEM micrograph and EDS spectra (1-3) of composites FA10WG, $t=1000^{\circ}\text{C}$

The fractured surface of the FA10WG composite is granular. It is evident presence of the liquid glassy phase, but also recognisable grains from the original morphology of the FA particles. EDS analysis confirmed that point 2 and point 3 correspond to the FA composition and the point 1 could be characterized as the region of the glassy phase.

Figure 4 shows that the microstructure of the fractured surface of the glass-ceramic FA40WG is homogeneous and smoother in comparison to the FA10WG composite. There are no recognisable grains from the FA and they are well encapsulated in the silica matrix. There is significant formation of closed spherical pores with dimensions between 5-10 μm . The formation of the spherical pores is connected with softening of the glassy phase and evolution of gas ⁽⁶⁾. According to the similarity of the peaks (1-6) from the EDS analysis of glass ceramics composite FA40WG it can be concluded that FA particles are uniformly distributed in the glassy matrix.

CONCLUSIONS

As a general it can be concluded that it is possible to produce dense glass-ceramic composites using high percentage of coal fly ash and waste glass. The new glass-ceramic composites possess significantly higher mechanical properties which make them suitable for a wide range of application in the building industry.



REFERENCES

- [1] G.Ondracek, *Waste treatment and recycling to remineralized products with multibarriers structure*. Monatshefte, 7 273 (1994)
- [2] C.Leroy, M.C.Ferro, R.C.C. Monteiro, M.H.V. Fernandes. *Production of glass-ceramics from coal ashes*. J. of Eur. Cer. Soc. 21 p.195-202, (2001)
- [3] B.Angjusheva, *Production and characterization of glass-ceramics from waste materials*, Qual.of life, 2 (1-2) p.13-20, (2011)
- [4] J.P.Wu, A.R Boccaccini, P.D. Lee, M.J.Kershaw, R.D. Rawlings, *Glass ceramic foams from coal ash and waste glass: production and characterization*. Adv. in App. Cer. 105 1 p.32-39, (2006)
- [5] www.scilabware.com/Glass_technical/, Accessed on 15 June 2011
- [6] M.Ilic, C.Cheeseman, C.Sollars, J.Knight. *Minerology and microstructure of sintered lignite coal fly ash*. Fuel, 82 (30), p.331-336 (2003)

Posters (Wednesday, February 12, 2014 10:15)

Narrow Lead Aprons under Medical Fluoroscopy Procedures

A. Ben-Shlomo

Soreq NRC, Yavne, Israel

INTRODUCTION

Lead aprons are the major protective item of the medical staff whose work involves x-ray exposure. Heart catheterization and angiography procedures represent the most common exposures of the medical staff. The lead equivalent thickness of lead aprons worn by the medical staff is defined by many national standards. The frontal side of the aprons should be 0.25 mm lead equivalent at working conditions under 100 kV, 0.35 mm for working conditions above 100 kV, and 0.5 mm for heart catheterization and angiography. The back side of the body needs less protection and usually is covered by 0.25 mm of lead equivalent. The lead equivalent thickness is defined at the 80 kV level.

Most of the hospital's lead aprons are purchased with general specifications and some of them too narrow and aren't suitable for the body of specific members of the medical staff. It can be assessed in Israel that at least 10% of the medical staff in fluoroscopy rooms are using lead aprons that are too narrow.

Most of the lead aprons in Israeli medical institutions are built in a way that the needed protection of the apron is obtained from two protective layers, each of half the needed lead equivalent thickness. The overlapping of these two layers gives the needed thickness and staff protection. The requirement for the two layer's thickness extends from one side of the body (R LAT) to the other side of the body (L LAT). When the body size is too large for a given apron, the overlapping width of the two layers is reduced and the two lateral sides of the body (along the whole body) get only the half needed protective lead equivalent thickness.

This work is based on Monte Carlo simulation under PCXMC 2.0 software¹. The effective dose calculations were performed for a reference adult (73.2 kg, 178.6 cm), 100 kV, focus to skin distance (FSD) of 100 cm, and entrance surface air kerma of 1 mGy. The number of photons in the simulation was 250,000 (the simulation error was $\pm 0.3\%$).

The radiation spectrum was formed by filtration of a 2.5 mm Al and tungsten target.

The main location of the x-ray source for the medical staff is the imaging volume of the patient, which causes scattered radiation. The simulation radiation angle towards the medical staff was taken as -20° in the cranial-caudal direction (z-axis) and $+45^\circ$ and -45° in the lateral direction (xy plane). These directions were chosen as the typical exposure angles of the staff.

The simulation was performed for whole body radiation (at the above angles) and for partial exposure of the lateral side to simulate the over-exposed area and only one apron layer protection (the field size width at this part of the simulation was one half of the body at LAT view, towards the back, along the full body length). This partial area simulates the half thickness of the protective apron.

The next step after the effective dose simulation was to calculate x-ray penetration through the apron. The calculations were performed for direct x-ray spectrum, using an IPEM spectrum processor². The calculation results give entrance surface air kerma after full apron protection (0.5 mm lead equivalent) and half protection (0.25 mm lead equivalent). Inputs to the calculations include similar kV and basic filtration that are used in the PCXMC 2.0 Monte Carlo simulation. Calculations of the final staff effective dose were obtained from the sum of the full body irradiation and the partial irradiation, using the shielding influence of the full and half protection protective clothing.

RESULTS

X-ray transmission through the protective apron is presented in Table 1.

Table 1: x-ray transmission through the lead apron.

Shielding thickness (mm lead equivalent)	X-Ray transmission (%)
0.25	9.61
0.5	3.02

The overall effective dose was calculated by the effective dose differences of the partial shielding (0.25 mm) and full shielding (0.5 mm) plus the whole body effective dose calculation with full shielding. Table 2 shows the calculation results.

Table 2: Staff effective dose per 1 mGy air kerma outside the apron and projection of -20° in the z-axis.

Lead Apron	Projection	mSv/mGy*
Full cover	AP	0.0152
Partial cover	45° to right	0.0116
Full cover		0.0106
Partial cover	45° to left	0.0134
Full cover		0.0122

It is clearly shown that partial apron cover raises the effective dose of the medical staff.

CONCLUSIONS

It can be assessed in Israel that at least 10% of the medical staff in fluoroscopy rooms are using lead aprons that are too narrow. The medical staff effective dose while wearing inappropriate lead aprons was assessed as an excess of 9-10% under 100 kV x-ray radiation. It can be compared to about double the dose of not wearing thyroid shielding during x-ray fluoroscopy procedures.

REFERENCES

1. **Tapiovaara M., Siiskonen T.** (2007) *A PC-based Monte Carlo Program for Calculating Patient Dose in Medical X-Ray Examinations*. STUK – The Finnish Radiation and Nuclear Safety Authority. Report STUK-A139. Helsinki, Finland.
2. **IPEM (1997).** *Spectrum processor software*, based on IPEM report 78.

Medical Staff X-Ray Dose Reduction by Changing the Patient Examination Side

A. Ben-Shlomo

Soreq NRC, Yavne, Israel

INTRODUCTION

The major x-ray procedures that expose the medical staff at hospitals are angiography and heart catheterization. Most of those procedures take place while the medical staff is standing to the right side of the patient (the patient is lying on his back). It is possible to change some of those examinations and make those invasive procedures on the left side of the patient instead of the right side of his body.

The position of the medical staff influences the staff's x-ray effective dose. The choice of the x-ray projection, as AP, PA, left lateral, or right lateral projections, causes effective dose differences. These differences arise from the asymmetrical positioning of tissues and organs inside the body, x-ray shielding of organs by other organs, and different radiation sensitivity of each organ¹.

The physicians usually stand close to the patient pelvis, keeping some distance from the x-ray source. Thus, standing on the right side of the patient in angiography and heart catheterization usually exposes the left side of their body (in most of the cases, their standing position is not frontal towards the patient's irradiated volume).

Based on anatomical indicators, the traditional concept of building x-ray equipment was to fix the x-ray accessory items at the left side of the patient bed so the medical staff is standing to the right of the patient. Modern x-ray equipment in fluoroscopy rooms for angiography and heart catheterization is built to allow easy and comfortable working from both sides of the patient.

This work shows the differences in the effective dose of the medical staff working in fluoroscopy procedures and standing to the right side of the patient compared to working at his left side. The work is based on Monte Carlo simulation under PCXMC 2.0 software². The effective dose calculations were performed for a reference adult (73.2 kg, 178.6 cm), 100 kV, focus to skin distance (FSD) of 100 cm, and entrance surface air kerma of 1 mGy. The number of photons in the simulation was 250,000 (the simulation error was $\pm 0.3\%$).

The radiation spectrum was formed by filtration of a 2.5 mm Al and tungsten target.

The imaging volume of the patient is the source of scattered radiation towards the medical staff. The simulation radiation angle was taken as -20° in the cranial-caudal direction (z-axis) and $+45^\circ$ and -45° in the lateral direction (xy plane). These directions were chosen as the typical exposure angles of the staff.

The effective dose calculation considers the x-ray penetration through the apron. The calculations were performed for direct x-ray spectrum, using IPEM spectrum processor³. The calculation results produced entrance surface air kerma after full apron protection (0.5 mm lead equivalent). Calculation of the staff effective dose was obtained by using the effective dose of the full body irradiation at the above specific angle and considering the shielding influence.

RESULTS

The standard lead apron thickness for angiography and heart cauterization is 0.5 mm lead equivalent. This protection layer transmits only 3.02% of the x-ray spectrum, formed by tungsten target, 100 kV, and 2.5 mm Al spectrum³.

PCXMC 2.0 effective dose simulation results and the shielding of the protective apron combined to assess the medical staff's effective dose while the staff member stand to the right or left sides of the patient bed.

Table 1: Staff effective dose per 1 mGy Air kerma outside the lead apron and staff irradiation angles of -20° in the cranial-caudal direction (z-axis) and +45° and -45° in the lateral direction (xy plane).

Projection	mSv	45° to left/45° to right projection effective dose ratio (%)
45° to left	0.0122	114.8
45° to right	0.0106	

The results in Table 1 show that standing at the right side of the patient (i.e., exposing the left side of the medical staff member at 45°) causes a larger effective dose than standing at the left side of the patient in the same conditions.

CONCLUSIONS

This work simulate the differences in the effective dose of the medical staff working in angiography and heart catheterization procedures and standing to the right side of the patient compared to working at his left side. This Monte Carlo exposure simulation of the medical staff, while they are standing to the right side of the patient, shows effective dose excess of 114.8% compared to standing in the same conditions at the left side of the patient.

REFERENCES

3. **Ben-Shlomo A., Bartal G., Shabat S and Mosseri M.** (2013). Effective Dose and Breast dose reduction in pediatric scoliosis X-Ray radiography by an optimal positioning. *Radiat. Prot. Dosimetry* 156(1):30-36.
4. **Tapiovaara M., Siiskonen T.** (2007). *A PC-based Monte Carlo Program for Calculating Patient Dose in Medical X-Ray Examinations*. STUK – The Finnish Radiation and Nuclear Safety Authority. Report STUK-A139. Helsinki, Finland.
5. **IPEM** (1997). *Spectrum processor software*, based on IPEM report 78.

DNA Topoisomerase-I Inhibition due to Exposure to X-Rays

R. Daudee¹, R. Gonen¹, U. German¹, I. Orion², E. Priel²

¹*Nuclear Research Center Negev, Beer-Sheva, Israel*

²*Ben-Gurion University of the Negev, Beer-Sheva, Israel*

INTRODUCTION

In events such as radiological terrorism, accidents involving radioactive materials and occupational exposures, there is a great need to identify exposures to relatively low radiation levels. In many situations, the evaluation of radiation doses is not possible using physical dosimeters as they are not worn, and it is desirable to achieve this based on sensitive biomarkers^(1,2,3).

DNA Topoisomerase-I (Topo-I) is an essential nuclear enzyme that is responsible for the topological state of the DNA. The enzyme is involved in a variety of DNA transactions, including replication, transcription, recombination and DNA repair^(4,5). The aim of the present work was to investigate the influence of X-ray radiation on the catalytic activity of this enzyme, and to evaluate its applicability as a biological dosimeter.

RESULTS

Osteoblast-like cell line MG-63 were cultured for 2 days, then harvested to six 50ml sterile tubes. The tubes containing the cells were irradiated using a X-ray source with a dose rate of 1Gy/min for different periods of time. The X-ray source used was an RS-2000 Biological system manufactured by RAD SOURCE company. It produces x-rays with an average energy of about 50keV. After irradiation, the cells were transferred back to the incubator for 2 hours, and then the nuclear protein was extracted from the cells using a common method described in the literature⁽⁶⁾.

The Topo-I catalytic activity was measured using a specific Topo-I reaction mixture which includes supercoiled plasmid as the substrate and nuclear protein extracts as the source of Topo-I⁽⁷⁾. Topo-I relax supercoiled DNA provides topoisomers which are seen by the agarose gel as a ladder of DNA molecules which differ in their topological structure. Equivalent amounts (50 ng) of nuclear proteins were added to a specific Topo-I reaction mixture and the reaction was stopped after 10 min (the reaction activity was calibrated prior to the addition of the nuclear proteins so that the control sample, which was not irradiated, could relax the majority of the supercoiled plasmids).

Figure 1 shows the Topo-I activity assay results of samples exposed to different levels of x-ray radiation, which reveal significant differences in the activity levels between the six samples tested.

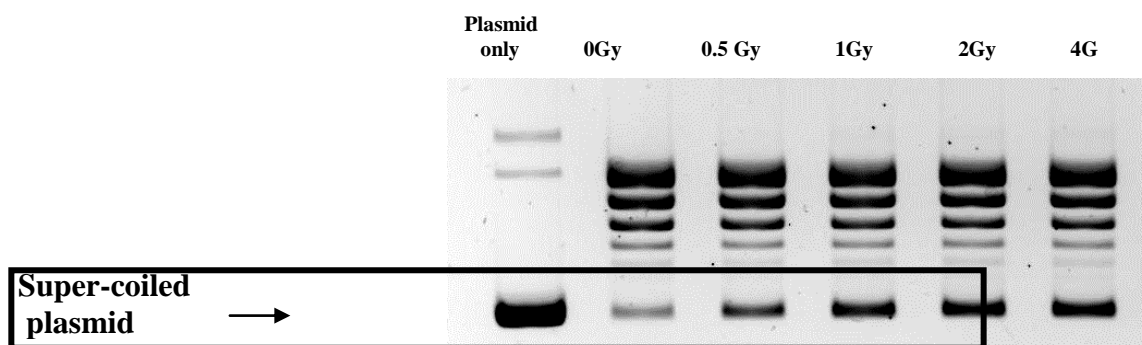


Figure 1: Topoisomerase-I assay results for nuclear extracts of MG-63 cells exposed to different doses of X-ray radiation.

Band intensities were quantified by densitometric scans using EZ-Quant-Gel image processing and analysis software (Figure 2). The inhibition was found to be linear up to a dose of about 1Gy ($r^2 \approx 1$). For exposures

higher than 1Gy there is a significant deviation from linearity, but still, inhibition of the enzyme's catalytic activity can be seen.

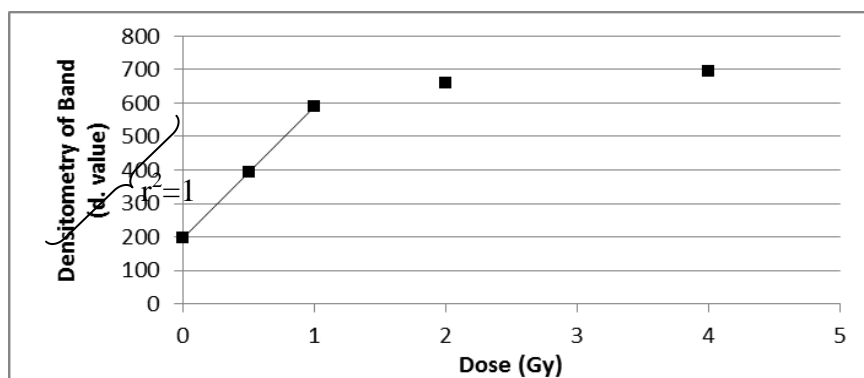


Figure 2: Densitometry results of supercoiled plasmid obtained from Fig. 1

The amount of supercoiled plasmid left after the reaction (see figure 1) was compared to the activity level of the un-irradiated control (0 Gy), that was taken as 100% activity. Figure 3 shows the comparison of the relative activities.

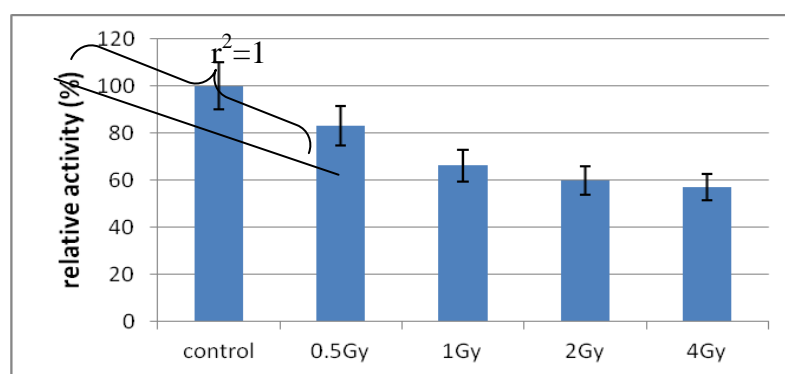


Figure 3: Inhibition of Topoisomerase-I activity after exposure of MG-63 cells to different doses of X-ray radiation.

For purposes of quality control, in order to verify that equivalent amounts of Topo-I were used in the Topo-I assay, the nuclear protein was analyzed by western blot⁽⁸⁾ and reacted with specific anti-topo I and anti β -actin antibodies. Band intensities were quantified by densitometric scans using EZQyant-Gel image processing and analysis software. The relative level of Topo-I protein was calculated using the equation: $[(\text{Topo-I})/(\beta\text{-actin})] \times 100$. The results show no significant differences between the levels of the proteins, leading to the conclusion that topoisomerase-1 activity is inhibited by X-Rays.

CONCLUSIONS

In the present work it was found that exposing MG-63 cells to X-ray irradiation resulted in a significant inhibition of DNA-Topoisomerase-I catalytic activity. The inhibition was found to function in the range of up to at least 4Gy, and up to 1Gy the inhibition was found to be linear with dose. As equal DNA-Topoisomerase-I were used, it is suggested that the cellular mechanism of Topo-I inhibition can be attributed to posttranslational modifications. The reduction in Topo-I activity after exposure to X-ray may be applicable as a biological dosimeter (biomarker) mainly in the range of 0-1 Gy. Further studies are needed to elucidate the limit of detection (LOD) of the dose that can be detected by the enzymes inhibition's activity.

REFERENCES

1. Brooks A.L. *Biomarkers of Exposure and Dose: state of the art*, Radiation Protection Dosimetry, Vol. 97 (1), p.39-46, (2001).
2. Durante M., *Potential application of biomarkers of radiation exposure in nuclear terrorism events*, Physica Medica, Vol. XIX (3), p.191-212, (2003).
3. Guipaud O., Benderitter M., *Protein biomarkers for radiation exposure: towards a proteomic approach as a new investigation tool*. Ann Ist Super Sanita, Vol.45 (3), p.278-286, (2009).

4. James C. Wang, *DNA topoisomerases*, Annu. Rev. Biochem, Vol. 65, p. 635-692,(1996).
5. Champoux JJ., *DNA topoisomerases: structure, function and mechanism*. Annu. Rev. Biochem., Vol 70, p.369-413, (2001).
6. Auer B., Vosberg HP, Buhre U., Klocker H., Hirsh-Kauffman M., Shweiger M., *Intracellular distribution of DNA topoisomerase I in fibroblasts from Fanconi patients*, Hum. Genet, Vol. 61, p.369-371, (1982).
7. N. Noach, Y. Segev, I. Levi, S. Segal, E. Priel, *Modification of topoisomerase I activity by glucose and by O-GlcNAcylation of the enzyme protein*, Glycobiology, Vol.17(12), p.1357-1364, (2007).
8. J. Sambrook, Fritch EF, Maniatis T., *Molecular cloning: a laboratory manual*, Cold spring Harbor, NY: Cold spring Harbor Laboratory Press, (1989).

Posters (Wednesday, February 12, 2014 15:30)

A Program for Follow-Up and Quality Assurance of Electret Results

B. Sarusi¹, S. Levinson¹, N. Lavi², U. German¹

¹ Nuclear Research Center, Negev, P.O.B 9001 Beer Sheva, 84190, Israel

² Ben-Gurion University of the Negev, Beer Sheva, 84105, Israel

INTRODUCTION

The most important naturally occurring radio-nuclides in the environment are ^{40}K and ^{238}U and ^{232}Th , which are heads of decay series. Building materials may also contain enhanced levels of naturally occurring radioisotopes which may be sources of external and internal radiation exposure in dwellings. The external exposure is due to the direct radiation from the radioisotopes in the decay series of ^{238}U and ^{232}Th , and among these daughters, two Radon isotopes are produced: ^{222}Rn is a daughter in the chain of decay of ^{238}U and ^{220}Rn is a daughter in the ^{232}Th chain. Radon is a gas, it undergoes diffusion in the building material and exhalation to the surrounding. Besides, radon is emanated also from soil and its concentration can be significant in radon prone areas. Inhalation of air with increased level of Radon causes internal exposure, which is the greatest contribution to the exposure of individuals to natural radiation. Therefore, accurate measurement of radon concentration is of great importance.

There are several methods to determine the radon concentration in air. The Israeli regulation for measuring the radioactive content in building materials⁽¹⁾ specifies three methods for radon concentration measurements: applying continuous monitoring, using Electrets and using active charcoal cassettes. Using Electrets is convenient, as a relatively simple stand-alone system can be used. The follow-up and quality assurance of Electrets results is the subject of the present work. For this purpose a computer program was developed which handles the Electrets results database and applies various tools for analysis.

MATERIALS AND METHODS

An Electret is a charged Teflon® disk, mounted inside a small chamber^(2,3). Radon gas diffuses into the chamber through filtered inlets, and the alpha particles emitted by the decay ionize air molecules. Negative ions produced inside the chamber are collected on the positively charged Electret, causing a reduction of its surface charge. Thus, the Electret serves both as a source of electrostatic field and as a sensor. The change in voltage, which is a function of the radon concentration, is measured by a sensible voltage reader. In the present work EIC's (Electret ion chambers) made by Rad Elec Inc. (5714-C Industry Lane, Frederick, MD 21704, USA) were used. The basic components of the E-PERM® Electret system are shown in Fig.1. The Electrets are accurate devices, but they are susceptible to some environmental effects, which may induce significant errors. The main effects are mechanical shocks, dirt/dust, humidity^(4,5,6). Also improper operation of the shutter handle when measuring the voltage may produce results deviating from the proper values. Therefore, at least 2 equal sequential measurements are needed for a valid result.



Figure 1. The E-PERM® Electrets system

THE COMPUTER PROGRAM

The general flow chart of the computer program is presented in Fig. 2. The main database contains information on each Electret, characterized by its unique serial number. All Electrets readings are displayed, as well as the time of reading, the readout equipment used and the reading status (voltage follow-up, voltage check before exposure, readout after exposure, etc.). All historical data is contained in the database, from beginning of use of each Electret. to ensure reliable check points and quality assurance of the reader, reference Electrets are also defined in the system. These are highly stabilized Electrets and in addition a blank Electret. Full information on the reference Electrets and their history is included in the database as well.

The database is used to check compliance with all the requirements of the manufacturer and the regulator (ministry of environmental protection) and to issue proper alerts for action. New Electrets come loaded to 700 – 780 volts which allows for 500 usable volts. A valid Electret reading must be higher than 200V, otherwise it must be sent back to the manufacturer for charging. In order to ensure a correctly functioning reader, weekly readings of reference Electrets should be within $\pm 3V$ of the manufacturer certified readings and the blank ("zeroing") Electret reading should be in the range $\pm 2V$. The warning limits can be changed by the administrator of the system, but not by the operator.

The program establishes communication between the reader and the database. The Electret number is written in barcode format and is transmitted directly to the database. Also the voltage values are received from the reader and are input automatically into the database.

A valid reading is defined as the value of two consecutive equal voltages out of up to 10 readings. In order to facilitate the follow-up, to enable an efficient handling of problems, and to observe trends, a graphical presentation of the voltage readings as a function of the reading time is available.

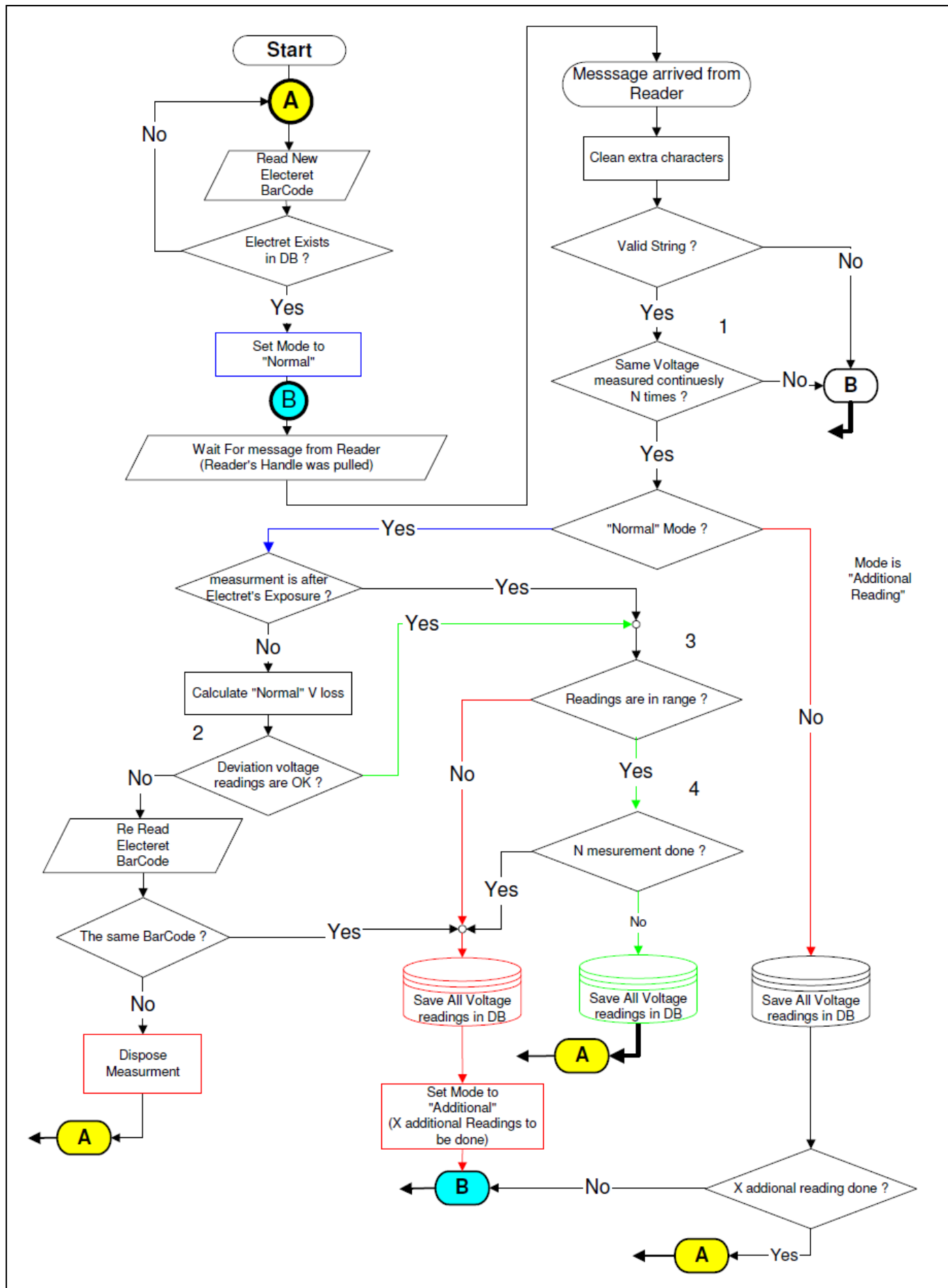


Figure 2. Flow chart of the computer program.

EXAMPLE OF RESULTS

Two typical graphic presentations are given. The first one (Fig. 3) presents data of a valid radon exposure measurement. Before exposing the Electrets, the voltage values are stable. Also after exposure the voltage remains stable and the radon concentration can be calculated from the voltage difference before and after the exposure. A different case can be seen in Fig. 4.

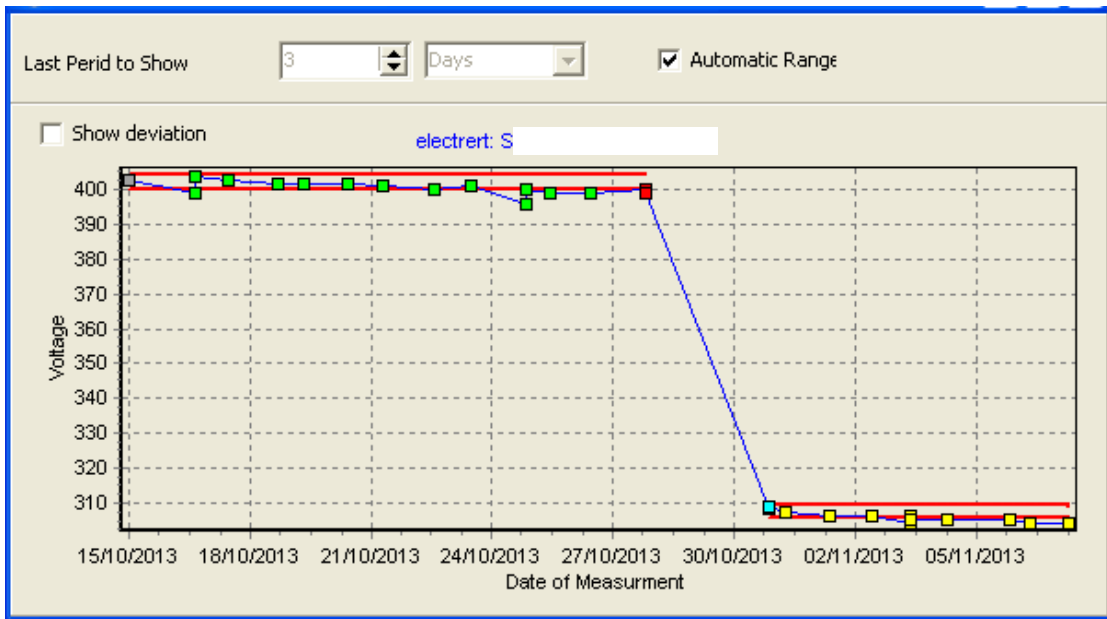


Figure 3. Data of a valid radon exposure measurement.

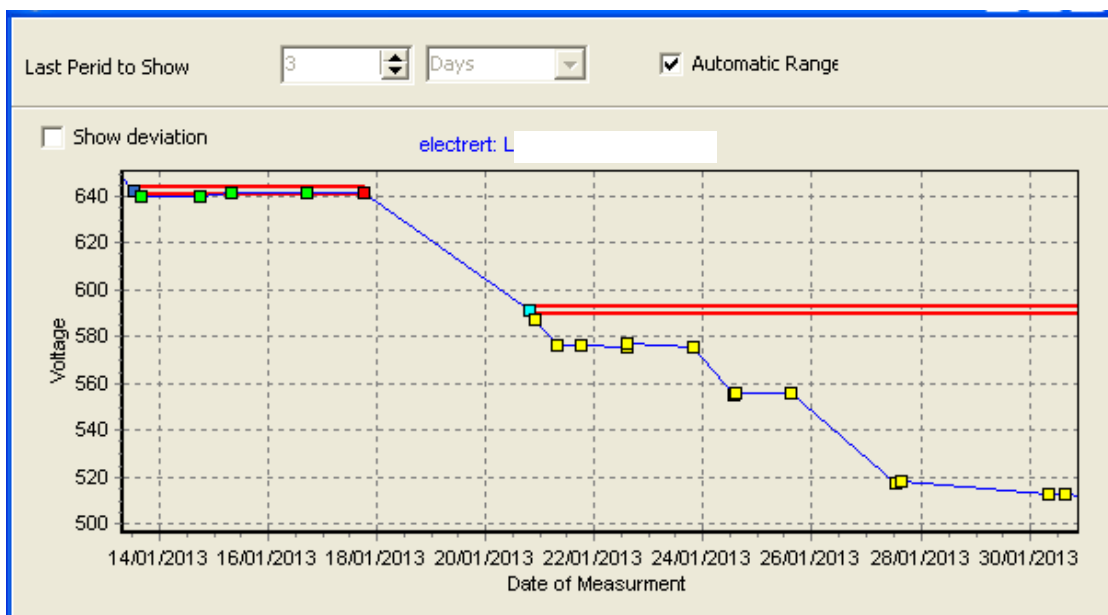


Figure 4. Data of an invalid exposure measurement.

Before the exposure the voltage was stable, but after the exposure there is a non-normal behavior. The first two readings were close, but afterwards a slip of about 15V occurred. The next 4 readings were stable, but then another drift occurred. This behavior does not allow us to determine with acceptable accuracy the radon concentration. It is possible that this drift was caused by some dirt accumulated on the Electret during its use.

CONCLUSIONS

A computerized tool was developed which greatly improves the handling and follow-up of data used to evaluate the radon concentrations by Electrets. The voltage readings are directly placed into the database, statistical analysis is performed and the validity of the readings are checked. All readings of the reference Electrets are included in the database as well. The graphic presentation of data enables a clear observation of behavior and trends. Using the program greatly improves the quality assurance of radon concentration determination when using Electrets. The program is under development. Its expansion will include calculations of radon concentrations based on the voltage readings.

REFERENCES

1. SI 5098, 2009. Content of radioactive elements in building products. The standards institution of Israel.
2. Kotrappa, P., Brubaker, T., Dempsey, J.C., Stieff, L.R., 1992. Electret ion chamber system for measurement of environmental radon and environmental gamma radiation. *Radiation Protection Dosimetry* 45, 107–110.
3. US Patent nr. 4,992,658. Ramsey Jr. et al. 1991.
4. Denman, A.R., Groves-Kirkby, C.J., Phillips, P.S., Krockett, R.G.M., Woolbridge, A., Gillmore, G.K., 2005. The practical use of Electrets in a public health radon remediation campaign. *J. of Envir. Radioactivity*, 84, 375-391.
5. Mahat, R.H., Bradley, D.A., Amin, Y.M., Wong, C.Y., Su, L.D., 2001. The effect of humidity on the accuracy of measurement of an Electret radon dosimeter. *Radiat. Phys. Chem.* 61, 489–490.
6. Sorimachi, A., Takahashi, H., Tokonami, S., 2009, Influence of the presence of humidity, ambient aerosols and thoron on the detection responses of Electret radon monitors. *Rad. Measurements* 44, 111-115.

Posters (Wednesday, February 12, 2014 15:30)

Application of the "GammaGen" Computer Code for NORM Synthetic Spectra Analysis

B. Sarusi¹, S. Levinson^{*1}, U. German¹, S. Antropov², K. Kovler³

¹*Nuclear Research Center, Negev, P.O.B 9001 Beer Sheva, 84190, Israel.*

²*"Amplituda" Research Center, POB 120, Moscow 124460, Russia*

³*Technion - Israel Institute of Technology, Haifa 32000, Israel*

INTRODUCTION

"GammaGen" (GG) is a computer software developed to simulate gamma ray spectra obtained from NaI(Tl) or Ge detectors. The detector efficiency, resolution and peak to Compton ratios are used to generate synthetic pulse height spectra for specific detector and geometrical configurations.

GG was used in the past for several applications, as to predict the detector response to different radio-nuclides mixtures [1-3], to predict the pulse height spectra near a nuclear spent fuel site as a function of the shielding thickness and cooling time [4] and for homeland security purposes [5, 6]. An updated version of the GG program was developed, and the application presented in the present work consists of building a library and simulating the detection and analysis of synthetic spectra to check the performance of a commercial spectrometry system based on a NaI(Tl) detector intended for NORM analysis, which was developed by *Amplituda/Russia* [7].

MATERIALS AND METHODS

The basic application of the GG computer program is to generate a calculated spectrum, mainly for complicate cases of many photo-peaks from different radioisotopes mixtures, for visual inspection and comparison with measured spectra. The spectrum for a chosen radio-nuclide is generated based on its activity and its photo-peaks energies and yields taken from a data library such as the "Raddecay" program [8]. The detector efficiency, resolution and the peak to Compton ratios are determined specifically for a certain detector system, as well as the counting geometry which is chosen by the user. The spectra can be displayed in several modes: as energy lines of the photo-peaks, as Gaussians of each photo-peak, or as sum of all Gaussians. Compton distributions of the predicted accumulated counts in each channel can be included. The resulting spectra are displayed for visual analysis together with peaks and radio-nuclides data. All spectra can be exported to formats required by commercial spectra analyzing programs and to Excel format.

THE COMPUTER PROGRAM

This new version of the GG program simulates the multichannel analyzer (MCA) operation. According to the activity determined for each radionuclide and the counting time, the GG program displays the spectrum accumulation as it is done in MCA. The counts are summed to a temporary variable as a function of time. If the count is greater than 1, Gaussian randomization is performed based on the normal standard deviation and if the random value is greater than 1 its integer value is added to the previous counts of the specific channel. The temporary variable is cleared for the next iteration. The same procedure is done for all the spectrum channels and the accumulation progress is refreshed and displayed every second, which is the basic unit time. This way, the channel content of spectra of low activity samples may be updated only after several seconds, as it really occurs in actual counting systems. The user can control the accumulation procedure with all the features that are in common MCA systems.

The "Progress" program developed at *Amplituda/Russia* [5] is commonly used to analyze NORM spectra, including the ¹³⁷Cs radionuclide. The analysis is basically performed by the Linear Least Squares technique on 12 Regions of Interests (ROIs) [9, 10]. Its library was replaced by a synthetic, calculated library consisting of NORM radioisotopes and ¹³⁷Cs, prepared by the GG program. The "Progress" program was applied to analyze complex pulse height spectra, also prepared by the GG program with statistical fluctuations taken into consideration.

EXAMPLE OF RESULTS

A spectrum of the NORM materials ^{226}Ra , ^{232}Th , ^{40}K with an activity of 1000 Bq/kg each, with added 1000 Bq/kg of ^{137}Cs in 1 liter Marinelli container [11] for 10 minutes counting time was calculated by the GG program, when using a NaI(Tl) flat 3"x3" detector (as installed in the "Progress" system). The spectrum was transferred and analyzed by the "Progress" program, that was pre-calibrated for this specific geometry and detector characteristics by GG spectra. In figure 1 the predicted "measured" spectrum and the analyzed and fitted spectrum by the "Progress" program are given. The analysis results reported by the "Progress" program can also be seen in the insert. Table 1 summarizes the "Progress" analysis results. It can be seen that for all radio-isotopes the accuracy is better than about 2%, except for ^{40}K where the difference from the target value is about 2.5%. However, also the standard deviation of the calculated ^{40}K activity is much higher than for other radio-isotopes (more than 5% compared to about 1%), indicating a lower statistical accuracy of the counts in the ^{40}K energy peak.

Table 1. The accuracy of the analysis performed by the "Progress" program on a simulated spectrum of a mixture of 1000 Bq/kg NORM radio-nuclides and ^{137}Cs .

Radio-nuclide	Calculated content [Bq /kg]	Difference [%]
^{226}Ra	1020.6 ± 8.7	2.06
^{232}Th	1001.6 ± 10.3	0.16
^{40}K	974.8 ± 52.6	2.52
^{137}Cs	999.6 ± 8.3	0.04

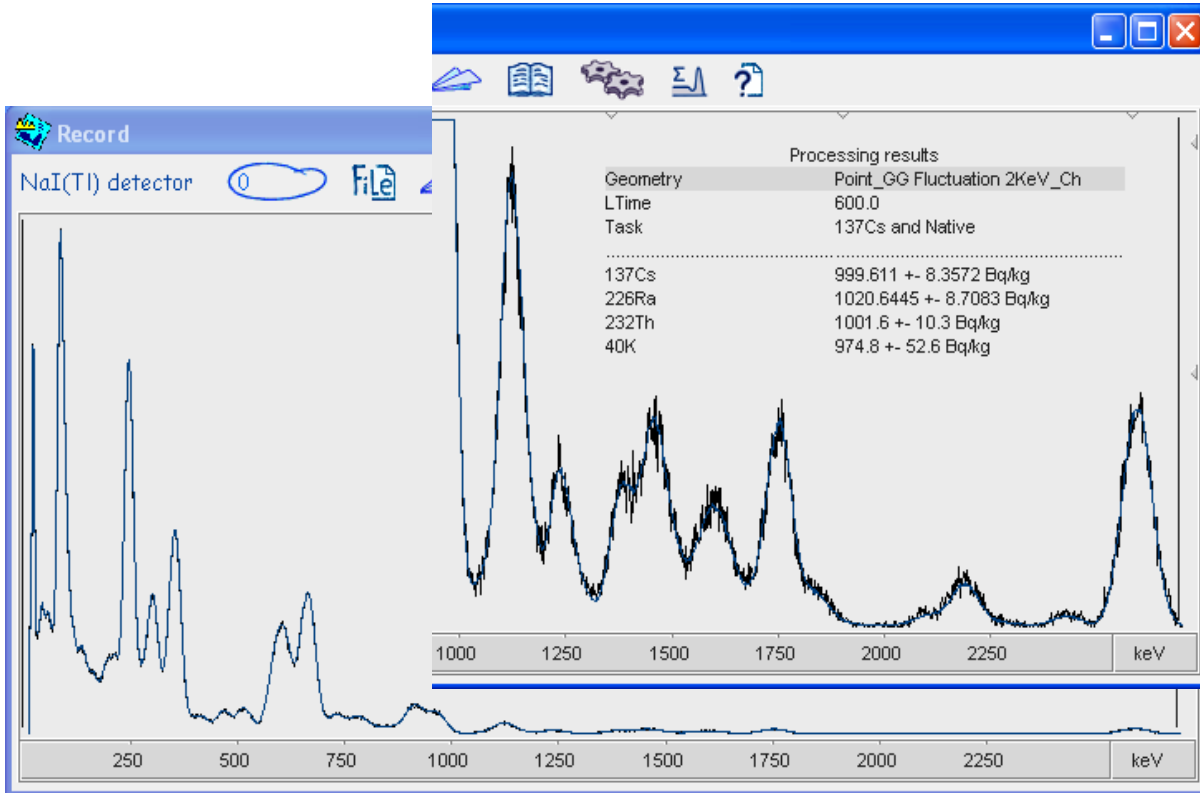


Figure 1: NORM + ^{137}Cs NaI(Tl) spectrum created by GG program and analyzed by the "Progress" program.

CONCLUSIONS

The new version of the GG program enables prediction of "real" spectra, including counting statistics. It simulates the operation of the multichannel accumulation process. The program was used to prepare the library components of the commercial "Progress" analysis system, in order to check its performance when analyzing NORM spectra. The "Progress" program was applied to analyze a synthetic mixture of 1000 Bq/kg of NORM materials+¹³⁷Cs contained in a Marinelli beaker, and the results for all radio-isotopes were obtained within an accuracy range of 2.5%

The new version of the GG program enables future investigations of counting and analyzing complex spectra, especially in the case of NaI(Tl) detectors, where significant overlapping may occur. Producing synthetic spectra can be used for example to determine the MDA of radio-nuclides in complex mixtures with various activities. The main advantage is that no sample preparation is needed, as well as no laboratory work.

REFERENCES

1. "GammaGen - a computer code for gamma-ray spectra generation". S.Levinson, B. Sarusi, O. Pelled, U. German. The 24th conference of the nuclear societies of Israel, Dead-Sea, Israel, February 19-21, 2008, p.137-140
2. "Simulation of pulse height spectra from NaI(Tl) and Ge detectors near the location of a nuclear reactor accident". S.Levinson, U.German, B.Sarusi, O.Peled. IRPA Regional Congress for Central and Eastern Europe, Brasov, Romania, 24-28 September 2007, p. 261
3. "A computer code for synthetic gamma-ray spectra generation". S. Levinson, B. Sarusi, O. Peled, U. German. IRPA-12 international congress of the international radiation protection association, Buenos-Aires, Argentina, 19-24 October 2008, TS I.1.1-2418, p. 31
4. "Gamma-ray spectra prediction for radioactive waste". S. Levinson, B. Sarusi, O. Peled, U. German, Z. Alfassi. MRS Materials research society, the 33nd international symposium, scientific basis for nuclear waste management, Saint Petersburg, Russia, 24-29 May 2009, RP-21, p. 177
5. "Synthetic gamma ray spectra for homeland security radio-nuclides analysis". S.Levinson, B.Sarusi, A.Osovizky, V.Pushkarsky, U.German, E.Marcus, Y.Cohen, I.Belaish. Nuclear science symposium Medical Imaging conference, Orlando, Florida, U.S.A, 25-31 October 2009, N13-81, pp. 504-508
6. "Homeland security - masking of special nuclear materials (SNM) by Natural Occurring Radiation Materials". B.Sarusi, S.Levinson, A.Osovitzki, U.German, T.Mazor, Y.Cohen, I.Belaish. The 25th conference of the nuclear societies in Israel, 16-18 February 2010, Dead-Sea, Israel, pp. 249-253
7. "Amplituda" Research Center, POB 120, Moscow 124460, Russia
8. "Raddecay", Version 3 March 1999. <http://rad-decay.software.informer.com>.
9. "Determination of Radionuclide Content of Building Materials by Means of Scintillation Spectrometry". K. Kovler, Z. Priluzky, S. Antropov, N. Antropova, V. Bozhko, Z. Alfassi, N. Lavi. The 25th conference of the nuclear societies in Israel, 16-18 February 2010, Dead-Sea, Israel, pp. 284-289
10. "Can scintillation detectors with low spectral resolution accurately determine radionuclides content of building materials?" K. Kovler, Z. Prilutskiy, S. Antropov, N. Antropova, V. Bozhko, Z.B. Alfassi, N. Lavi. Applied Radiation and Isotopes 77 (2013) 76-83
11. Isotrak Nuclitec Eckert & Ziegler, Germany, 1 liter Marinelli beaker type 1N FZ-1262-001 with internal hole of 77 mm dia.

Posters (Wednesday, February 12, 2014 15:30)

Matrix Materials for Preparation of Marinelli Calibration Standards

S. Levinson¹, N. Lavi², U. German¹

¹ Nuclear Research Center, Negev, P.O.B 9001 Beer Sheva, 84190, Israel

² Ben Gurion University of the Negev, Beer Sheva, 84105, Israel

INTRODUCTION

Due to the very low concentrations of radioactive nuclides in environmental samples (soils, water, plants, building materials, etc.) high volume samples are used when employing γ -ray spectrometry. A convenient procedure is to employ Marinelli beakers, which surround the spectrometer and enhance the detection efficiency. The spectrometry system must be calibrated to the Marinelli beaker geometry, but due to the great variety of the environmental samples, their density may vary in the general range $0.2 - 2 \text{ g cm}^{-3}$. Variability in the sample chemical composition is not a major problem, since mass attenuation coefficients differ only slightly from one environmental sample to another, but the wide range of densities results in large differences in γ -ray attenuation factors within the samples. Therefore, measurements of radionuclides from environmental samples by γ -ray spectrometry require a correction for self-attenuation of γ -rays. This correction can be minimized or avoided by direct calibration with certified γ -ray standard sources in matrices with a composition close to that of environmental samples to be assayed. The preparation of the standards can be made using "in house procedures". This can be done by homogeneously incorporating certified standard radionuclide sources into inactive matrices with a composition and density as close as possible to the samples.

Many possible matrices are described in the literature for preparation of the Marinelli standards. De Sanoit⁽¹⁾ describes the preparation and characterization of a low density (0.27 g cm^{-3}) silica matrix spiked with mixed γ -ray standards. Daraban et. al⁽²⁾ used a composition of CaCO_3 , CaSO_4 , SiO_2 and Al_2O_3 to simulate "artificial soil". Lavi and Alfassi⁽³⁾ proposed CaCO_3 for a matrix with a density of $1.1 - 1.3 \text{ g cm}^{-3}$ mixed with known amounts of ThO_2 . The Netherlands Standard for radioactivity measurements in building materials⁽⁴⁾ mentions stearic acid, starch, gypsum and quartz powder as suitable matrix materials. Taskaeva et.al⁽⁵⁾ gave a detailed description on preparation of low activity efficiency calibration standards of different densities with natural organic and inorganic materials, including widespread food products as coffee, sugar and honey.

The Marinelli matrix density is indeed an important parameter which influences the calibration accuracy, but the natural radioactivity content of the various added bulk materials may also contribute by adding spurious background to the spectra originating from the certified γ -ray emitting radioisotopes, as the calibration for NORM determination is usually performed with very low standard activities. In the present work, an investigation of the specific activity content in selected inorganic and natural organic products regarded as potential matrix materials was performed. As the main natural occurring radioisotopes are ^{226}Ra , ^{232}Th and ^{40}K , their specific activity in the various samples was measured. ^{137}Cs which was added in the last decades to the environment due to the increased nuclear activity was measured as well.

MATERIALS AND METHODS

Marinelli beakers of 1 liter volume supplied by Isotrak- Ekert & Ziegler were used. The bore diameter of these beakers is 79 mm and fits to the 2.75” diameter of the HPGe detector employed in this work (Ortec, 20% efficiency). The samples were counted several times (50,000 to 300,000 sec) in order to achieve a desirable statistical accuracy.

The following samples were analyzed :

- Sand collected from the shore of the Mediterranean Sea
- White Sugar
- White Flour
- Several organic food products: Rice, Maize (corn), Red and green Lentils, White beans, Broad beans and Humous beans and green Pea.

The samples were grinded to a fine powder, were homogenized and transferred to Marinelli standard beakers. The content of each beaker was compressed to obtain maximum density and the beakers were tightly closed, The counting was delayed for 21 days to allow equilibrium between ^{226}Ra and its daughters, due to Radon emanation from the natural ^{226}Ra . The system was calibrated using a standard ^{226}Ra 1 liter Marinelli beaker with an activity of 3080 Bq and density of 1.08 gr cm^{-3} .

RESULTS AND DISCUSSION

The ^{226}Ra , ^{232}Th and ^{40}K activity in the samples checked is presented in Figures 1-3. The specific weights of the various samples are given in Table 1.

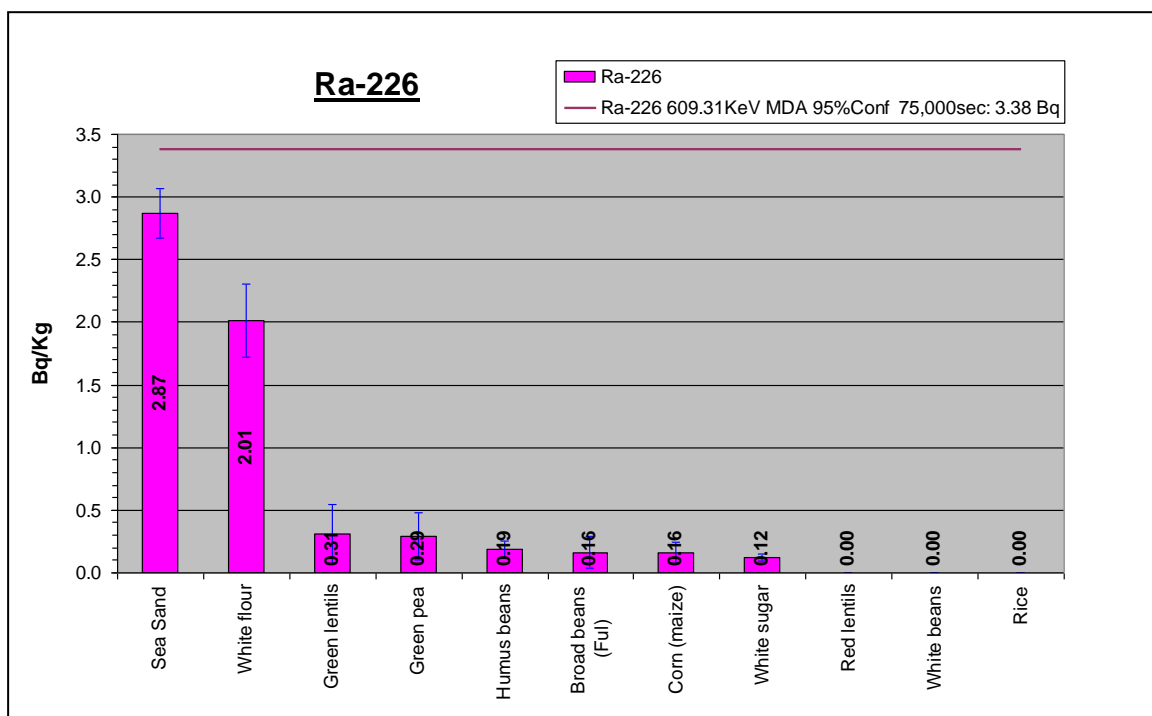


Figure 1: The ^{226}Ra specific activity of the different samples.

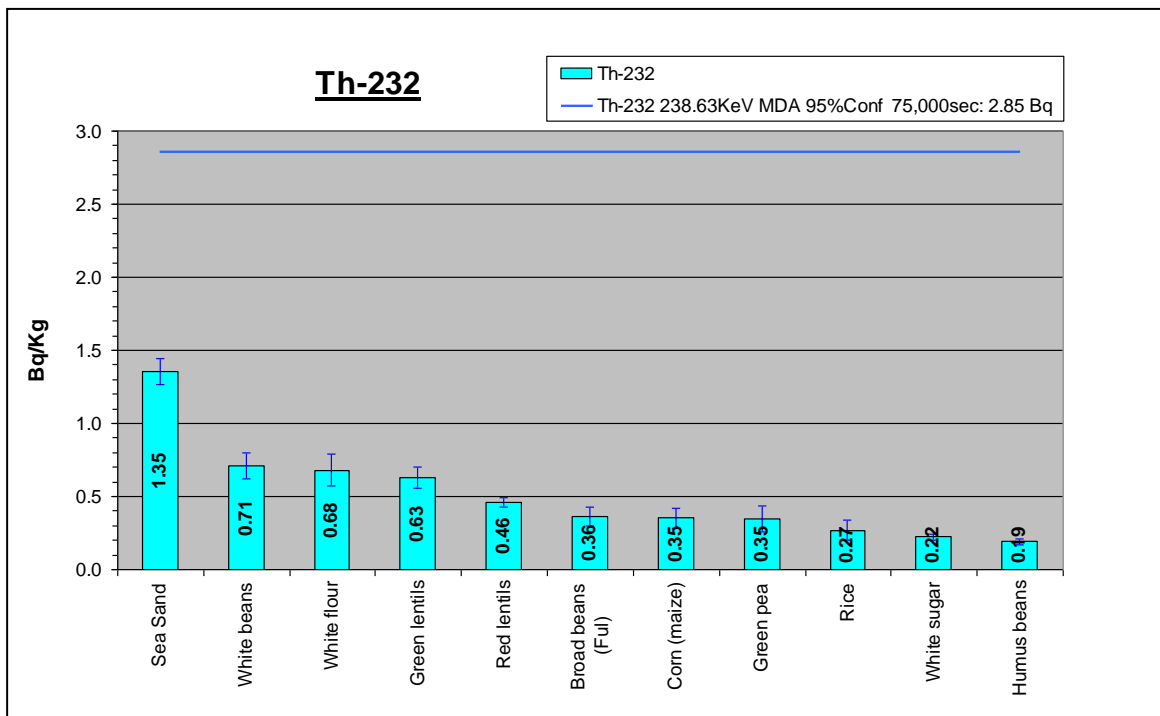


Figure 2: The ^{232}Th specific activity of the different samples.

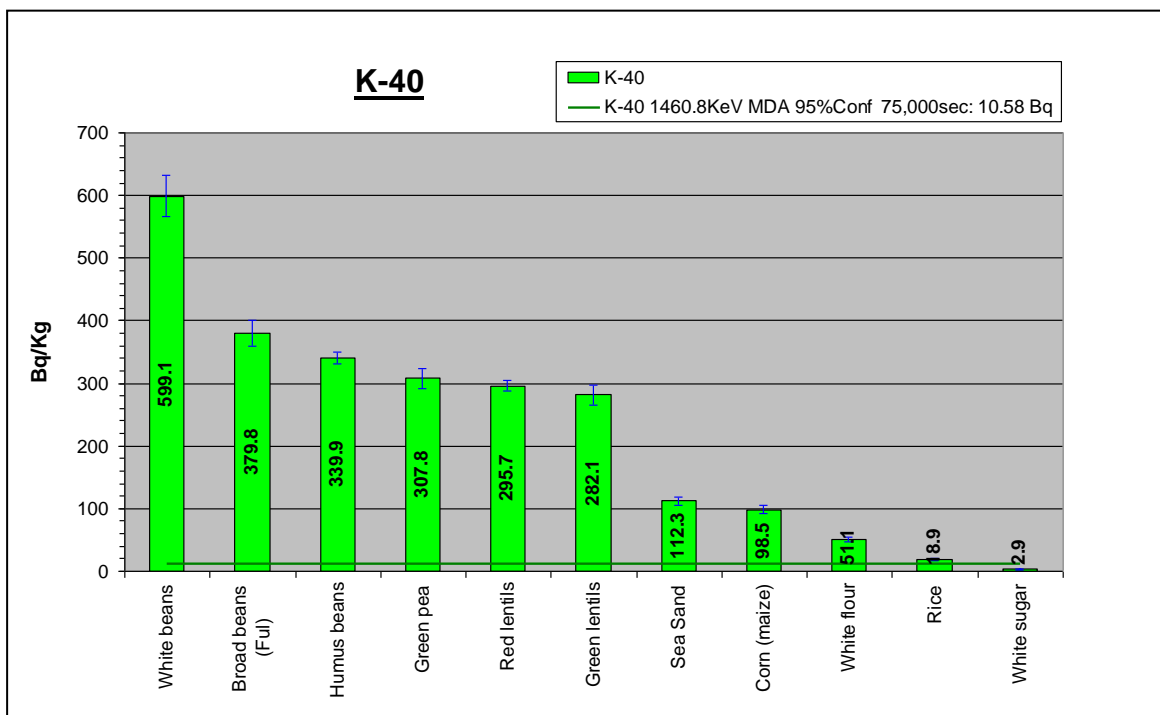


Figure 3: The ^{40}K specific activity of the different samples.

Table 1: Specific weight of the checked materials

	White	Broad	Humus	Red	Corn	White	Rice	Green	Green	Sand
Material	flour	Beans (ful)	beans	lentils	(maize)	sugar		lentils	pea	
Density (kg/liter)	0.78	0.84	0.92	0.94	0.95	0.98	1.03	1.04	1.04	1.83

DISCUSSION

It can be seen that except sea sand, white flour and broad beans the specific weight of all samples is in the range 0.9 - 1.1 kg L⁻¹. However, significant differences are present regarding the radio-nuclides content. The ²²⁶Ra and ²³²Th activity for all samples is below the MDA value for the applied counting time. However, the ⁴⁰K content is considerably higher in all samples, the highest value being 599 Bq kg⁻¹ in white beans and only 2.9 Bq kg⁻¹ in sugar. Traces of ¹³⁷Cs (0.006 Bq kg⁻¹) were found only in the sand sample. It seems that grinded white sugar is the best choice for matrix material, with the lowest NORM concentration and density close to 1.

REFERENCES

1. de Sanoit J., Silica spiked with mixed γ ray standards for use as environmental reference material. *Radiochimica Acta* 65, 249-257, 1994.
2. Daraban L., Iancu D. Nita D., Daraban L., Efficiency calibration in γ spectrometry by using ²³²Th series radionuclides. *Rom. Journ. Phys.* Vol 58, Suppl. P, S99-S107, 2013.
3. Lavi N., Asfassi Z.B., Development of Marinelli beaker standards containing thorium oxide and application for measurements of radioactive environmental samples. *Rad. Measurements*, 38, 15-19, 2005.
4. NEN 5697, Radioactivity measurements-Determination of the natural radioactivity in stony building materials by means of semiconductor gamma-ray spectrometry. Netherlands Standard, 2001
5. Taskaeva M., Taskaev E., Penev I., On the preparation of efficiency calibration standards for γ -ray spectrometers. *Appl. Radiat. Isot.*, Vol 47, 981-990, 1996.

Posters (Wednesday, February 12, 2014 15:30)

Radioactivity in Soils and Foodstuff Samples in Israel

S. Levinson¹, N.Lavi², H.Nasar³, U.German¹

¹ Nuclear Research Center, Negev, P.O.B 9001 Beer Sheva, 84190, Israel.

² Ben Gurion University of the Negev, Beer Sheva, 84105, Israel.

³ Ministry of Environmental Protection, Jerusalem POB 34033, Israel

INTRODUCTION

A new series of measurements was performed to determine the current NORM radionuclide content in cultivated soils and selected foodstuff. An HPGe detector (EG& G Ortec) system with a 20% efficiency (relative to 3"x3" NaI(Tl) at 1332 keV) was used for gamma ray spectrometry. Due to the low amount of radioactivity in natural materials, 1 liter of soil samples were measured in Marinelli beakers as well as the foodstuff samples which were concentrated and homogenized. Calculation of the radioactivity transfer factors from the cultivated soils to foodstuff was performed on the basis of dry weight data, as described elsewhere in the literature [1,2]. In order to ensure the equilibrium of ²²²Rn and its daughters in the ²²⁶Ra chain, the measurements were performed after a waiting time of at least 21 days.

MATERIALS AND METHODS

The foodstuff and soil samples were collected from several locations in Israel: Ein Carmel (North), Nehalim, Beerot Ytzhak and Bne Atarot (Center) and Arad (South). The samples of cultivated soils were taken from the top 5 cm of the soil, were dried at 105° C, homogenized and transferred into Marinelli Beakers of 1 liter [3]. Two types of foodstuff samples were prepared from each sampling place and were transferred to Marinelli beakers for counting:

- 1) Samples in natural form (raw materials) grinded and homogenized.
- 2) Samples dried and blended to fine powder. The average drying temperature was 150° C, which differs from a previous technique that was used in the past [4]. The drying process took about 16 hours and required continuous blending.

γ spectrometry was performed for all samples, after calibration for the Marinelli beaker geometry. In order to get acceptable counting statistics the measurements lasted between 8 and 80 hours, depending on the radioactivity content in the samples. The appropriate background was subtracted from each spectrum and density corrections were applied.

RESULTS AND DISCUSSION

Fig. 1 presents the ratio of the dry foodstuff weight to the natural weight, defined as the dryness fraction. The sort of foodstuffs and their collection location are noted in the figure. The dryness fraction obviously depends on the kind of foodstuff. It varies in the range from 4.5% to 22.1% with an average value of about 12%.

The specific activity of the dried soil samples from the various locations is given in Fig. 2. The average activity of ²²⁶Ra is 12.72 Bq/kg, of ²³²Th is 23.10 Bq/kg and of ⁴⁰K is 245 Bq/kg. The contribution of ¹³⁷Cs, which became significant after the Chernobyl accident, can also be seen with an average activity of 3.77 Bq/kg.

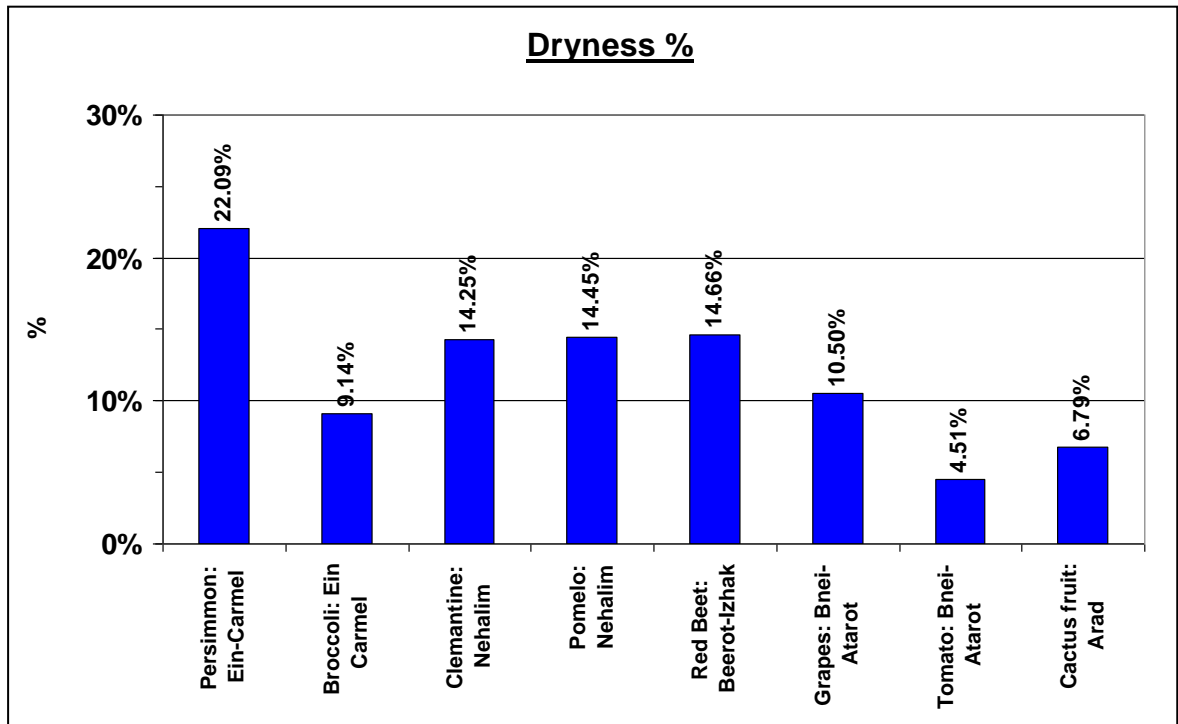


Figure 1: Dryness fractions of various foodstuffs.

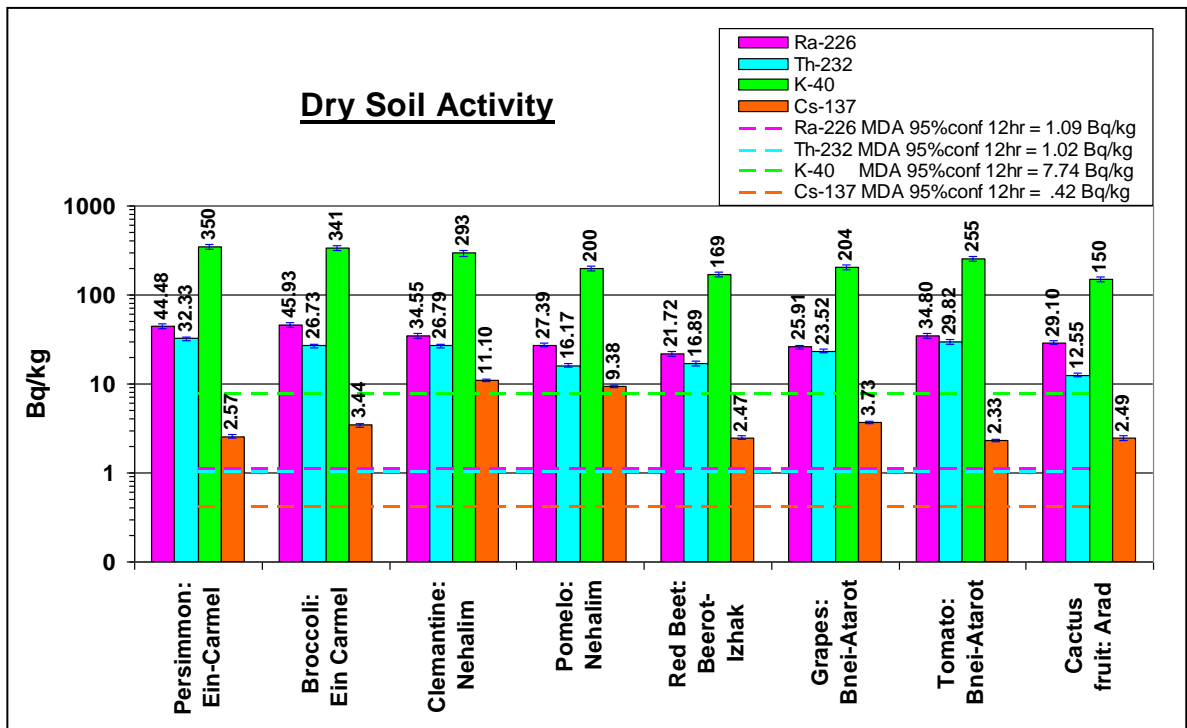


Figure 2: The specific activity of the soil samples from different locations.

Due to the great variation in dryness fraction between the different foodstuff sorts, it is important to notice the differences between the specific activities normalized to the natural weight (as consumed) and normalized to the dry weight (the actual plant specific activity). Both specific NORM activities for the selected foodstuffs can be seen in Fig. 3. No measurable ^{137}Cs amounts were detected.

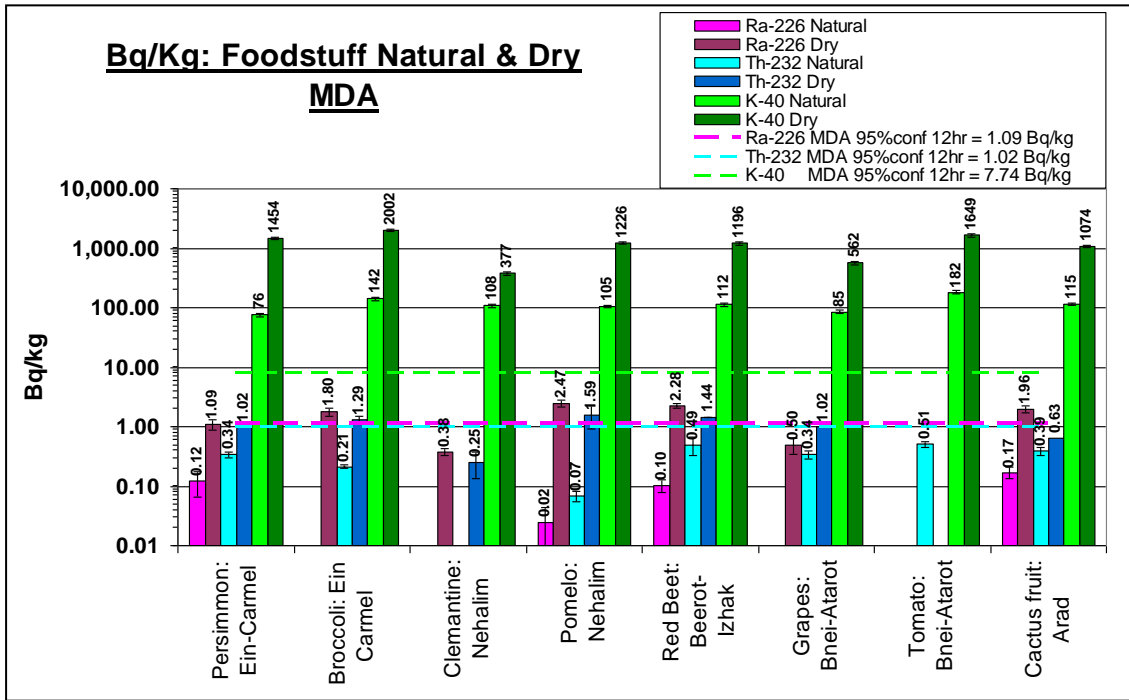


Figure 3: Specific activities of NORM radio-nuclides in natural and dried foodstuff samples.

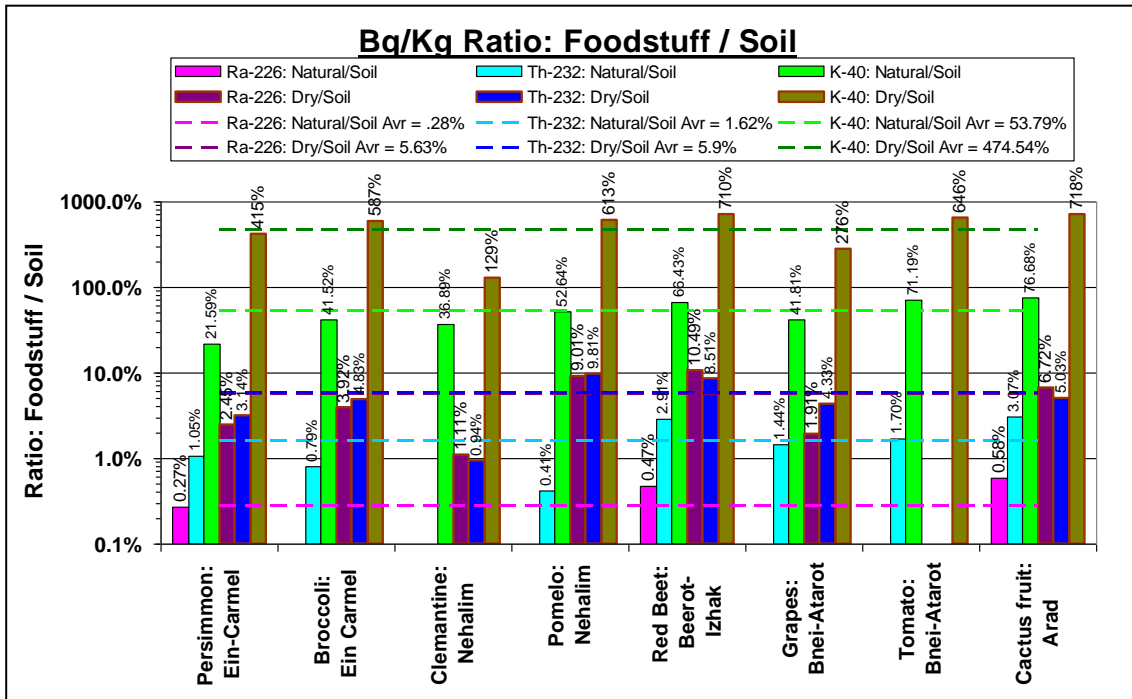


Figure 4: Transfer fraction of NORM radio-nuclides from soil to natural and dried foodstuff samples.

The transfer fraction of NORM radio-nuclides was calculated for the natural and dried foodstuff samples and is given in figure no 4. For ^{226}Ra in natural samples the average transfer fraction is 0.35% and for dried samples 5.09%. For ^{232}Th the average transfer fraction is 1.63% for natural samples and 5.23% for dried samples. For ^{40}K the results are very different compared to ^{226}Ra and from ^{232}Th . An average transfer fraction of 51.09% was obtained for the natural samples and 511.58% for dried samples. Although also the soil contains a much higher ^{40}K activity relative to ^{226}Ra and ^{232}Th (about one order of magnitude – see Fig 2), the ^{40}K activity in foodstuff is enhanced further to a factor of about 100 relative to ^{226}Ra and ^{232}Th . The reason for this seems to be that in the growing process fertilizers containing significant portions of potassium are added to the soil. Part of the potassium excess is absorbed by the plants (increasing its ^{40}K activity), but most of it is washed away from the soil by irrigation or rain and the ^{40}K content in the soil is reduced, leading to an excess in the ^{40}K ratio between plants and soil.

CONCLUSIONS

Gamma-ray spectrometry was used to determine the NORM radionuclide content in foodstuff samples and in cultivated soils in Israel during the year 2013. The transfer fractions from soil to foodstuff were determined as well, and excess values were found for ^{40}K , most probably due to added fertilizers which contain significant amounts of potassium. The activity measured in the checked foodstuff is very low and is in the general frame of values published in the literature [4,6,7].

REFERENCES

1. L.H.Staven, K.Rhoads, B.A. Napier and D.L. Strenge, "A Compendium of Transfer Factors for Agricultural and Animal Products". PNNL-13421, June 2003.
2. W.E. Kennedy, D.L. Strenge. "Residual Radioactive contamination from Decommissioning: Technical Basis for Translating Contamination Levels to Annual Total Effective Dose Equivalent". NUREG-5512 (PNL-7994), Pacific Northwest Laboratory, Richland, Washington. 1992.
3. Isotrak Nuclitec Eckert & Ziegler, Germany, 1 liter Marinelli beaker type 1N FZ-1262-001.
4. N.Lavi, G.Golob, Z.B. Alfassi. "Monitoring and surveillance of radio-caesium in cultivated soils and foodstuff samples in Israel 18 years after Chernobyl disaster". Radiation Measurements. 41, (2006) 78-83.
5. IAEA Technical Reports Series no. 295. "Measurement of Radionuclides in Food and the Environment" – a guidebook, IAEA library 0-000002-316-30, 1989.
6. T.V. Ramachadran, U.C. Mishra. "Measurement of Natural Radioactivity Levels in Indian Foodstuffs by Gamma Spectrometry". Appl. Radiat. Isot. 40, (1989) 723-726.
7. P.R. Maul, J.P. O'Hara. "Background Radioactivity in Environmental Materials". J. Environ. Radioactivity. 9, (1989) 265-280.

Using Cherenkov Counting For Fast Determination of $^{90}\text{Sr}/^{90}\text{Y}$ Activity in Milk

S. Tsroya¹, B. Dolgin¹, U. German¹, O. Pelled¹, Z. B. Alfassi²

¹ Nuclear Research Center Negev, P.O.B. 9001, 84190 Beer Sheva, Israel

² Ben-Gurion University of the Negev, 84105 Beer Sheva, Israel

1. INTRODUCTION

^{90}Sr is one of the main long-lived fission products, and it is transferred into human body primarily by food, with milk being a substantial contributor. Due to its biochemical similarity to calcium, most strontium is efficiently incorporated into bone tissues. ^{90}Sr is characterized by a long physical half life (28.8 y) and decays by beta particles with an E_{max} of 0.546 MeV to ^{90}Y . This daughter isotope has a half life of 64 h and decays into ^{90}Zr by beta particles with an E_{max} of 2.284 MeV.

The milk components produce a high turbidity and light attenuation, causing a significant decrease of the counting efficiency in liquid scintillation counting (LSC) systems, mostly used for beta emitters detection. Most methods proposed in the past are time-consuming, as they are based on several stages of chemical and physical treatments, including precipitation, ashing, ion exchange and extraction (Wikins et al., 1984, Porter et al, 1961, Kimura et al., 1979).

When measuring $^{90}\text{Sr}/^{90}\text{Y}$ activity by Cherenkov counting, most of the Cherenkov radiation is produced by ^{90}Y (about 98.6%), due to the much higher energy of its beta particles relative to these from ^{90}Sr . The counting efficiency varies strongly with color quenching, at a greater extent than in standard liquid scintillation counting (L'Annunziata, 2012), and therefore the quench correction is critical. The "external source area ratio" (ESAR) quench correction method was applied to measure $^{90}\text{Sr}/^{90}\text{Y}$ activities in aqueous samples with a wide range of quenching levels (Tsroya et al., 2009). This method was proved to be superior to all other quench correction methods (Tsroya et al., 2012) and is applicable also for determination of $^{90}\text{Sr}/^{90}\text{Y}$ in human urine (Tsroya et al., 2013). In the present work the applicability of the ESAR method to measurement of $^{90}\text{Sr}/^{90}\text{Y}$ activities in milk and some of its products was investigated.

2. MATERIALS AND METHODS

2.1 The ESAR method

A Quantulus 1220TM LSC system (manufactured by Wallac Oy, Finland) is operated at Soreq Nuclear Research Center, Israel. It has an external ^{152}Eu source, emitting radiation of sufficient energy to produce Cherenkov radiation. The ESAR method was developed for aqueous samples and is described in detail in a former publication (Tsroya et al., 2009). It is also described shortly in the latest edition of Handbook of radioactivity analysis (L'Annunziata, 2012).

The experiments in the present work were performed using a $^{90}\text{Sr}/^{90}\text{Y}$ calibrated and certified liquid standard with a specific activity of 4070 Bq/g of ^{90}Sr in 0.1 M HCl solution, provided by Amersham International. Polyethylene vials were used, as it is generally accepted that they are superior to glass vials for Cerenkov counting (Takiue (1996), L'Annunziata (2002)). The vials volume was 20 ml.

2.2 The milk samples

A set of representative milk samples was collected from the local supermarkets. The set contained 1% fat fresh and 1% UHT pasteurized skimmed cow milk (produced by Tnuva dairies), 3% fresh and UHT pasteurized cow milk, 3.7% fresh whole goat milk, about 6% raw sheep milk, 8% buffalo milk, and two cream types with different fat content: 15% (cooking cream) and 32% (whipping cream). A second set was also used, which contained 2% fat enriched milk, 3% fresh milk, 3.6% natural milk and 10% cooking. The fat contents mentioned above are as indicated on the packages.

3. RESULTS AND DISCUSSION

3.1 The parameters analysis

Due to the opaqueness of the milk bulk which is influenced by its complex composition and the variety of the milk matrix characteristics, it is expected that the counting efficiency will be influenced by the specific

properties of the various milk products (density, fat content, conductivity, etc.) in different ways. Six parameters were chosen for investigation in the present work: fat content, electrical conductivity, specific gravity, transmittance at 420nm, transmittance at 650 nm and the ESAR quench indicator parameter. The efficiency was the response function. The Minitab statistical software tool (Minitab 16) automatically performs a variance analysis for each factor and the interaction between them. For a quantitative analysis, a best subsets linear regression of the efficiency using different parameters sets (variants) was performed. The regression results obtained are presented in Table 1. The parameters (predictors) included in each specific model are marked in the property columns. The results for one parameter presenting a simple linear regression are given only for illustration, to stress their relative values.

Table 1. The best subsets regression results

Variants	R ² [%]	Stdev	Property (predictor)					
			Fat content	Specific gravity	Conductivity	Transmission 450nm	850nm	ESAR
1	46.1	2.81	√					
1	94.7	1.00						√
2	96.7	0.82		√				√
3	97.0	0.80	√	√				√
4	97.7	0.72	√			√	√	√
5	98.2	0.67	√		√	√	√	√
6	98.2	0.70	√	√	√	√	√	√

A best fitting line to the experimental points will be obtained when the correlation (R²) of the function (efficiency) expressed by the variables (predictors) in the model is as large as possible. "Stdev" is the standard deviation, representing the random experimental error in the efficiency values, and it should be as small as possible.

As seen in Table 1, for ESAR alone the R² is about 95%, more than twice the value for fat alone. Based on the experimental data and the defined statistical criteria, the best linear regression should include 5 variables, but we can see that adding more variants to the fit has only a minor influence on the R² compared to ESAR alone.

3.2 The contribution of ⁴⁰K

The ⁴⁰K contribution to Cherenkov counting can be estimated by assessing separately the activity of ⁴⁰K by HPGe (High Pure Germanium) gamma detector and converting the activity to counts using the efficiency calibration function.

The actual concentration of potassium in milk may depend on several factors, as the kind of milk giving animal and its diet. 8 samples from each of the milk types investigated in the present work were analyzed by γ spectrometry using an HPGe system with calibrated containers. The counting time was 100,000 s for each sample. The average activity concentration of ⁴⁰K for the different milk products is presented in Table 2.

Table 2: ⁴⁰K activities in different milk products

Milk type*	Activity[Bq/L]
1% - skimmed	54.0 ± 10.4
1% - skimmed UHT	38.6 ± 6.4
3%	50.9 ± 7.1
3% - UHT	57.5 ± 7.3
3.7% - goat milk	49.3 ± 7.4
6% - sheep raw milk	42.1 ± 5.9
8% - buffalo milk	29.8 ± 6.1
15% - cooking cream	60.4 ± 9.2
32% - whipping cream	≤MDA (18.1 Bq/L)

- Cow milk if not otherwise noted

The average activity in all types of milk products (except the 32% cream), is 47.8±10.3 Bq/l. The standard deviation within each group is up to about 20%. No significant variation of ⁴⁰K activity can be observed for all milk products examined within the given uncertainties. The efficiency of the ⁴⁰K Cherenkov counting was

estimated by measuring milk samples after adding a known amount of potassium. As each milk product has a different composition, the quenching effect will be type-dependent, therefore, the ^{40}K contribution will also be type-dependent. ^{40}K counting efficiency was obtained as a function of the relative ESAR index of the different milk products. The ^{40}K counting efficiency range is from 2.3% (for 32% fat cream) to 7.3% (for 1% skimmed milk).

4. $^{90}\text{Sr}/^{90}\text{Y}$ activity determination in milk samples

4.1 Application of the ESAR quench correction method

Samples were prepared by adding 16 Bq of $^{90}\text{Sr}/^{90}\text{Y}$ (as solution) to 20 ml from the different milk types. A linear function was fitted to the efficiency results obtained for all milk samples, and Fig. 5 presents the ESAR dependent efficiency curve. The full line in Fig. 5 relates to all natural milk samples, starting with 1% fat content up to 6% (raw sheep milk). The striped line includes the milk cream products, with 15% and 32% fat content. Standard $^{90}\text{Sr}/^{90}\text{Y}$ calibration solutions were added to 3% fat milk samples which were not used in the preparation of the calibration curve. These samples are shown in Fig.5 as open circles.

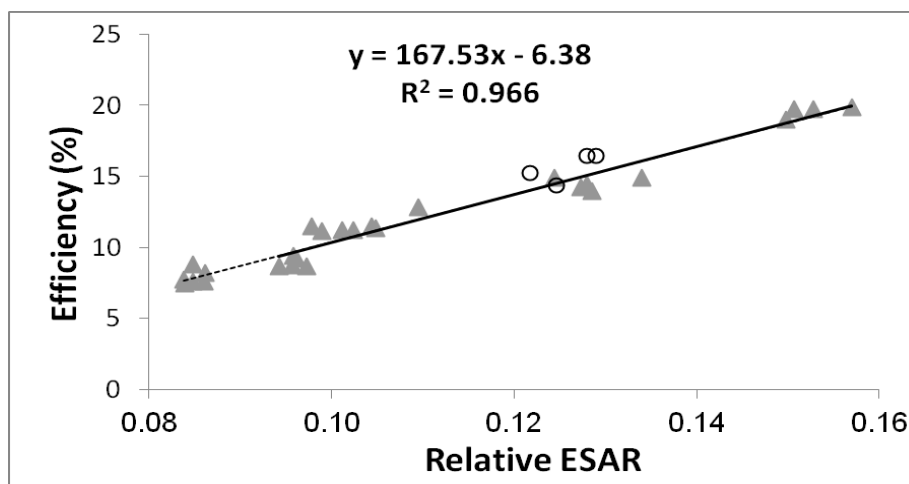


Figure 5. Correlation of the Cherenkov counting efficiency of $^{90}\text{Sr}/^{90}\text{Y}$ to the ESAR quenching indicator parameter in milk samples.

By using the quenching efficiency curve given in Fig 5, the $^{90}\text{Sr}/^{90}\text{Y}$ activity in any milk sample and milk products can be determined, without considering its source or fat content. The evaluated activities and the difference from the known activity added to "unknown" samples are presented in Table 3.

Table 3: ^{90}Sr activity determination in four different kinds of milk products (3 natural drinking milk sorts and a 10% fat cooking cream).

<u>Fat [%]</u>	<u>Actual activity [Bq]</u>	<u>Evaluated activity [Bq]</u>	<u>Difference [%]</u>
2	8.29 ± 0.18	8.41 ± 0.30	1.45
2	8.29 ± 0.18	8.07 ± 0.29	-2.65
2	16.59 ± 0.36	18.02 ± 0.64	8.62
2	16.59 ± 0.36	17.47 ± 0.62	5.30
3	8.29 ± 0.18	8.53 ± 0.64	2.90
3	8.29 ± 0.18	8.79 ± 0.66	6.03
3	16.59 ± 0.36	16.32 ± 1.22	-1.63
3	16.59 ± 0.36	17.91 ± 1.34	7.96
3.6	8.29 ± 0.18	8.64 ± 1.41	4.22
3.6	8.29 ± 0.18	8.70 ± 1.42	4.95
3.6	16.59 ± 0.36	15.67 ± 2.56	-5.55
3.6	16.59 ± 0.36	17.23 ± 2.81	3.86
10	8.29 ± 0.18	10.02 ± 2.80	20.87
10	8.29 ± 0.18	10.27 ± 2.87	23.88
10	16.59 ± 0.36	21.15 ± 5.90	27.49
10	16.59 ± 0.36	20.51 ± 5.72	23.63

For the natural milk samples (2%, 3% and 3.6% fat), the mean difference between the actual and real activity is about 4% and the results for all samples are within 8.6% from the target values. For the 10% cooking cream there is an average difference of about 24% from the target values. Although this difference is within the uncertainty range of the evaluated values, there seems to be a bias (as all differences are in the same direction).

4.2 The limit of detection

Due to its simplicity and short processing time, the Cherenkov counting method is especially suitable for emergency situations. However, if assessing ^{90}Sr activity in milk and its products without applying any pre-concentration procedure, a relatively high MDA (minimum detectable activity) is expected. The applicability of the proposed method was checked against the corresponding regulations for emergency situations. The results are presented in Fig. 6 for 4 hours counting time.

The highest MDA for drinking milk is for the buffalo milk (containing the maximum fat percent in natural drinking milk - 8%), which is about 108 Bq/l, lower than both limits of the FDA (160 Bq/kg) and the European regulations (125 Bq/l - EU No 961/2011, FDA 1998). For the most popular and widespread drinking milk products (1%-3% fat content) the MDA for ^{90}Sr when applying direct Cherenkov counting for 4 h is much below 100 Bq/l. For the processed milk products (creams) with the highest fat content of 32% the MDA values approach the limiting levels, but due to their related high uncertainties applying the ESAR index in this case seems not to be applicable.

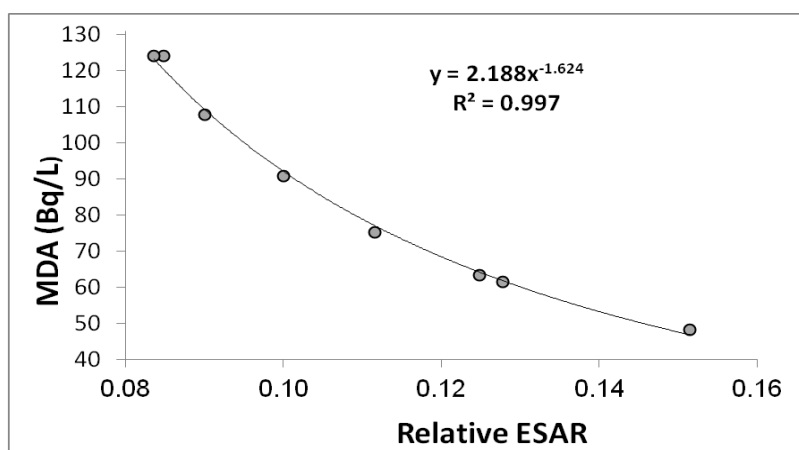


Figure 6. The ^{90}Sr MDA levels for 4 h counting time in milk products for various ESAR values.

5. CONCLUSIONS

Cherenkov counting is a fast, reliable and non-destructive method for detecting high energy beta emitters in aqueous solution, but it is sensitive to quench correction, especially for colored or semi-opaque media as milk. The ESAR quench correction index is shown to work well also for milk, in spite of the high turbidity and strong light attenuation. The ESAR index is the main parameter which uniquely defines the counting efficiency for all kinds of milk tested. There are no major differences in the ^{40}K content in different sorts of drinking milk, enabling a direct evaluation of the $^{90}\text{Sr}/^{90}\text{Y}$ based only on the ESAR value.

REFERENCES

- EU No 961/2011. Special conditions governing the import of feed and food originating in or consigned from Japan following the accident at the Fukushima nuclear power station and repealing Regulation (EU) No 297/2011. EU commission implementing regulation of 27.11.2011. L 252/10.
- FDA 1998. Food and Drug Administration. Accidental Radioactive Contamination of Human Food and Animal Feeds: Recommendations for State and Local Agencies. Federal Register 63:43402-43403; 1998.
- Kimura, T., Iwashima, K., Ishimori., T., Hamada, T., 1979, Separation of Strontium-89 and -90 from Calcium in Milk with a Macrocyclic Ether. *Anal. Chem.* 51, 1113-1116.
- L'Annunziata, M.F., Passo, C.J., 2002. Cherenkov counting of yttrium-90 in the dry state; correlations with phosphorus-32 Cherenkov counting data. *Appl. Radiat. Isot.* 56, 907-916.
- L'Annunziata, M.F., 2012. Cherenkov Counting. pp. 935-1019, in "Handbook of radioactivity analysis", Third ed. (M.F. L' Annunziata, Ed.) Elsevier, Oxford.
- Minitab 16, <http://www.minitab.com/en-US/products/minitab/default.aspx>

- Porter, C., Cahill, D., Sshneider, R., Robbins, P., Perry, W., Kahn, B., 1961. Determination of Strontium-90 in Milk by an Ion Exchange Method. *Anal. Chem.* 33, 1306-1308.
- Takiue, M., Natake, T., Fujii, H., Aburai, T., 1996. Accuracy of Cerenkov Measurements Using a Liquid Scintillation Spectrometer. *Appl. Radiat. Isot.* 47, 123-126.
- Tsroya S., Pelled, O., German, U., Marco, R., Katorza, E., Alfassi, Z.B., 2009. Color quench correction for low level Cherenkov counting. *Appl. Radiat. Isot.* 67, 805-808.
- Tsroya S., Pelled, O., German, U., Katorza, E., Abraham A., Alfassi, Z.B., 2012. A comparative study of color quenching correction methods for Cherenkov counting. *Appl. Radiat. Isot.* 70, 397-403.
- Tsroya S., German, U., Pelled, O., Katorza, E., Alfassi, Z.B., 2013. Determination of $^{90}\text{Sr}/^{90}\text{Y}$ activity in urine samples using Cherenkov counting. *Appl. Radiat. Isot.* 73, 12-16
- Wilkins, B.T., Green, N., Dodd, N.J., Smith, D.M., 1984. Concentrations of Strontium-90 and Cesium-137 in milk produced in the Channel Islands. *Rad. Prot. Dosim.* 8, 253-255.

Posters (Wednesday, February 12, 2014 15:30)

Study of Cleanup Procedures for Contaminated Areas: Examination of Rubidium as a Surrogate to Cesium

O. Paz Tal, R. Bar Ziv, R. Hakmon, E. J. C. Borojovich, A. Nikoloski, T. Ohaion, R. (Yanosh) Levi, I. Yaar

Nuclear Research Center Negev, POB 9001 Beer Sheva 84190, Israel

A radiological weapon, or radiological dispersion device (RDD), is designed to spread radioactive materials (^{137}Cs , ^{60}Co , ^{241}Am , ^{252}Cf , ^{192}Ir , ^{238}Pu , ^{90}Sr , ^{226}Ra , etc) over a large area, in order to cause severe contamination. The dispersed radioactive material can be strongly bound to surfaces if not effectively removed shortly after the event.

An effective decontamination agent for such cases is the commercial polymer Decongel-1101¹. It can be applied onto contaminated surfaces by brushing or spraying. Upon drying, it forms stable films that can be peeled off the surface, together with most of the contaminating materials.

One of the most dangerous isotopes that can be used by terrorist to make a RDD is ^{137}Cs ². Therefore, it is important to examine the effectiveness of the polymer Decongel-1101 in removing it. Due to the difficulty in working with ^{137}Cs in large scale experiments, It was suggested to replace it with the short lived radioisotope ^{86}Rb (~18.6 days). This isotope is a good simulator for ^{137}Cs , having similar chemical properties and migration behavior.

This work is aimed at verifying whether ^{86}Rb can indeed serve as a simulator to ^{137}Cs in cleanup procedures of large contaminated areas. The first step will be a small scale comparison, on porous and non-porous surfaces, of the decontamination efficiency of this procedure tested on Rb versus Cs. These elements were spread on the examined surfaces as known concentration solutions of natural Rb and Cs salts. The decontamination efficiency was measured by peeling off the dry polymer and measuring the concentrations of the two elements in the polymer by various analytical methods.

¹<http://decongel.com/documents/1101%20Product%20Data%20Sheet%20v080612.pdf> (Last accessed on 18.1.14).

²J.L.Conca, J.R. Wischnewsky and M.D. Johnson, Reducing the Threat of a Serious ^{137}Cs Dirty Bomb, Proceedings of the DHS Conference; Working Together – Research & Development Partnerships in Homeland Security, the Seaport Hotel and World Trade Center, Boston, MA, April 27-28 (2005).

A Computerized QC Analysis of TLD Glow Curves for Personal Dosimetry Measurements Using TagQC Program

S. Primo⁽¹⁾, H. Datz⁽¹⁾ and A. Dar⁽²⁾

⁽¹⁾ *Soreq Nuclear Research Center, Yavne, Israel*

⁽²⁾ *Empiric Technologies consulting (e.t.c) Ltd. Modiin, Israel*

INTRODUCTION

The External Dosimetry Lab (EDL) at the Radiation Safety Division at Soreq Nuclear Research Center (SNRC) is ISO 17025 certified and provides its services to approximately 13,000 users throughout the country from various sectors such as medical, industrial and academic. About 95% of the users are monitored monthly for X-rays, γ and β radiation using Thermoluminescence Dosimeter (TLD) cards that contain three LiF:Mg,Ti elements and the other users, who work also with thermal neutrons, use TLD cards that contain four LiF:Mg,Ti elements. All TLD cards are measured with the Thermo 8800pc reader.⁽¹⁾

Suspicious TLD glow curve (GC) can cause wrong dose estimation so the EDL makes great efforts to ensure that each GC undergoes a careful QC procedure.⁽³⁾ The current QC procedure is performed manually and through a few steps using different softwares and databases in a long and complicated procedure: EDL staff needs to export all the results/GCs to be checked to an Excel file, followed by finding the suspicious GCs, which is done in a different program (WinREMS), According to the GC shapes (Figure 1 illustrates suitable and suspicious GC shapes) and the ratio between the elements result values (see graph in Figure 2), the inspecting technician corrects the data.⁽³⁾

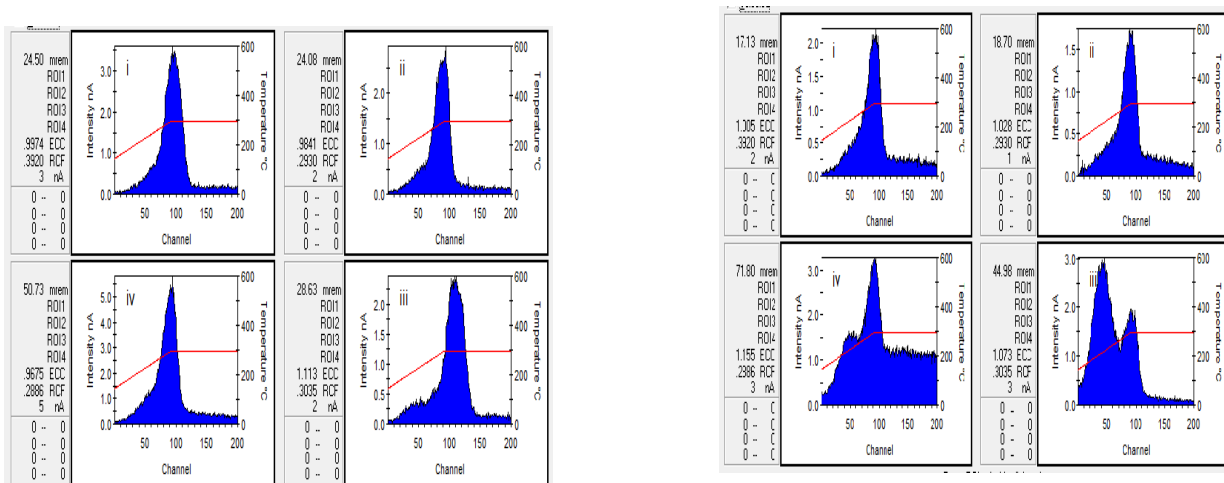


Figure 1. Typical LiF: Mg, Ti glow curve following ^{137}Cs irradiation (a) suitable GC; (b) suspicious GC

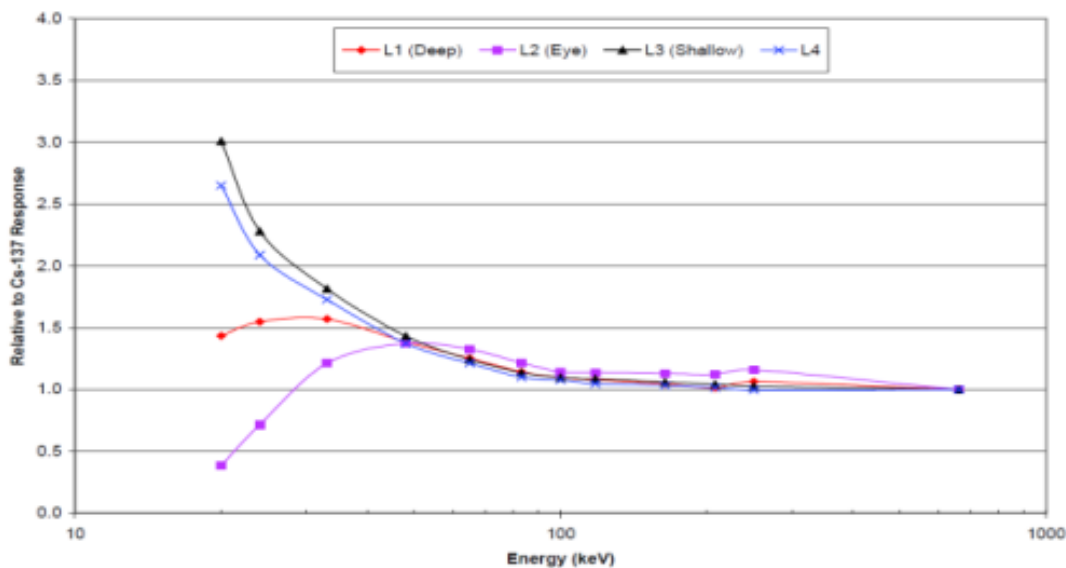


Figure 2. LiF:Mg,Ti TLD elements response⁽²⁾

The motivation for developing the new program is the complicated and time consuming process of our the manual procedure to the large amount of TLDs each month (13,000), similarly to other Dosimetry services that use computerized QC GC analysis.^(4,5) it is important to note that only ~25% of the results are above the EDL recorded level (0.10 mSv) and need to be inspected. Thus, the purpose of this paper is to describe a new program, TagQC, which allows a computerized QC GC analysis that identifies automatically, swiftly, and accurately suspicious TLD GC.

TagQC program description.

The source file is copied (to avoid damage of the raw data) to a destination file and all the corrections are made and saved on it.

A morphologic classifier is embedded in TagQC, for pointing out "*Suspicious*" GC using the following general method:

- a. A canonic GC is defined (to which the analyzed GC is compared. during the classifier).
- b. Each GC is first canonized & passes a noise filter. a too high noise figure in a GC renders it as "*Suspicious*".
- c. The location and shape of the main lobe of the GC is checked, in several parameters: the start (first channel) of the lobe, the end of the lobe (last channel) - both using the wavefront, The slopes of the front and end of the lobe, the width of the lobe, its similarity to a parabola (difference from quadratic fit), and the shift of the peak from its canonic location. Finally the skewness and kurtosis of the GC is compared to the canonic ones. Any diversion from the canonic parameters that are too large renders the analyzed GC *suspicious*.
- d. The last step is comparison between the values of the parameters of the various elements on the tag (if possible), and pointing out outliers as "*suspicious*".

Once the above process is complete, the program automatically indicates the faulty GC by painting the suspicious element with a different color (red), as shown in Figure 3.

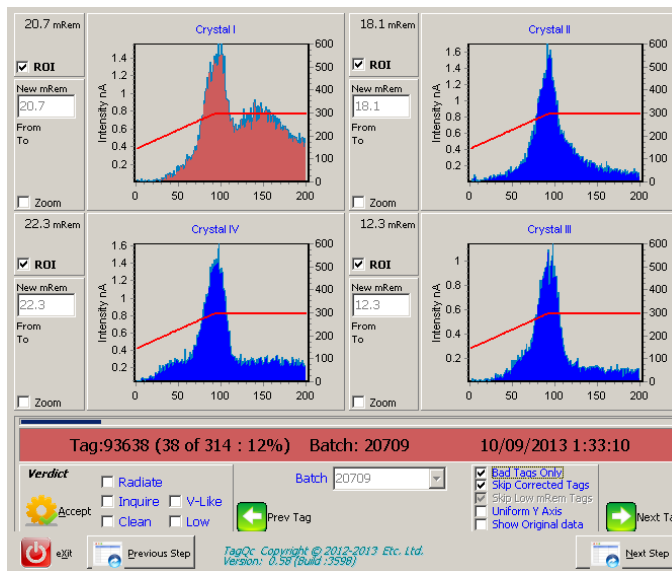


Figure 3. TagQC screen with marked suspicious GC (upper left GC)

The operator can choose from a number of options to correct the abnormal data:

1. Use ROI (region of interest) by dragging the GC's borders to fit the correct GC and dose value (as shown at the bottom of Figure 4).
2. Select "Low" check box to correct all the doses to a value which is set at the preferences page, as a limit of detection (as shown at the bottom of Figure 3).
3. Selecting a specific check box, when only the third TLD element is suspicious, to determine the value of the third element to the average dose of the first and second elements. Shown in Figure 5.

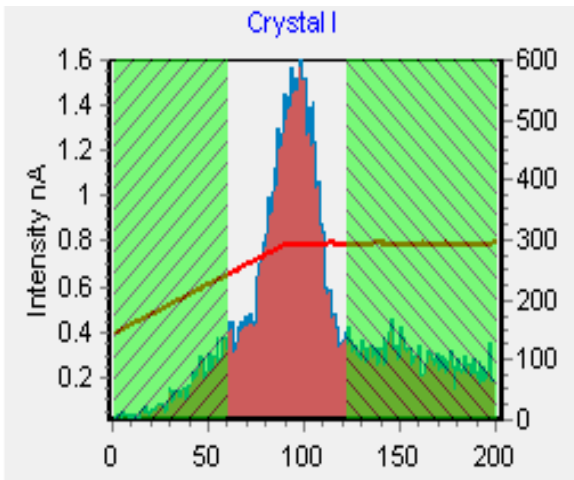


Figure 4. TagQC ROI correction

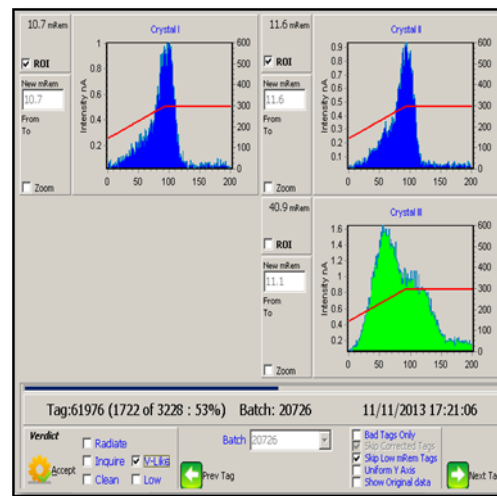


Figure 5. 3rd element value correction

In addition to abnormal data correction, the operator can perform more QC steps:

1. Selecting the "Irradiate" checkbox, the TLD will be manually exposed to a known dose and re-measured prior to the shipment to the user.
2. Selecting the "Inquire" checkbox will e-mail a print screen of the GC to the EDL supervisor for a second opinion and approval.

When all the TLD cards are checked, a log report is issued containing all the information of any card that underwent results intervention.

CONCLUSION

TagQC is a useful program that automatically will indicate suspicious TLD elements results and allows correcting the data in a reliable and fast way. In addition, it will allow the EDL staff to view and to check only the suspicious TLD results, which will make the QC procedure much faster and accurate.

The TagQC program is currently being examined at the EDL. At the completion of the examination and validation, TagQC will be used in routine activities and thus will improve the efficiency and quality assurance of EDL service.

REFERENCES

1. Model 8800 Automatic TLD Card Reader with WinREMS Operator's Manual. Publication No 8800-W-O-1200-006.
2. WinAlgorithms: Dose calculation Algorithm for 8805, 8810, 8814, and 8815 Dosimeters user's manual. Publication No. ALGM-W05-U-0903-001
3. LiF:Ti, Mg Methodology - Guidelines for GC Analysis. Publication No. LiFM-G-C-1091-001-Bicron/Saint-Gobain/Norton Industrial Ceramics Corporation.
4. Harvey.A.John, Rodriguse L.Miesher, J.Kearfott.J. *Computrized glow curve analysis (GCA) method for WinREMS thermoluminescent dosimeter data using MATLAB*. Applied Radiation and Isotopes **69**, 1282-1286, (2011).
5. Chase, W.J, Bezaire, M.D, Vanderzwet, F.P., Taylor, C.E., *A glow curve analyzer (GCA) for routine analysis of personnel thermoluminescent dosimeter results*. Radiation Measurement **43**, 621-625, (2008).

Electronic and Magnetic Properties of NpNi₅

A. Hen,^{1,2} E. Colineau,¹ R. Eloirdi,¹ J.-C. Griveau,¹ J.-P. Sanchez,⁴
A. B. Shick,^{1,5} I. Halevy,^{2,3} I. Orion,² and R. Caciuffo¹

¹European Commission, Joint Research Centre, Institute for Transuranium Elements, Postfach 2340, D-76125 Karlsruhe, Germany

²Ben Gurion University, IL84105 Beer-Sheva, Israel

³Nuclear Research Center Negev, P.O. Box 9001, IL84190 Beer-Sheva, Israel

⁴SPSMS, UMR-E CEA/UJF-Grenoble 1, INAC, FR-38054 Grenoble, France

⁵Academy of Sciences of the Czech Republic, Na Slovance 2, CZ-182 21 Prague, Czech Republic

The physical properties of binary actinides and transition metal alloys are of great importance for the safety assessment of nuclear fuels. Since transition metals are major components of the cladding material of fuel rods (stainless steel, HT-9 etc.), the physical properties of those compounds formed by accidental fuel-cladding interactions could have limiting factors on the fabrication, life time operation and disposal of nuclear fuels. Binary compound of the form ReT₅ (Re = rare earth, T = Transition metal) has been in the focus of interest mainly because of their magnetic properties (small Re to T stoichiometric ratio, large spontaneous magnetization and high Curie temperature) and their ability to store large amount of hydrogen per formula unit (f. u.)

Reported in 1997 [1], NpNi₅ was synthesized and identified to have hexagonal (D_{2d}) CaCu₅ crystallographic structure, with room-temperature lattice parameters $a = 8.3107(1)$ Å and $c = 8.1058(1)$ Å. In the present study, NpNi₅ has been synthesized and characterized by means of powder x-Ray diffraction (**Fig. 2** left panel), Superconducting – Quantum – Interference – Device magnetometry (SQUID, **Fig. 2** right panel), ²³⁷Np Mössbauer spectroscopy [2] (**Fig. 3** left panel) and specific heat measurements (**Fig. 3** right panel).

Magnetization curves indicate that NpNi₅ is a ferromagnet ($T_C \sim 16$ K), fit of the paramagnetic part to the Curie–Weiss law ($C \sim 1.7$ emu·K/mol, $\theta_P \sim 14.6$ K) gives an effective moment $\mu_{\text{eff}} \sim 3.7 \mu_B$ per f.u. – no magnetization hysteresis was observed. The isomer shift ($\delta_{\text{IS}} \approx -11.1$ mm/s vs. NpAl₂) observed in Mössbauer spectra suggests a tetravalent Np state, but considering the influence of conduction electrons we determine a Np³⁺ (5f⁴ configuration) oxidation state. The hyperfine field determined by fitting of the spectra (~ 439 T) gives an ordered moment at the Np site $\mu_{\text{Np}} \sim 2 \mu_B$ per Np ion ($1 \mu_B = 215$ T [3]). The magnetic transition is clearly visible in the temperature dependence of the specific heat, and a magnetic phase diagram as a function of temperature and external magnetic field was generated.

In this communication we will present the results obtained and discuss them in the light of theoretical considerations.

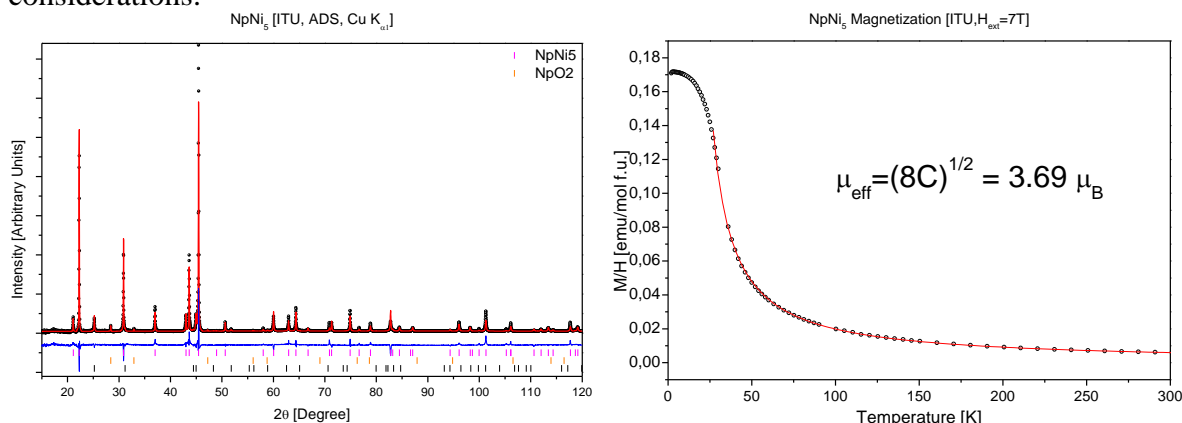


Fig. 2 Left: Powder x-ray diffraction pattern of NpNi₅, black dot – measured data, red line – fitted profile, blue line – difference profile, vertical tick – angular position of Bragg peaks. **Right:** Temperature dependence of the magnetic susceptibility, red line – fit to the Curie-Weiss law.

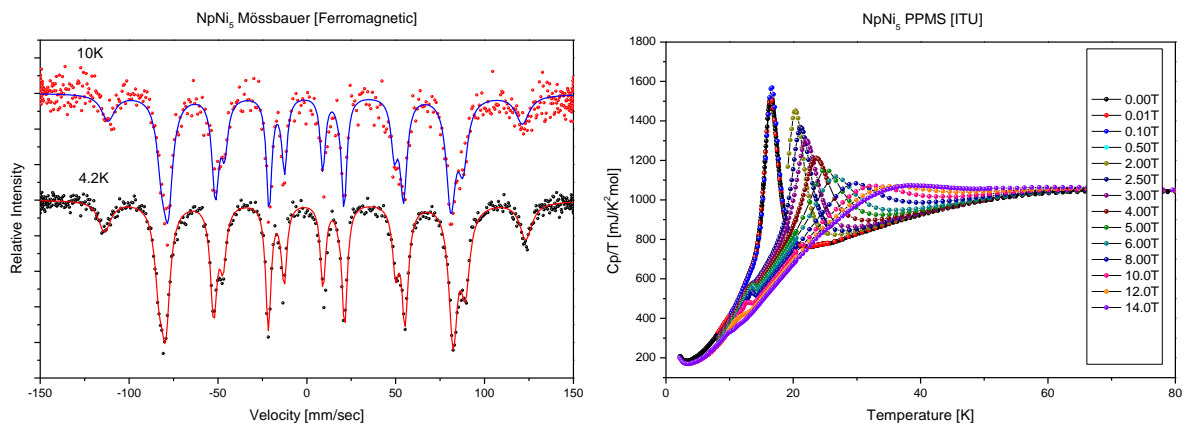


Fig. 3 **Left:** Mössbauer spectra taken in the ferromagnetic region, dots – measured data, lines – fits of hyperfine fields to the measured data, spectrum is composed of one hyperfine field as expected from the crystallography.

Right: Normalized heat capacity as a function of temperature in various external magnetic fields.

ACKNOWLEDGEMENTS

The high purity Np metals required for the fabrication of the compound were made available through a loan agreement between Lawrence Livermore National Laboratory and ITU, in the frame of a collaboration involving LLNL, Los Alamos National Laboratory and the US Department of Energy.

REFERENCES

- [1] M. Akabori et al. , Journal of Alloys and Compounds 257 (1997) 268-272.
- [2] R.L. Mössbauer., Zeitschrift für Physik, Bd. **151**, S. 124-143 (1958).
- [3] B. D. Dunlap and G. M. Kalvius, in Handbook on the Physics and Chemistry of the Actinides, edited by A. J. Freeman and G. H. Lander (North-Holland, Amsterdam, 1985), Vol. 2, p. 329.

Posters (Wednesday, February 12, 2014 15:30)

Radioactive Contamination Estimation from Micro-Copters or Helicopter Airborne Survey: Simulation and Real Measurements

I. Halevy, M. Ghelman, Y. Yehuda-Zada, A. Manor, A. Sharon and I. Yaar

Nuclear Research Center – Negev, P. O. Box 9001, Be'er-Sheva 84190, Israel

One of the main advantages of acquiring aero-radiometric measurements lies in the high collection rate of data over large areas and rough terrain. Typical aero-radiometric system records and saves gamma ray spectrum, correlated with the GPS derived location information in regular time intervals of one to two seconds. Such data can be used to locate radiation anomalies on the ground, map ground contamination or track a radioactive airborne plume. Acquiring spectral data of this type allows separation of natural radioactivity from that of man-made sources and identification of specific isotopes, natural or man-made.

The data acquisition can be done by helicopter or micro-copters at wide range of heights from few meters to few kilometers.

Usually the flight altitude will be kept constant to make the data analysis easier. Rough terrain will jeopardize that assumption. The radioactive particles are not always on the ground, they can be in a cloud above the ground or on roofs or trees. Speed of survey with a helicopter is in the range from hovering to ~120 Knots, while the speed of micro-copters is much lower, from hovering to ~30 Knots. Both, the helicopter and the micro-copters are suffering from limited abilities while severe weather conditions.

The main advantages of micro-copters are the ability to fly even indoor and without exposing the measuring team to radiation or extra flight risks.

When the survey is done or even during the survey, the main challenge is to estimate the radiation field and the contamination in the scene.

An iterative algorithm was suggested to estimate the radioactive contamination for analyzing an airborne survey [1].

In that work this algorithm will be tested on real scenario while spreading radioactive material, ^{99m}Tc , simulating an RDD events by explosion [2, 3].

In those simulations it is clear that a lower-height survey can improve the space resolution. Slow flight will improve the detection sensitivity but will take much more time.

This survey can be for detection only or it can bring also isotope identification by energy resolution. In our software, four energies windows can be set as our PDS-1000 flying detector.

We simulated a spread of radioactive sources on a radioactive background. A radioactive field at a survey height was calculated. From that data we found the spread of radioactive sources by our iterative algorithm.

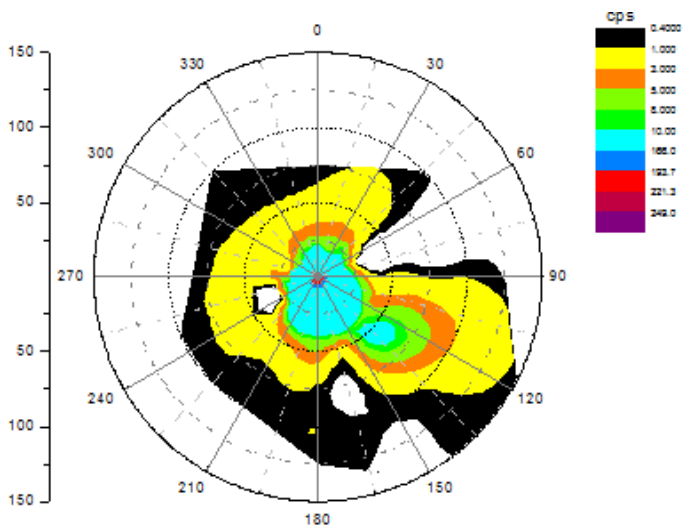
There is no clear proof that the results are unique. The highest background we have the less significant map of spread radioactive sources can be achieved.

Few new results of simulation and real surveys are depicted in the next figures.

Mikro-Kopter / multi-rotor



Figure 1: Mikro-Kopter / multi-rotor (upper)
Airborne radiation survey of ^{99m}Tc from “Green field” (Open field) test compared with ground survey (lower) [2].



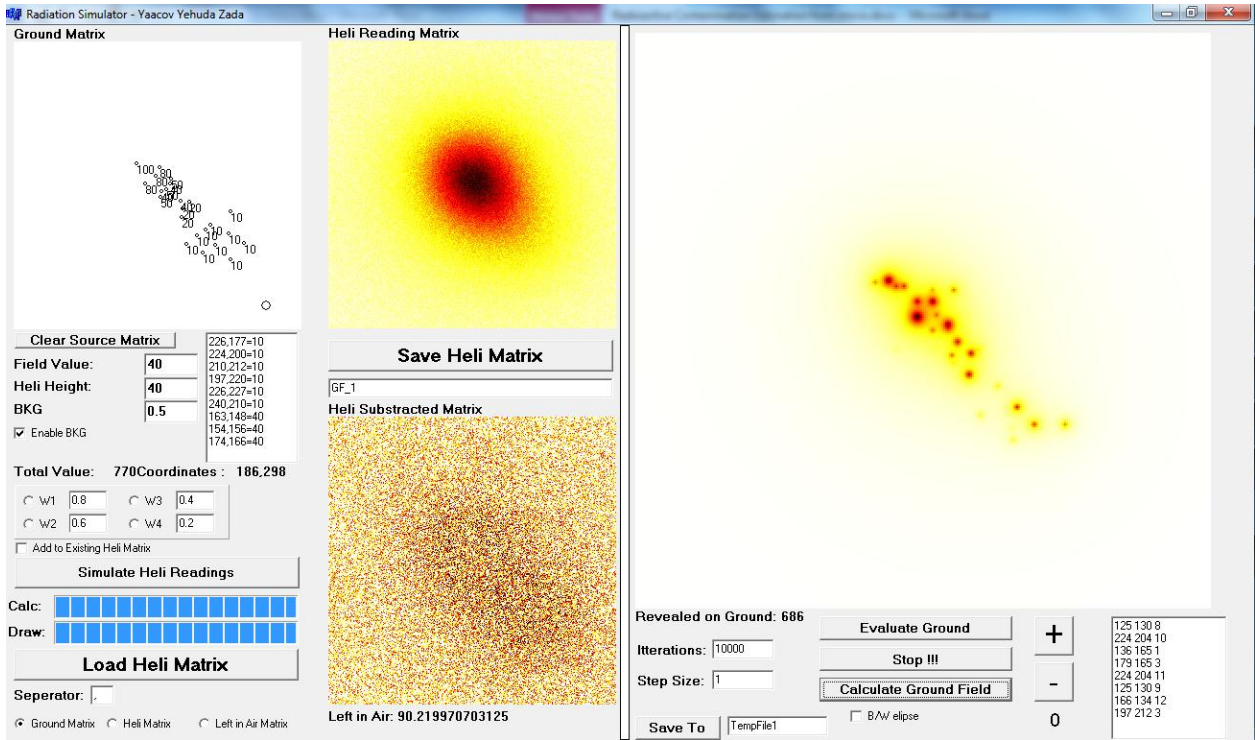


Figure 2: Airborne radiation survey analysis of ^{99m}Tc from “Green field” (Open field) test compared with ground survey [2].

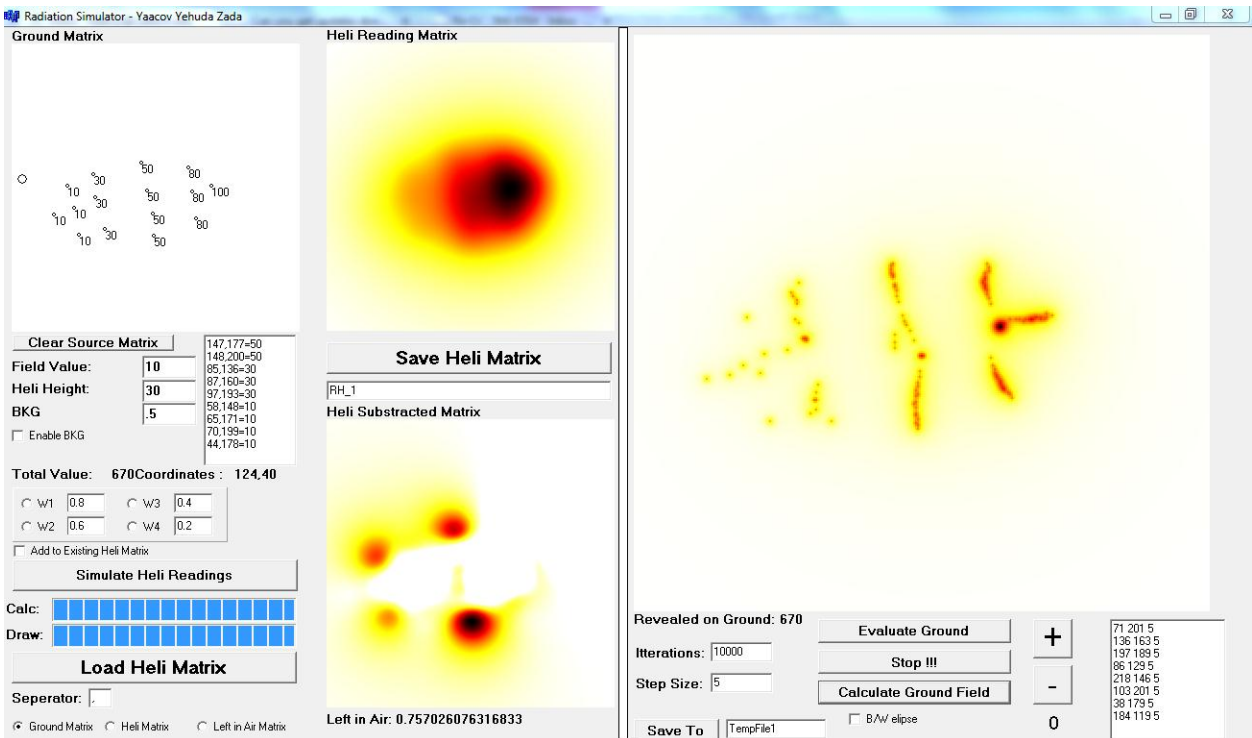
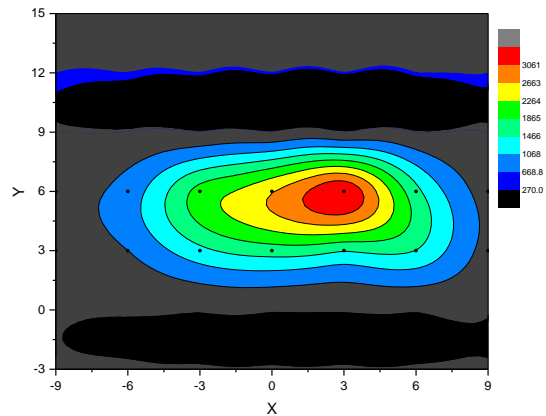


Figure 3: Airborne radiation survey of ^{99m}Tc from “Red-House” (Indoor) test compared with ground survey [3].

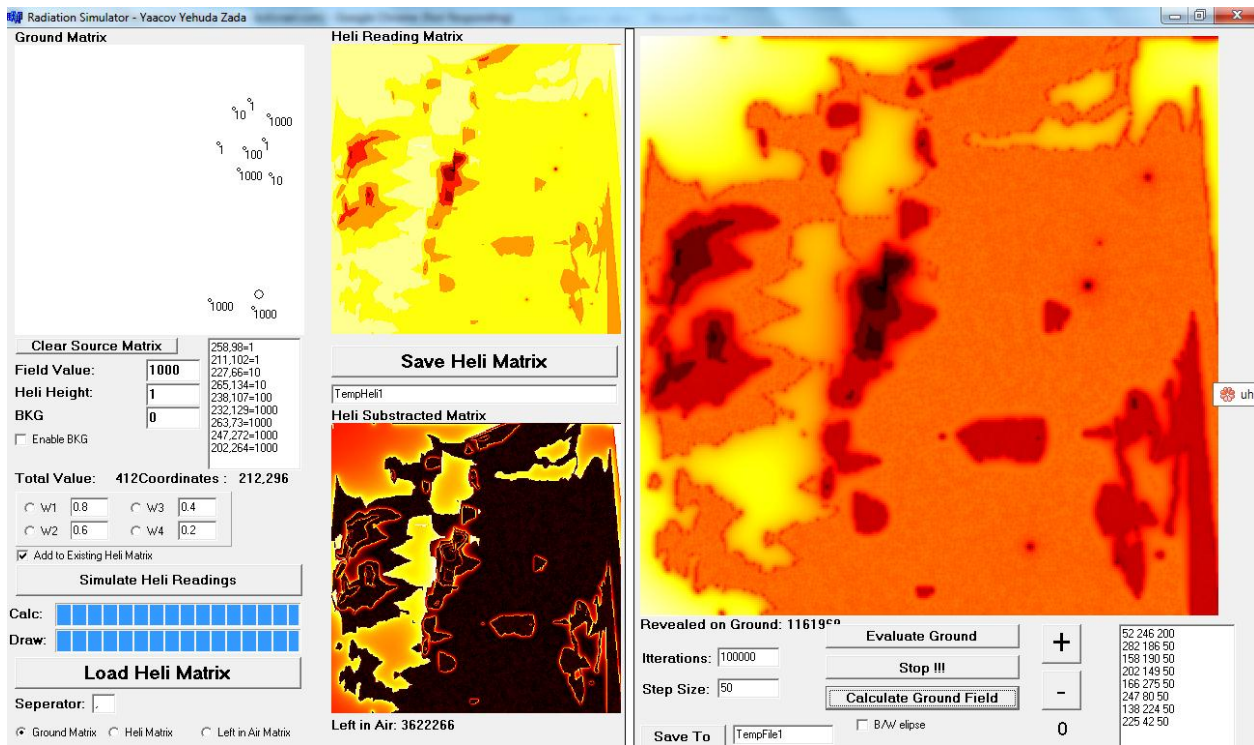


Figure 4: Airborne radiation survey of natural background from Air RAM 2000 measurements at the Government Wash area [4].

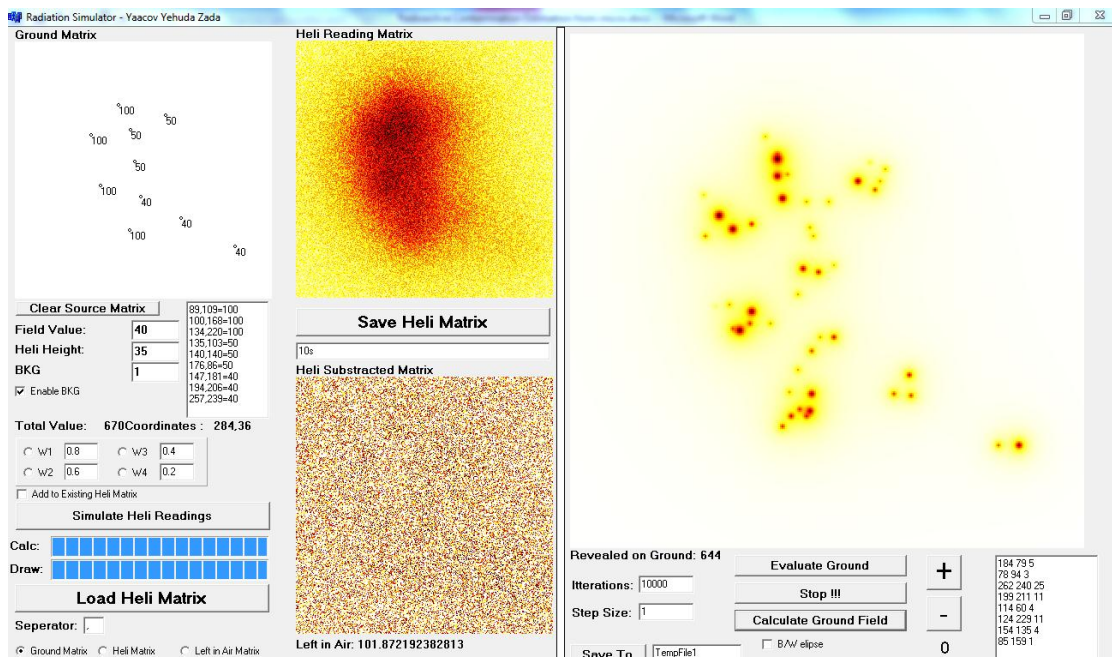


Figure 5: Airborne radiation simulation of natural background with ten spread sealed sources.

REFERENCES

- [1] M. Ghelman, M. Sheinfeld, A. Manor, E. Vax, Y. Kadmon and D. Tirosch The 25th Conference of the Nuclear Societies in Israel 16-18 February 2010, Crown Plaza Hotel, Dead Sea, Ein Bokek, ISRAEL (PDF)
- [2] A. Sharon, D. Sattinger, I. Halevy, R. Neuman, A. Ashkenazi and I. Yaar Cloud Rise Model for a "Dirty Bomb" Event The 25th Conference of the Nuclear Societies in Israel 16-18 February 2010, Crown Plaza Hotel, Dead Sea, Ein Bokek, ISRAEL (PDF)

- [3] Cloud Rise Model for an Explosion Inside a Building A. Sharon, D. Sattinger, I. Halevy, R. Neuman, A. Ashkenazi and I. Yaar The ²⁵th Conference of the Nuclear Societies in Israel 16-18 February 2010, Crown Plaza Hotel, Dead Sea, Ein Bokek, ISRAEL (PDF)
- [4] Aerial Measuring System (AMS) / Israel Atomic Energy Commission (IAEC) Joint Comparison Study Report Piotr Wasiolek and Itzhak Halevy: DOE/NV/25946-1941

Prospects for the SMR Technology

B. Tavron , D. R. Marouani

Israel Electric Corporation, Haifa, Israel

ABSTRACT

The nuclear power industry which suffered from prolonged recession has got additional slowdown by the Fukushima nuclear accident. Nuclear safety and security concerns together with cheap fossil fuel alternatives are among main reasons for this recession. Small Modular Reactor (SMR) technologies which feature enhanced safety, security and economics features may restore confidence in nuclear power and lead the nuclear energy renaissance. SMR unit sizes (up to 300MWe), match common existing oil, coal and gas unit sizes and present the environmentally suitable candidate for replacing old polluting plants. Moreover, SMR unit sizes and their enhanced load following capabilities match well future electricity system requirements.

SMR technology, safety and security features

SMR is referred by IAEA as Small-Medium size Reactor, and is defined to have power in the range of up to 700MWe. Here we will refer to the other commonly used term for SMR - Small Modular Reactors, referring to the factory made module feature of SMR of up to 300MWe. In the IAEA advanced reactor database - <https://aris.iaea.org/> - there are about 30 SMR types, based mainly on Light Water Reactor (LWR), Heavy Water Reactor (HWR), Gas Cooled Reactor (GCR) and Liquid-Metal Cooled Reactor (LMCR) technologies. Most of SMR designs are at various stages of development. SMR of 3 technologies are under-construction: the HTR-PM (200MWe) Pebble-Bed reactor in China, the KLT-40S floating nuclear power (35MWe PWR) in Russia and the CAREM 27 MWe Integral Pressurized Water Reactor in Argentina. Research is being carried out on SMR design for electricity generation, process heat production, desalination, hydrogen generation and other applications

SMR are expected to have improved safety performance mainly due to its reduced source term. The reduced power level means also lower decay heat allowing for simplified and/or passive emergency heat removal systems. Many SMR variants feature integral design which has less vulnerable components therefore reducing accident probabilities. The small reactor size makes also their seismic design simpler and more robust. The improved safety performance results in increased safety margins reduced shielding, reduced site exclusion and emergency planning zones.

Security measures for small reactors may be easier to implement. Some SMR types feature underground reactor design which improves resistance to external hazards. SMR may also include proliferation-resistant fuel cycle design [1].

SMR economics

Large reactors benefit from the economy of scales due to saving expenses which are independent from reactor size. Siting multiple SMR units at the same site, with the common infrastructure may also improve SMR economics. SMR also benefit in cost savings from factory module fabrication. Increasing SMR fabrication efficiency is anticipated at conditions of "mass production". Shorter construction times of SMR, will significantly save the interest payments. SMR will have additional cost savings from incrementally adjusting installed site capacity to demand growth and financial conditions. The SMR initial investment level is significantly lower than for large reactors reducing the finance risk and therefore enabling the private sector involvement. Since SMR are still in development stages, no detailed cost estimates are available; some general evaluations have estimated that SMR can be competitive especially when applying "carbon tax" on fossil fuel generation plants [2].

SMR and future electricity systems

Discoveries of large shale gas resources (especially in the US), environmental considerations and the energy sector reforms are some of main factors contributing to the change of electricity systems during the last decade. In the US the CCGT (Combined Cycle Gas Turbine) technology become the leading generation expansion technology on the account of coal, and oil fueled plants. Greenhouse gases emitting technologies are being phased-out by renewable energy technologies, like wind and solar, due to environmental concerns. Introduction of intermittent renewable energy sources, like solar and wind (both with up to 30% capacity factor), requires flexible backup generation capacity with steep load-following capabilities. In addition, government policies for renewable energy such as subsidies and dispatch priorities have to be set in order to make them acceptable. Hence, the operation of future grids will be a more complex task, and various "Smart grid" management programs are in development [3]. "Smart grid" control systems manage energy production, grid operations and demand side management for optimizing system performance. Energy market reform programs are promoting electricity production by the private sector, which has usually limited abilities to raise capital for very large plants. Energy market reforms also result with distributed generation systems.

SMR have the right unit size for integration into the future electrical system. Enhanced load following and relatively modest capital cost requirements of SMR also suitable for future electrical systems.

SUMMARY AND CONCLUSIONS

SMR have good safety, security and economics features. The SMR siting, and operation features may suit well the future electrical systems. Moreover, SMR integration in future electrical system may be part of the solution for achieving environmental goals along with energy security of supply.

Whether SMR will fulfill the prospects for clean, secure and affordable electricity supply and the prospects for the nuclear industry renaissance – it will depend on the commitment of governments to promote building and operating SMR that will demonstrate the enhanced features and regain the public confidence in nuclear energy, as well as continuous investment in SMR R&D.

Such positive developments may be suitable for Israel conditions since the SMR suite both to Israel future electrical grid as well as to the Shivta site in the Negev intended to the first nuclear power plant.

REFERENCES

1. *"INTERIM REPORT OF THE ANS PRESIDENT'S SPECIAL COMMITTEE ON SMR GENERIC LICENSING ISSUES"*, American Nuclear Society (ANS), 2010.
2. D. Shropshire, *"Economic viability of small to medium -sized reactors deployed in future European energy markets"*, Progress in Nuclear Energy 53 (2011) 299-307.
3. http://www.smartgrid.gov/the_smart_grid#smart_grid

Posters (Wednesday, February 12, 2014 15:30)

Mechanical Properties Characterization for a Cylindrical Fuel Clad Using the Segmented Expanding Cone-Mandrel (SEM) Method

M. Tubul, B. Ostraich, E. Shwageraus

Ben Gurion University P.O.B. 653 Beer-Sheva 8410501 Israel

INTRODUCTION

Rotem Industries is one of the partners in the JHR project. The Project deals with research reactor facilities. To train future employees for recruitment, The Company supports and assists students in undergraduate and master's degrees. This work is part of an MSc thesis accompanied by Rotem Industries instructors.

Modern demand for higher burn-up of nuclear fuels presents complicated safety related challenges for testing of both new and existing fuel cladding materials for integrity during long term operations, and especially for several known phenomena that may be expected to occur during the fuel rod operation.

Irradiation damage, as well as temperature and pressure induced creep along with several other factors have significant effect on cladding mechanical properties. Also, the small (usually about 300 μm) fuel to clad gap in as-received fuel usually closes rather rapidly due to high external pressure and the thermal expansion (swelling) of the fuel pellet.

The combination of these effects often leads to full contact between the pellet and the cladding inner wall. Since the fuel pellet is also subjected to non-uniform temperature gradient and operates at high temperatures⁽¹⁾, radial pellet cracking may incur, potentially compromising the integrity of the cladding and allowing fission products release to the coolant⁽²⁾. This process is known as PCI (Pellet cladding interaction) and it is of high importance in reactor safety and licensing considerations.

PCI also affects the fuel pellet itself, the ceramic UO₂ pellet geometry often distorts from cylindrical geometry into hour glass shaped sections. It is induced also by several other phenomena (Stress Corrosion Cracking, Chemical reactions, etc.), and leads to stress concentrations in some contact areas between fuel and clad. It is in fact one of the major cladding failure mechanisms. Therefore, it must be addressed when designing the fuel.

The characterization of mechanical properties is very important in the fuel design stages to adequately address the phenomena mentioned above.

Usually, the stress strain curves, produced in uni-axial tests, describe the mechanical properties of materials sufficiently well. In the case of fuel cladding, the stress regime is tri-axial. Therefore, properties obtained in uni-axial tests do not provide sufficient information on material properties required for obtaining an accurate prediction of cladding behavior. As a result, a requirement is emerging for a new simulation method of the PCMI phenomenon, suitable also for irradiated materials. Several works on this subject were published. In one of these works, the SEM⁽³⁾ (segmented expanding cone mandrel) test is used. This test simulates the clad loading due to thermal expansion of cracked fuel, by inducing clad radial loading through expanding segments, which are placed inside the cladding tube (Fig 1).

In this work, we propose a method for obtaining a more accurate evaluation of the material properties. By using a three-dimensional FEM model based on the SEM test, our method allows a better understanding of the three-dimensional complex stress fields occurring during pellet-cladding interaction⁽⁴⁾, including stress concentrations at the edges of the segments. In addition, our model takes into account the normal and shear stress distribution in all directions, the friction between all surfaces, the reaction force and the strain distribution in the clad. For validation of the proposed method, the FEM simulation predictions are compared with experimental data from the literature.

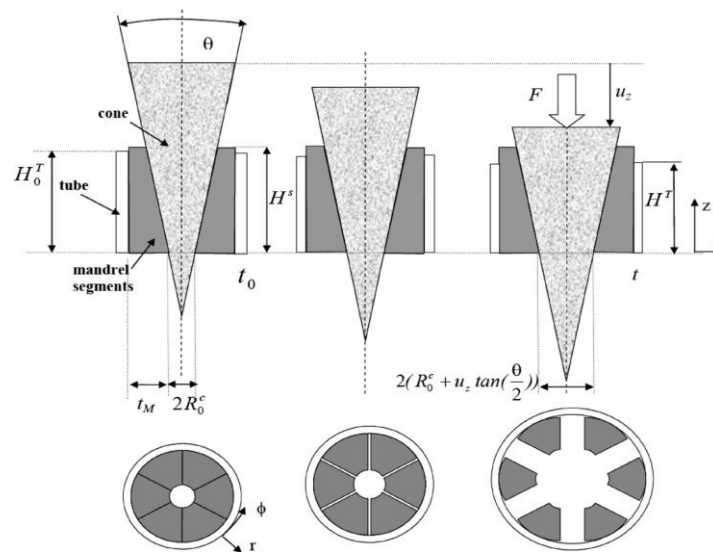


Figure 29-Schematic illustration of the principles for the cone mandrel test ^[1]

Finite element modeling

The following analysis concentrates on the segmented expanding mandrel (SEM) test ⁽³⁾ shown in Fig.1, in which a Cartesian and cylindrical coordinate system is defined. The SEM includes a cylinder (cladding), a segment, cone and block. The parametric FEM is performed using the finite element software ANSYS-APDL. The 3D eight-node solid element SOLID186 is used to mesh the structure. The effects of friction are represented by the Ansys Coulomb friction model algorithm on the contact between the clad segment cone and block. The finite element mesh model is shown in Fig.2.

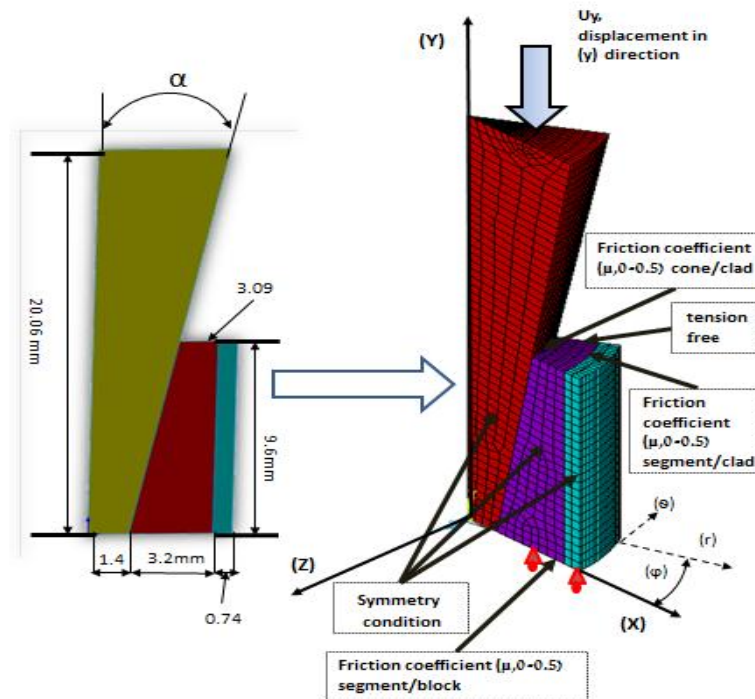


Figure 30-meshing and boundary condition

RESULTS

The reaction forces from the 3D-FE model are compared to the SEM test ⁽¹⁾ experimental results. The load displacement curves are shown in Fig 3. The model results are in good agreement with the experimental curves. This suggests that the friction coefficient (μ) in both cases is similar and equal to 0.04. The difference between the FE model and experimental curves comes from the difference between the material model fed into the 3D-FE model and the actual properties of the material used in the experiment.

Fig 4a presents the stress-strain curves of Zircaloy 2 obtained by: 1. uniaxial tensile test. This data is the material model fed into the 3D-FE model 2. Ansys 3D-FE model. The data in this curve is calculated for the clad outer perimeter. 3. Feeding the data in fig 3 to a semi-analytical model ⁽³⁾, transforming it to stress-strain. Curves 2 and 3 are calculated using $\mu=0.04$. It can be seen that all curves are similar. In the case of

$\mu=0.5$ (Fig 4b), the curves are very different from each other: In the semi-analytical curve, the material strength is much lower, the elastic slope is lower and the strain hardening is more moderate. All results assume isotropic material. Clearly, the friction coefficient has a large effect on the Semi-analytical computed stress-strain curve. In order to reduce this effect dramatically, a correction for the semi-analytical model was developed. Its effect can be seen in Fig. 4b, the stress-strain curve calculated using the semi-analytical model changed when the friction coefficient increased, but material mechanical properties are expected to be independent of the friction in the measuring system. Thus, the semi-analytical model needs to be modified by adding a mathematical expression that fits the semi-analytical curve to the FE model curve. Eq. 1 presents such an expression.

$$(1) \quad \sigma_{\theta} = \begin{cases} \text{if } \varepsilon \leq 0.0034 ; E * \varepsilon \\ \text{if } \varepsilon > 0.0034 ; K * \varepsilon^n \end{cases}$$

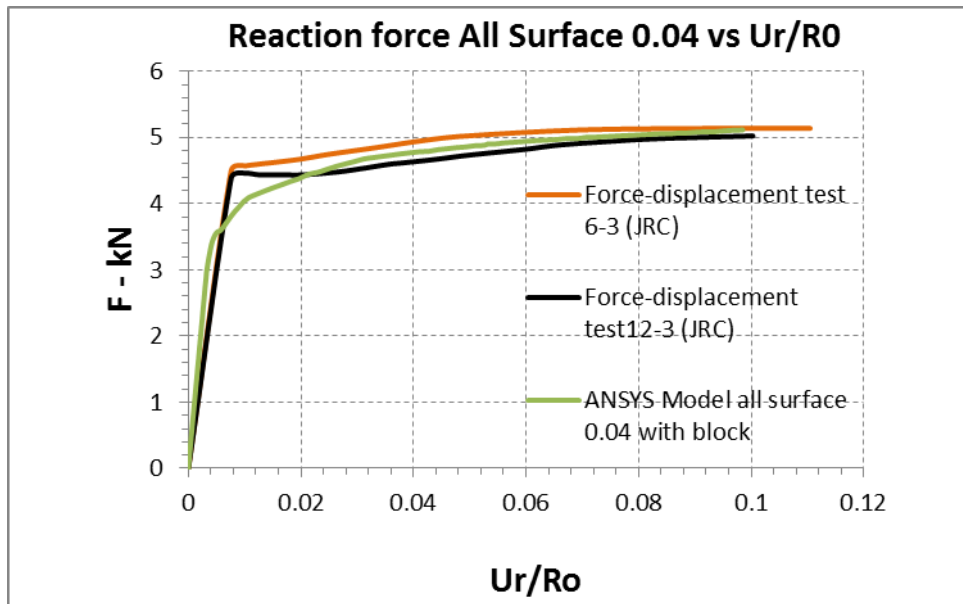


Figure 31-Force-displacement relationship with a friction coefficient of 0.04 cone / segment, segment /clad compared with experiment cone segment produced from STAVAX [3]

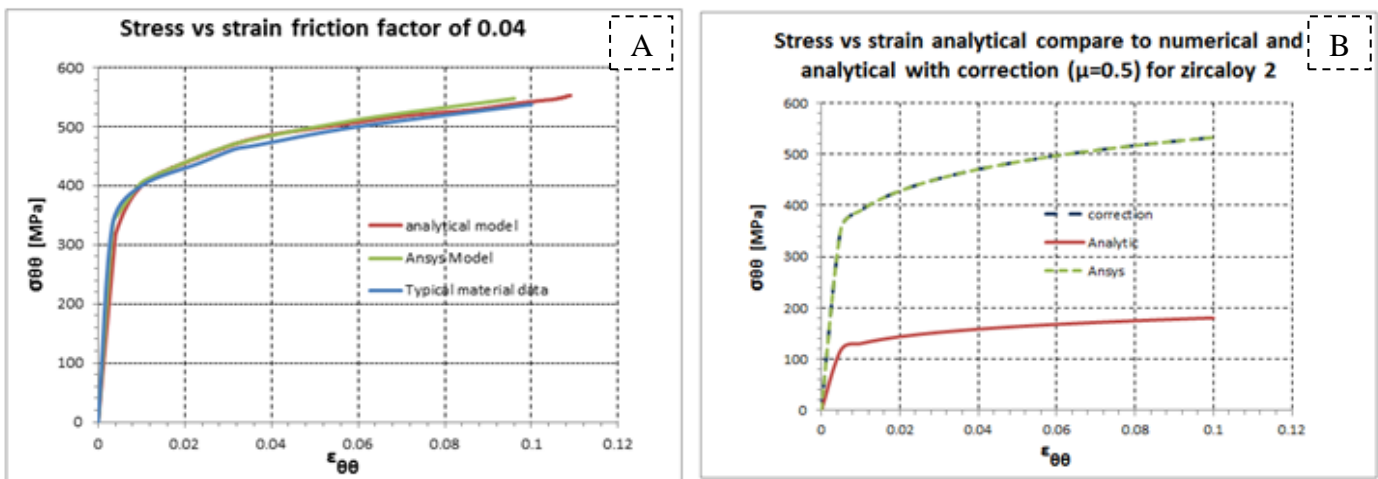


Figure 4- calculated stress-strain curve in ANSYS versus stress-strain curve calculated using force curve (Figure 4) taken through the calculation results on ANSYS model and entered the semi-analytical model [3]. A- Friction coefficient of 0.04 B- friction coefficient of 0.5

CONCLUSIONS

In the current stage of the research, the following conclusions can be drawn:

- The 3D FE model can accurately reproduce the experimental results after calibrating the friction coefficient.
- The 3D FE model is suitable for the analyses of local failure mechanisms and distribution of stresses/strain and stress concentration in the clad segmented interaction.
- A correction for the semi-analytical model was developed using the 3D-FE model. The corrected semi-analytical model is independent of the friction coefficient.
- The 3D-FE model can be used to obtain the friction coefficient from experimental results.

For summing up, a 3D model is developed to correct the analytical model which intends to compute the stress-strain curve of a clad from SEM test. The analytical model happens to fail at high friction factors. The analytical correction, developed by the 3D model, reduces the dependency of the results at the friction and suggests useful method for compiling SEM models.

REFERENCES

- [1] Lustman, B., 1979. *Zirconium technology – twenty years of evolution*. In: *ASTM-STP 681. American Society for Testing and Materials*, pp. 5–18.
- [2] Cacuci, D.G., 2010. *Handbook of Nuclear Engineering, Volume 1, Nuclear Engineering Fundamentals*. Springer
- [3] Karl-Fredrik Nilsson, Oliver Martin, Cesar Chenel-Ramos, Jose Mendes *The segmented expanding cone-mandrel test revisited as material characterization and component test for fuel claddings*.
- [4] Nakatsuka, M., Koizumi, K., Hayashi, Y., Kawahara, A., 1982. *Measurement of friction coefficient and strain concentration of barriered fuel claddings under mechanical interaction with pellets*. *J. Nucl. Sci. Technol.* 19 (4), 336–339.
- [5] Pickman, D.O., 1994. *Zirconium alloy performance in light water reactors: a review of UK and Scandinavian experience*. In: *ASTM-STP 1245. American Society for Testing and Materials*, pp. 19–32.

Posters (Wednesday, February 12, 2014 15:30)

Ground Shock Resistant of Buried Nuclear Power Plant Facility

D. Ornai, A. Adar, E. Gal

Ben-Gurion University of the Negev, PO Box 653, Beer-Sheva, 84105, Israel

Ground Shock Resistant of Buried Nuclear Power Plant Facility

D. Ornai^{1,2}, A. Adar¹, E. Gal¹

¹*Department of Structural Engineering, Ben-Gurion University of the Negev*

²*Protective Technologies Research & Development Center, Ben-Gurion University of the Negev,
PO Box 653, Beer-Sheva, 84105, Israel*

INTRODUCTION

Nuclear Power Plant (NPP) might be subjected to hostile attacks such as Earth Penetrating Weapons (EPW) that carry explosive charges. Explosions of these weapons near buried NPP facility might cause collapse, breaching, spalling, deflection, shear, rigid body motion (depending upon the foundations), and in-structure shock. The occupants and the equipment in the buried facilities are exposed to the in-structure motions, and if they are greater than their fragility values than occupants might be wounded or killed and the equipment might be damaged, unless protective measures will be applied. NPP critical equipment such as pumps are vital for the normal safe operation since it requires constant water circulation between the nuclear reactor and the cooling system, including in case of an immediate shut down. This paper presents analytical- semi empirical formulation and analysis of the explosion of a penetrating weapon with a warhead of 100kgs TNT (Trinitrotoluene) that creates ground shock effect on underground NPP structure containing equipment, such as a typical pump. If the in-structure spectral shock is greater than the pump fragility values than protective measures are required, otherwise a real danger to the NPP safety might occur.

NUMERICAL EXAMPLE

Underground explosion creates free field motions formulated by Drake & Little [1], [2], [3]. The analysis of NPP buried facilities resistant to the in-structure shock caused by the external ground motions is based on the response shock spectra method [2],[3],[4]. A response spectrum is calculated and presented on a special figure with four logarithmic axes. Both the spectral motions (displacement, velocity, and acceleration) of a damped structure subjected to support excitations as a function of frequency and the installed equipment fragility spectrum are presented on the same figure (for example see figure 3). If the spectral in-structure motions are greater than the equipment fragility than the equipment is supposed to be damaged with direct implication on the NPP unsafe operation. Hence, for an existing structure the equipment may be mounted to proper isolator. In a new facility external base isolators may decrease the excessive motions, and additional external protective layers may lower the ground shock and the in-structure shock as required. A numerical example of a response spectrum of an underground structure with an internal pump coping with motions caused by explosive charge stand-off distances of 5m and 10m was carried. The configuration of the structure and the explosive charge is presented in Figure 1.

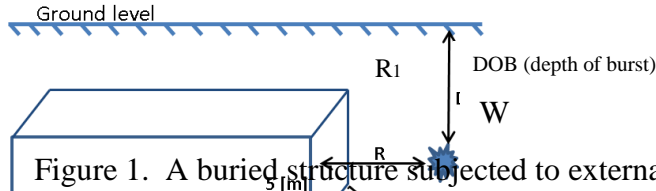


Figure 1. A buried structure subjected to external underground explosion

The soil properties of dense and poorly graded dry sand are as follows [2]: seismic velocity $c=365.76$ [mps (meters per seconds)], and attenuation coefficient $n= 2.6$. The explosion parameters are: weight of charge $W=100(\text{kgs})_{\text{TNT}}=73(\text{kgs})$ C4, and coupling factor $f=1$ (fully coupled). The US army and air force protective structures manuals [2],[3] suggests the following procedure to evaluate the in-structure response spectrum including some fragility spectrums of typical equipment exposed to shock. The in-structure motions are the average ground motions ranging between the front wall that is exposed directly to the explosion and the back wall. The formulas for the averaged acceleration- $A(\text{g}'\text{s})$, velocity- $V[\text{fps}$ (feet per seconds)], and displacement- $D(\text{ft})$ are:

$$A_{avg} = \frac{50 * f * c * W^{\frac{n+1}{3}} * [R_1^{-n} - R_2^{-n}]}{W^{\frac{1}{3}} * n * [R_2 - R_1]} \quad [g's]$$

$$V_{avg} = \frac{160 * f * W^{\frac{n}{3}} * [R_1^{-n+1} - R_2^{-n+1}]}{(n - 1) * [R_2 - R_1]} \quad [fps]$$

$$D_{avg} = \frac{W^{\frac{1}{3}} * 500 * f * W^{\frac{n-1}{3}} * [R_1^{-n+2} - R_2^{-n+2}]}{c(n - 2) * [R_2 - R_1]} \quad [ft]$$

f , c , n , W , and R_1 , R_2 are the coupling factor (for deep explosion $f=1$), soil seismic velocity (fps), dimensionless attenuation coefficient, charge weight (in lbs of C4 high explosive that are equal to 1.37 lbs of TNT), distance between the explosive charge and the front wall, and distance between the explosive charge the back wall.

The values of the free field ground motion are larger than those in the structure since the distances to the various points on the structure's front wall are larger than the shortest distance to the wall center, R_1 . Using a reduction factor approach proposed by [2] corrects the ground motions in relation to the explosion stand-off and the structure geometry as shown in Figure 2.

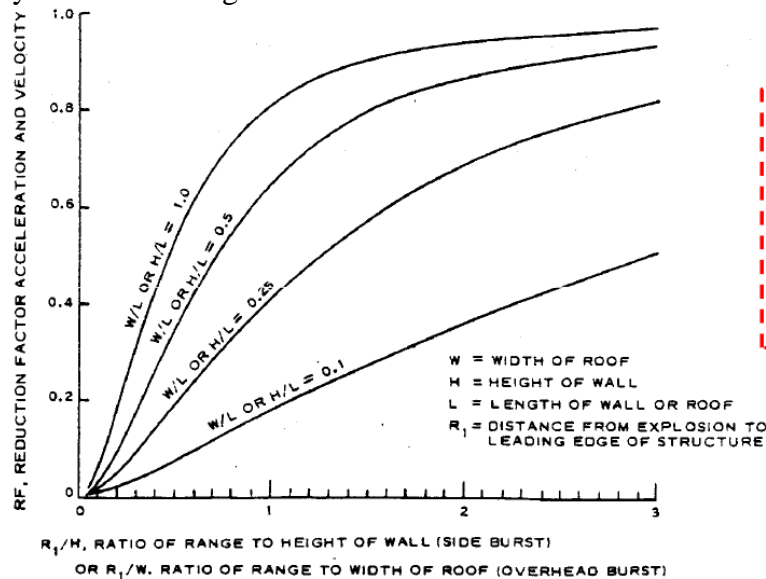


Figure 2. Reduction factor of in-structure acceleration and velocity regarding side burst ($H=5\text{m}$, $L=10\text{m}$)

For small amounts of structural damping (5-10% of the critical damping ratio) it is recommended to multiply the maximum motions by factors 1, 1.5 and 2 for displacement, velocity and acceleration respectively [2]. The physical units of the shock spectrum are taken in inches (in) for the displacement, inches/sec (in/sec) for

the velocity and g's (gravity multiplier) for the acceleration. The calculated spectral in-structure motions are shown in Table 1.

Table 1. Spectral motion values due to in-structure shock caused by two external underground explosions

Explosion stand-off, R	Motion type	Average Values	RF-Reduction Factor	Spectrum factor	Spectral motion values
5[m] , 16.4[ft]	Acceleration [g's]	9.38	0.63	2	18.76[g's]
	Velocity [in/sec]	7.52		1.5	11.28[in/sec]
	Displacement [in]	0.91		1	0.91[in]
10[m] , 32.8[ft]	Acceleration [g's]	1.98	0.84	2	3.95[g's]
	Velocity [in/sec]	2.96		1.5	4.44[in/sec]
	Displacement [in]	0.47		1	0.47[in]

At a stand-off of 5 meters the blast produces base motions that for some frequencies are greater than the pump fragility, hence protective measures are necessary (Figure 3). At a stand-off of 10 meters the blast produces motions that are smaller than the pump fragility and there is no need for protection.

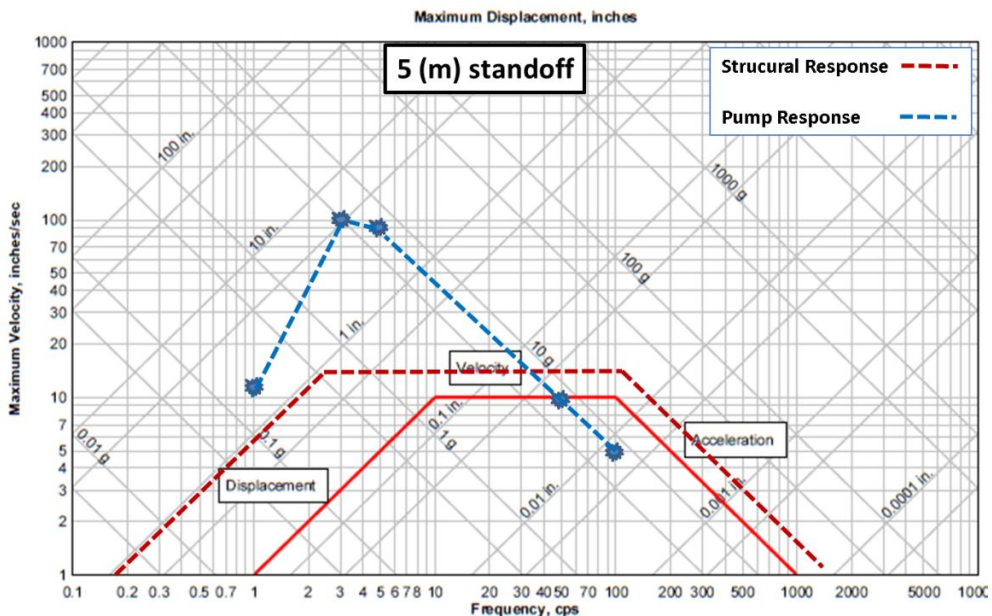


Figure 3. Pump fragility versus in-structure shock spectra due to external 100 kgs. TNT exploding 5 meters from the structure

SUMMARY

Analytical semi empirical method based on Little & Drake method enabled in-structure motion analysis due to external buried explosion. At 5 meters stand-off between the explosive charge and the front wall the blast creates in-structure motions that are greater than the pump fragility. In the case of existing structure protective measures such as mounting the pump to a proper isolator is required. For a new designed structure using base isolators or external protective layers should be considered. Similarly any underground NPP facility may be analyzed.

REFERENCES

1. Drake J.L., and Little, C.D.Jr. *Ground shock from penetrating conventional weapons*, The interaction of non-nuclear munition with structures, Symposium proceedings, Colorado USA (1983).
2. *Fundamentals of Protective Design for Conventional Weapons, TM5-855-1*. US Army, (1986).
3. Drake, J., Twisdale, L., Frank, R., Dass, W., Rochefort, M., Walker, R., Britt, J., and Sues, R. *Protective construction design manual ESL-TR-87-57*. US Air Force

Engineering and Services Center, Tyndall Air Force Base, Florida, (1989).

4. Harris, C. M., and Piersol, A. G. *Harris' shock and vibration handbook*, McGraw-Hill, New York, (2002).

Posters (Wednesday, February 12, 2014 15:30)

Performance of SNRC in MAPEP Proficiency Tests During 2005-2013

O. Aviv, Z. Yungrais, S. Moscovici, M. Brandis, C. Tzur, L. Broshi, T. Reimer, R. Oren-Shemesh,
G. Haquin

Soreq Nuclear Research Center, Yavne 81800, Israel

INTRODUCTION

The Mixed Analyte Performance Evaluation Program (MAPEP) is organized by the United States Department of Energy as a quality assurance tool for radiological and chemical laboratories around the world. Matrices of vegetation, soil, air filter and water, spiked with mixed radionuclides and stable elements are prepared and sent to participating laboratories every 6 months. The participating labs are required to identify and quantify radionuclides and stable elements using their standard methods⁽¹⁾ and report the results within sixty days. False positives are also routinely examined. The performances are assessed and sent to the participating laboratories.

The radiation measurements laboratories at the Radiation Safety Department (RSD) at Soreq Nuclear Research Centre (SNRC) continually participates in MAPEP since 2005 for gross alpha and beta, tritium and uranium in water and gamma emitting radionuclides in the previously mentioned matrices. In this paper we present an analysis of SNRC performance up today.

MATERIALS AND METHODS

Gamma emitting radionuclides are measured from the four matrices by gamma spectrometry using a high purity germanium (HPGe) detector. Efficiency, true coincidence summing corrections and decay corrections are applied where required.

Gross alpha and beta in liquid samples are measured by low background coincidence proportional counting. Tritium in water is performed by low background liquid scintillation using a Quantulus1220 (PerkinElmer) while for uranium isotopes selective extraction liquid scintillation alpha counting using the same type of instrument.

In the following we specify the materials supplied by MAPEP and the preparation procedure for the actual samples which are measured.

Vegetation: Two plastic jars consisting of 95 gr and 10 gr of finely milled grass hay (identically spiked) are supplied. The sample with 10 gr are placed in a dedicated plastic container and sealed with silicon.

Soil: Sample containing 300 gr of soil is supplied in a plastic jar. All 300 gr are transferred into a dedicated plastic container which fits to the measuring apparatus.

Air filter: A thin air filter (diameter of 47 mm, width of 1 mm) made of glass fiber is supplied. The filter is measured "as is", i.e. without any preparation.

Water: Two bottles of 1 liter of water each are supplied. One bottle is used for identification of gamma, alpha and beta emitters (RSD labs participates in the measurement of ^3H , ^{234}U , ^{238}U only). The other bottle is used for gross alpha-beta measurements. For gamma emitters, the preparation method involved transfer of 200 ml into a dedicated plastic container. For gross alpha measurement the standard co-precipitation method⁽²⁾ is used. The method consists of co-precipitation of Ra, U and Th isotopes with BaSO_4 , FeO_3 . Gross beta sample preparation is according to the standard evaporation method⁽²⁾. For Tritium in water, a sample of 150 ml of water is cleaned and purified through active charcoal powder and then filtered and distilled (boiling and condensed) to achieve a constant quenching property of the sample mixed with the inorganic scintillation solution. For uranium isotopes measurements (^{234}U and ^{238}U), a sample of 200 ml of water is transferred into a dedicated container which is first heated to remove radon and CO_2 . After cooling, the sample is mixed with the extraction cocktail (HDEHP and liquid scintillator), and later a known portion is measured by a low background liquid scintillation counter (Quantulus1220, PerkinElmer).

The evaluated parameters in the proficiency tests are the activity concentration and the corresponding uncertainty for each nuclide and for each matrix. Reporting of activity⁷ was performed in accordance to

⁷For cases where a nuclide was not identified, the minimal detection activity was reported.

MAPEP instructions (i.e. decay corrected to the requested reference time). The acceptance criteria for receiving a passing grade (“A”) defined by MAPEP is given for a result which is within a relative deviation⁸ of <20% than the reference value. A passing grade with warning (“W”) is given for a relative deviation within 20%-30%. A fail grade (“N”) is given for a relative deviation of >30%.

RESULTS

Table 1 shows the performance level in percent (i.e. number of “A”+”W” grades) for all of the examined radionuclides in each of the four matrices for all tests during 2005-2013. Tests involving detection and quantification of the most of the gamma emitters (⁴⁰K, ⁵⁴Mn, ⁵⁷Co, ⁶⁰Co, ⁶⁵Zn, ¹³⁴Cs, ¹³⁷Cs, ²⁴¹Am) in all matrices as well as Uranium isotopes and gross alpha and gross beta in water are mostly graded “A”. The low energy gamma emitters ²⁴¹Am and ⁵⁷Co were given the highest amount of fail grades in water and vegetation matrices. Tests with ³H were only partly good, though we note that since 2010 a significant improvement was achieved after a validation process was performed.

Submitted data including activity concentrations, and the reference values within the period of 2005-2013 (conducted once/twice per year, altogether 16 tests) were processed and analyzed. Figure 1 (left) shows the average deviation (over all tests) between the submitted result and the reference value for the studied nuclides and for the four matrices (vegetation, soil, filter, and water).

Non-zero deviations⁹ are observed in practically all matrices and radionuclides. The deviations in the gamma emitters may be attributed to a significant offset in the used efficiency curve. The relatively large deviation in the low gamma energy emitter ²⁴¹Am is attributed to the very low activity concentration of the nuclide which is best suited for alpha spectrometry methods rather than for gamma spectrometry as the minimal detection activity level of the HPGe detection system is usually above the reference values.

The large deviation in ³H is attributed to a previous sample preparation method which was updated in 2010. Since then the performance was successful.

The few deviations in Uranium isotopes results are attributed to non-equilibrium between the isotopes in depleted uranium samples. The updated measurement method (since 2011) accurately determines the uranium activity concentration not depending on uranium depletion/enrichment.

Nuclide	Success Level			
	Vegetation	Soil	Filter	Water
⁴⁰ K	-	100%	-	100%
⁵⁴ Mn	100%	100%	100%	100%
⁵⁷ Co	93%	100%	100%	100%
⁶⁰ Co	100%	100%	100%	100%
⁶⁵ Zn	100%	100%	100%	100%
¹³⁴ Cs	100%	100%	100%	100%
¹³⁷ Cs	99%	100%	98%	98%
²⁴¹ Am	80%	100%	87%	64%
³ H	-	-	-	90%
²³⁴ U	-	-	-	85%
²³⁸ U	-	-	-	93%
Gross α	-	-	-	94%
Gross β	-	-	-	94%

Table 5: Grades per nuclide and per matrix for MAPEP tests during 2005-2013.

⁸For gross alpha/beta emitters, the acceptable values are within a relative deviation of <70%.

⁹Deviations in reported results caused by typos were omitted from this average as this report studies technical expertise.

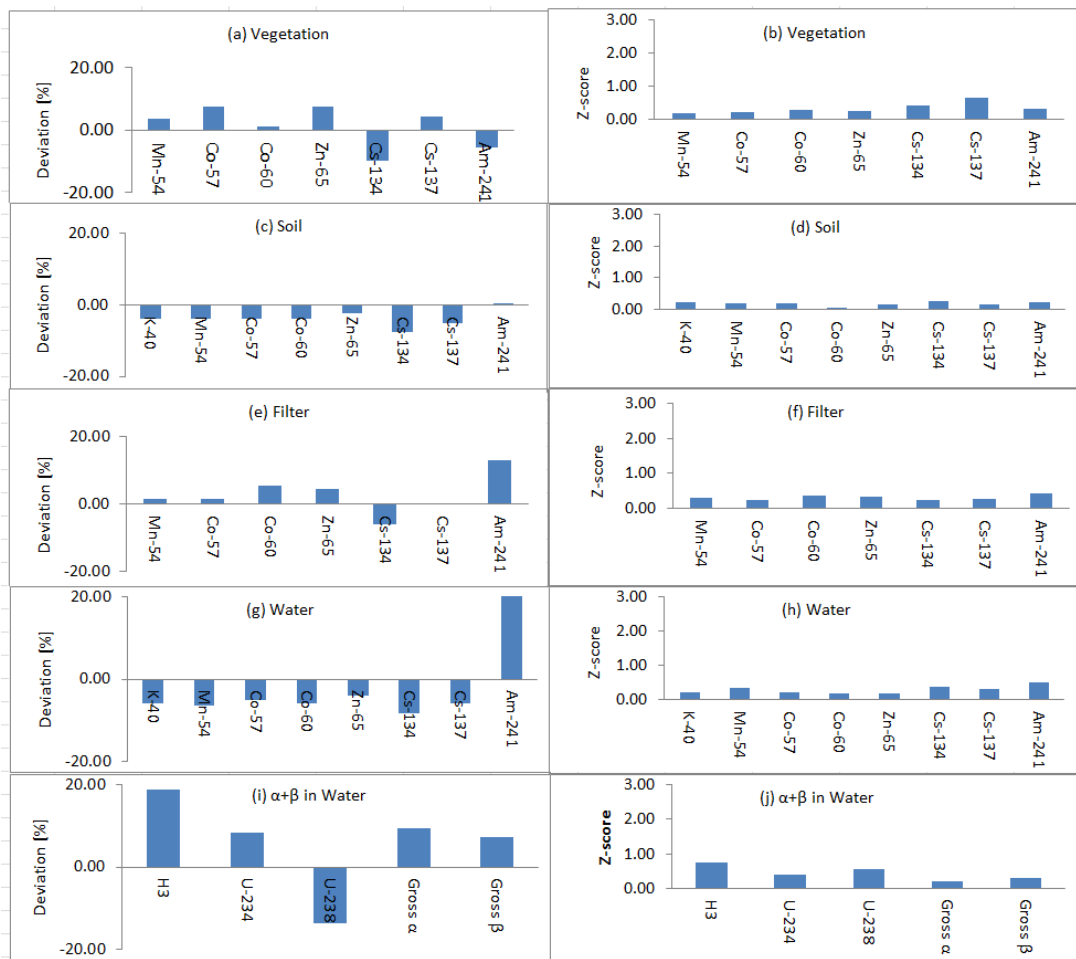


Figure 32: Averaged deviation (left – a,c,e,g,i) and averaged z-score (right – b,d,f,h,j) for the examined radionuclides in four matrices: vegetation, soil, filter and water.

Most of the reported results for nuclides in the four matrices are within the accepted values, while alpha and beta emitters exhibit slightly elevated Z-scores.

An additional performance evaluation has been carried out using the statistical test Z-score which takes into account the relative deviation between the assigned value and the lab result together with the corresponding uncertainties, given by $\zeta = \frac{|A_{lab} - A_{ref}|}{\sqrt{\Delta A_{lab}^2 + \Delta A_{ref}^2}}$. Where A_{lab} is the reported activity; A_{ref} is the assigned activity;

ΔA_{lab} and ΔA_{ref} are the corresponding uncertainties. Results with $\zeta < 3$ are considered accepted values.

Figure 1 (right) shows the averaged (over all tests) Z-score per nuclide and per matrix.

Figure 2 shows the performance of the lab in MAPEP tests over the period 2005-2013 in terms of success level in percent ($=$ [number of “A” + “W” grades]/[total nuclides examined]). The lab exhibited good performance over the years for all matrices, though occasional failures were recorded in some years especially for vegetation and water matrix. The main reason for these failures is miss-quantification in the low energy gamma emitters (^{241}Am and ^{57}Co).

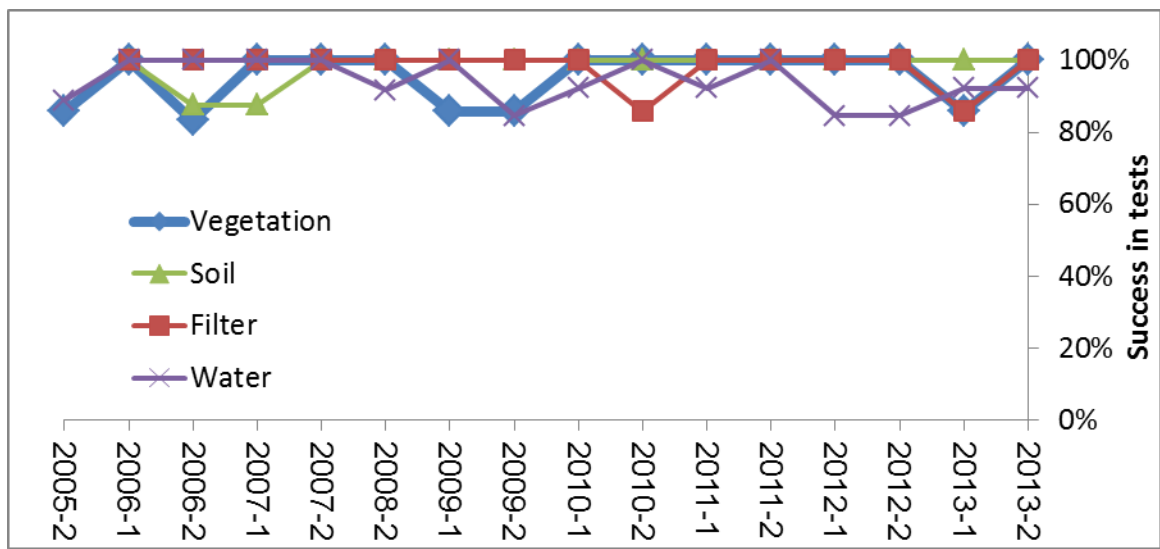


Figure 33: Success level for the four matrices in MAPEP tests during 2005-2013.

CONCLUSIONS

The performance of the radiation measurements laboratories at Soreq Nuclear Research Centre in MAPEP proficiency tests has been presented. There is a very good overall success in these tests over the years, although deviations were found in some nuclides which need to be addressed.

REFERENCES

1. DOE\MAPEP website: <https://mapep.inl.gov/>
2. Standard methods for the examination of water and waste water 22nd edition, American Public Health association (2012).

Natural Circulation Modeling in MTR Fuel Geometry in Research Reactors

Y. Aharon

NRCN, P.O.B. 9001, Beer – Sheva, Israel

INTRUDUCTION

In many research reactors the reactor can operate under either forced or natural convection modes. Under forced convection, the primary cooling system removes the heat generated in the reactor core through a heat exchanger to the secondary cooling system, which releases this thermal energy through the cooling tower to the atmosphere. Under natural convection operating mode, the generated nuclear power imply heats up the pool water, and is ultimately dissipated through the pool surface to the containment atmosphere. Hence, the large pool provides a heat sink for the energy generated within the core. The pool surface is open to the containment atmosphere, where thermal energy exchange via evaporation and convection heat transfer can occur. In case of electrical supply failure or mechanical / electrical failure in the pumps, a Loss of Flow Accident (LOFA) will occur. In this case natural circulation mechanism may be the only mechanism that can be use to remove the decay heat from the core.

Modeling and modeling validation of natural circulation is an important issue in designing and commissioning of nuclear reactors. Most of the designers are using commercial codes like RELAP5, TRAC and THYDE-W to simulate the behavior of the core under natural circulation. Validation of those cods is done by comparing between different codes and comparing the calculated results with results from scaled experimental systems. In the last two decades, CFD calculations are also used for calculations and validation of the commercial codes⁽¹⁾.

In case of research reactors and in case of Loss of Flow Accident, a simple analytical model can be use for preliminary and advanced calculations of the reactors.

The purpose of this paper is to present and validate a simple model for thermohydraulic calculation of research reactor in natural circulation mode.

THE MODEL

The flow loop in a pool type research reactor, in case of natural circulation, consists of the heat source (the core) which works in low power (up to about 100 kW) or in case of decay heat after shutdown. The inlet of the water from the pool to the lower plenum of the core is through the flapper valves which are opened automatically when the flow rate reaches a limiting value of about 10% of the nominal flow rate. The water entering the lower plenum and flowing up trough the inlet nuzzle of the fuel rod to the fuel plates / pins zone. In most of the research reactors the water continues to flow through the exit nozzle of the fuel rod and mixing with the water in the pool. In few research reactors like the Australian MAPLE and the Korean HANARO and also in the commercial heating reactor SLOWPOKE, the water continue to flow to a chimney and than mixing with the water in the pool.

Modeling of a natural circulating in that loop based on a balance between the friction losses along the loop due to the flow rate ($\Delta p_{tot,f}$) and the moving force (pressure drop) due to the density decreased by the heating of the water which causing buoyancy force ($\Delta p_{tot,b}$).

$$(1) \quad \Delta p_{tot,f} = \Delta p_{tot,b}$$

In each zone the friction losses were calculated as follow.

For the longitudinal friction losses: (2)
$$\Delta p_{L,i} = \left(f \frac{L}{D_H} \rho \frac{v^2}{2} \right)_i$$

And for local friction losses: (3)
$$\Delta p_{loc,i} = \left(K \rho \frac{v^2}{2} \right)_i$$

The friction coefficient f in eq. 1 was taken according to the Reynolds number in the calculated zone. In case of natural circulation the Reynolds number is usually defined a laminar flow regime. In this case the friction coefficient f is calculated as follow: (4) $f = C/Re$

where the value of the constant C depends on the channel geometry. For the local friction losses the constant K was taken as approximated value $K=1$.

The velocity v in each zone is calculated from the mass flow rate and the cross section of the calculated channel.

The moving force (buoyancy pressure drop) is depending on the mass flow rate of the coolant, the heating power of each zone and the inlet and outlet level of the calculated zone as follow:

$$(5) \quad \Delta p_{b,i} = g\Delta z(\rho_{inf} - \rho_i)$$

Where Δz is the elevation difference between the inlet and the exit of the channel, ρ_{inf} is the pool water density and ρ_i is the average density value of the water in the calculated zone. The density value in each zone is varying with the coolant temperature. That value was calculated by using a curve fitting of the density vs. temperature of the water. The water temperature gradient in each zone (ΔT_i) was calculated from the energy equation:

$$(6) \quad \Delta T_i = T_{in} + \frac{q_i}{\dot{m}Cp}$$

Where T_{in} is the inlet temperature to the calculated zone, q_i is the heating power which supply to the water along the calculated zone, \dot{m} and Cp are the mass flow rate and the heat capacity of the coolant, respectively. In case of heating zone (along the fuel plates) the average temperature was calculated between the inlet and the outlet temperature and the average density was calculated from the density function with that temperature.

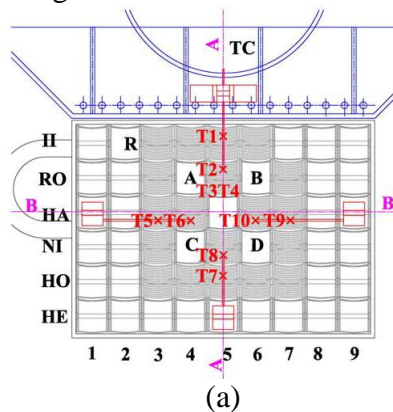
Model Validation

To validate the present model, experimental data from the Kyoto University Research Reactor (KUR) was used which is a pool type 5MW research.

Experimental temperature measurements of water in various locations in the core in natural circulation mode of the KUR are presented in ref. 2. The description of the KUR core is presented in Fig. 1(a) and the fuel rode in Fig. 1(b). The core consists of 19 standard fuel rods and 5 control rods (A,B,C,D and R in Fig. 1). Standard fuel rode consist of 18 fuel plates 1.5 mm in thick and 625.5 mm in length and 75.9 mm in with. Between the fuel plates, there is a 2.8 mm width water channel for the coolant flow. The location of the water temperatures measurements is presented in Fig. 1(a) and the power distribution between the fuel rods for 100 kW operation power is presented in Table 1. It was also mentioned in reference 2 that the ratio between the thermal power and the nutronic power is 0.9. The two thermocouples T3 and T4 were respectively arranged in the vertical positions of 5 cm and 10 cm above the position of thermocouple T2.

The channel power from Table 1 was normalized with the core power to get the values in various operation core powers.

In the model it was assumed that the main flow resistance in the flow loop is the resistance of the channels between the fuel plates and the inlet nozzle of the fuel rod, where the flow resistance inside the lower plenum is negligible. Sensitivity calculation was done for the inlet flapper resistance. In ref. 2 the dimensions of the flapper are not provided and we assumed that the flapper has (in total open position) typical circular tube geometry of 0.2 m inside diameter and length of 0.5 m⁽³⁾.



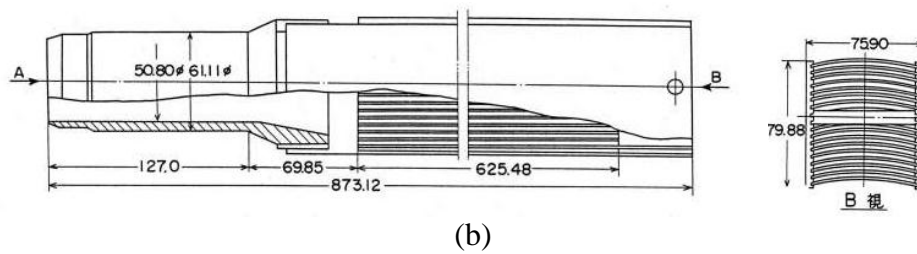


Figure 1: a- Fuel rods arrangement in the KUR core. b- Fuel rod geometry ⁽²⁾.

Table 1: Power distribution between the fuel rods at reactor operating power of 100 kW⁽²⁾.

Output Power : 100kW									
	1	2	3	4	5	6	7	8	9
II	G	1.79	3.75	4.21	4.22	3.79	SSS	G	G
RO	G	G	4.66	2.94	5.77	2.64	3.92	G	G
HA	G	G	4.90	6.11	Hyd	5.71	4.24	G	G
NI	G	G	4.68	3.02	5.93	2.84	4.11	G	Pn2
HO	G	G	3.94	4.48	4.57	4.27	3.52	G	Pn3
HE	G	G	G	G	G	G	G	G	Pn1

Unit: kW

The total flow resistance of the flapper was taken as a sum of local flow resistance ($K=1$) due to a sudden entrance of the water from the pool to the valve and longitudinal friction losses along the flapper valve tube. It was also assumed that the pool has no resistance to the flow. For conservative calculation it was assumed also that the flow rate through the flapper is the hottest channel flow rate times the number of the fuel rods. The measured temperatures versus the time are presented in ref. 2 for to fuel channels HA-3 and HA-4 for various core operating power up to 100 kW. Comparison between the measured temperatures and the calculated values is presented in Fig. 2.

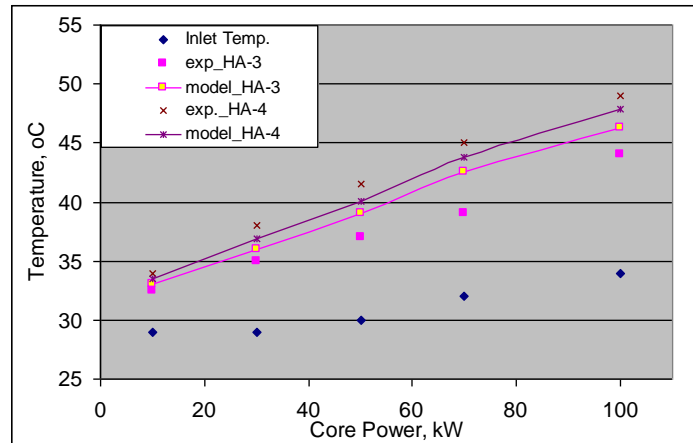


Figure 2: Comparison between calculated and measured exit temperatures

As it can be observed from Fig. 2, a good agreement was achieved between the calculated and the measured values where in fuel rod AH-3 there is a small over prediction of the model and in fuel rod AH-4 the model has a small under prediction in the calculated values.

For calculation of the water and the fuel temperature along the fuel rods it was assumed that the power distribution has a chopped cosine shape with a 30% heat flux value at the plate edge. The fuel plates temperature $T(z)_{wall}$ was calculated as follow:

$$(7) \quad T(z)_{wall} = T_b(z) + \frac{q''(z)}{h}$$

Where $T_b(z)$ and $q''(z)$ are the local water temperature and heat flux, respectively and h is the convective heat transfer coefficient. Based on the Reynolds number in the channel the flow regime is laminar. In this case the value of h was calculated as proposed in ref. 4 by using the following correlation: (8)

$$Nu = \max[Nu = 4(const), eq(9)] \quad \text{for } Re < 2000$$

$$(9) \quad Nu = 0.17 Re_f^{0.33} Pr_f^{0.43} \left(\frac{Pr_f}{Pr_w} \right)^{0.25} \left\{ \frac{g \beta D_H^3 (T_w - T_b)}{\nu^2} \right\}_f^{0.1}$$

The calculated water and the fuel temperatures are presented in Fig. 3 (a) and (b) for fuel rod HA-3 and HA-4 respectively for core power of 100 kW.

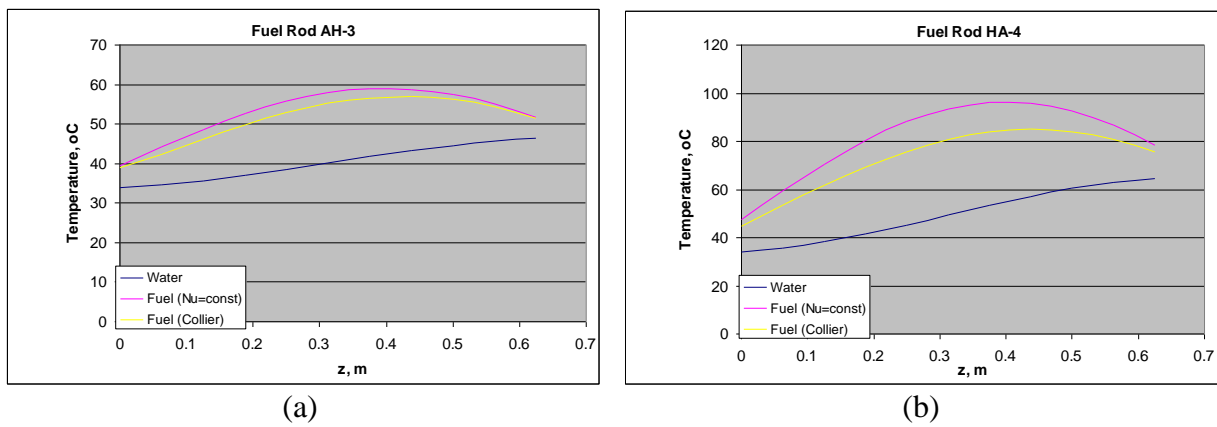


Figure 3: Calculated water and fuel temperature for fuel rod AH-3 (a) and AH-4 (b) at 100 kW core power.

CONCLUSIONS

- A good agreement was achieved by the present model in calculating of the flow rate and the exit water temperatures in a natural circulation mode in plates geometry fuel rod.
- It was found that the inlet plenum and the flapper valve have a negligible flow resistance comparing to the flow resistance of the flow channels in the fuel element.
- Fuel temperature was calculated based on correlations from literature. Validation of those correlations can be done by comparing with experiments from literature.

REFERENCES

- Y. Yan, R. Uddin and N. Sobh, CFD Simulation of a Research Reactor, Mathematical and Computation Supercomputing, Reactor Physics and Nuclear and Biological Applications, France, 2005
- J. Zhang, X. Z. Shen, Y. Fujihara, T. Sano, Y. Takahashi, K. Oono, A. Nakamori, N. Maruyama, K. Hasegawa, T. Tsuchiyama, K. Minami, K. Okumura, T. Yamamoto and K. Nakajima, Experimental Investigation on Natural Circulation Capacity of Kyoto University Research Reactor, NURETH15-125, Pisa, Italy, 2013
- C. Park, M. Tanimoto, T. Imaizumi, M. Miyauchi, M. Ito, M. Kaminga, Preliminary Accident Analysis for a Conceptual Design of a 10 MW Multi-purpose Research Reactor, Japan Atomic Energy Agency, JAEA – Technology 2012 – 039, 2013
- Y. Sudo, H. Ando, H. Ikawa, N. Ohnishi, Core Thermohydraulic Design with 20% LEU Fuel for Upgraded Research Reactor JRR-3, J. Nucl. Science and Technology, 3, pp. 551-564, 1985

A New Approach to Analyse the Effect of Initial Conditions on Steam Explosion In Coolant Injection Mode

I. Baruch¹, G. Widenfeld²

¹*Ben Gurion University of the Negev, Ben Gurion 1, Beer-Sheva, Israel*

²*NRCN, Israel*

ABSTRACT

Reaction between water and molten metal can lead to a very severe accident, caused by Steam Explosion (SE). Although the SE has been widely studied, the effect of dynamic parameters and material properties are still not well established. This study presents a new approach that based on the influence of material properties, jet characteristics and the initial temperatures on the feasibility of SE occurrence in coolant injection (CI) mode. Data from four different studies were cross-referenced, comparing various parameters such as melt and water initial temperatures, material properties and jet parameters for different melts such tin, aluminium, zinc and lead-bismuth eutectic mixture. This study showed that in tin-water system, the thermal interaction boundaries which varied with the jet dynamic properties, indicating that other parameters affecting the phenomena. Regions of low Weber number found as regions where spontaneous SE did not occur. This study shows that analysing the occurrence conditions solely by the melt and water initial temperatures is not applicable, and offers a new approach for further examination of jet parameters and material properties together with melt and jet initial temperatures.

INTRODUCTION

Violent thermal interactions resulting from the sudden contact of a cold vaporizable liquid and a hot liquid may cause high pressure explosions. In nuclear reactors the Steam Explosion (SE) might damage the core vessel and the containment integrity, release radioactive fission products to the environment and risk human health and pollute the environment for years to come. Fuel Coolant Interaction (FCI) can be form in one of these contact modes: Melt Injection (MI), Coolant Injection (CI), Free Fall Melt Drop (FFMD) into coolant and melt flooding by coolant. The current study uses TIZ map together with dynamic properties in order to reveal the SE occurrence conditions.

Due to the complexity of the CI experimental system, there is a lack of experimental data in the literature. Experimental data of the FFMD mode, found useful in interpreting the CI mode data. TIZ (Thermal Interaction Zone) map is the most conventional method to display the conditions leading to SE. These maps depict the areas where SE occur or does not occur depending on the initial melt and water temperatures. TIZ theoretical boundaries commonly defined as melting point (MP) temperature or homogenous nucleation (HN) temperature and minimum film boiling (MFB) temperature, at the interface temperature (1) between the two liquids.

$$T_i = T_{jet} + \frac{T_{melt} - T_{jet}}{1 + \sqrt{\beta}}, \text{ where } \beta = \frac{(k \cdot \rho \cdot C_p)_{jet}}{(k \cdot \rho \cdot C_p)_{melt}} \quad (1)$$

Although a TIZ map analysis is commonly used, this map does not provide sufficient information of other parameters affecting the feasibility for SE occurrence at CI mode. These parameters include jet dynamic properties such as diameter, nozzle height from melt surface, velocity and the amount of water. Material properties such as: thermal conductivity, specific heat, MP, density, surface tension, heat of fusion and more.

The examination of experiments^[1-4], shows that the contact mode has a major influence on the feasibility for SE to occur. From comparison of two experiments in CI mode, conducted with the same materials and initial temperatures, it was found that one may generate SE while the other ends in a violent boiling regime. The main cause for these different results is the jet dynamic characteristics. This fact emphasize that it is impossible to predict SE occurrence in CI mode by using only TIZ map.

Triggering thermal interaction is an essential stage for escalating violent boiling to SE. Some materials as tin have spontaneous triggering mechanism while others, like aluminium or zinc, do not spontaneously triggered. It well known that the triggering mechanism leading towards SE is a local vapour film collapse that generates a shock wave, which moves through the water and extends the film collapses to other sites. Y. Abe et al^[4] found that SE trigger cannot be satisfied when the interfacial temperature (Ti) between the molten material and water is lower than the material melting temperature, even if the vapour film around the

molten material collapsed by the external pressure pulse. However, analysing G. Widenfeld^[1] experiments results of water injection into tin melt, SE does occur even beneath the MP boundary at the interface temperature. External triggers may generate SE, by forcing the film boiling to collapse, at non self-triggered materials like aluminium and zinc. From Y. Abe et al^[4] experiments includes external triggering of aluminium and zinc, it was found that **0.5 [MPa]** pressure pulse triggers both materials.

A vast experimental data from different studies collected and analysed. Table 1 shows the main experiments parameters from the studies^[1-4] used in the current study.

Table 6: [1-4] experiments main parameters.

Experiment	Mode of contact	Materials (melting point [°C])	Melt mass [kg]	Jet dia. [mm]	Jet velocity [m/s]	Jet temp. [°C]	Melt temp. [°C]
G. Widenfeld ^[1]	CI	*Sn(231.9), Al(660.3), Zn(419), different Sn- Zn mixtures(198.5,300,350)	1.4	0.5-5	9-25	25,31	240-750
Y .Sibamoto et al ^[2]	CI	Pb-Bi eutectic mixture (125)	2	6	5-8	25-90	230-550
Y. Perets ^[3]	CI	Sn(231.9)	1	0.7	13-14	25-98	240-590
Y. Abe et al ^[4]	FFMD	Sn(231.9), Al**(660.3), Zn(419)	$5 \cdot 10^{-3}$	NA	50mm free fall	Water pool temp 25,57	Al:710,746 Zn:575,590

* Only Sn experiments were analysed. ** Only Al and Zn experiments were analysed.

The experiments results from studies [1-4] compared by: melt point temperature, water to melt thermal inertial ratio (β), surface tension, kinematic viscosity, jet diameter and velocity and jet theoretical breakup length. Examination of this vast field of parameters is possible by using dimensionless numbers that describes the material properties, jet characteristics and the initial temperatures. The dimensionless numbers, which were used to describe the phenomena, are Weber ($We = \frac{\rho v^2 d}{\sigma}$), Froude ($Fr = \frac{v}{d_{jet} g^{1/2} (\rho_{jet} - \rho_{melt})^{1/2}}$), $\frac{T_m}{T_{MP}}$ and β . With this new approach, further insights concerning the SE trends and boundaries exposed.

RESULTS

Drawing TIZ map for studies [1] and [3], in tin-water system, shows that TIZ boundaries relevance for one study are not matching to the other. In Fig.1, TIZ map shows melt temperature as function of water temperature, the "x" sign represents no SE occurrence and a full diamond is a SE event. The boundaries divided to theoretical boundaries as mentioned before (T_{MFB} , T_{MP} , and T_{HN}) and empirical boundaries. Y. Perets^[3] found empirical boundary (marked as RBTIZ - right boundary TIZ) for tin – water system. Figure 1 shows that SEs above the RBTIZ may occur as was found at G. Widenfeld^[1] experiments using higher jet diameters and velocities.

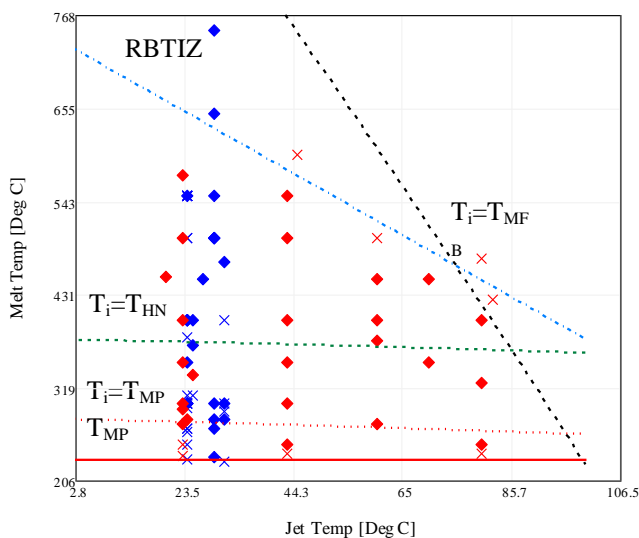


Fig. 5. Thermal interaction zone for tin-water system in CI mode from [1, 3] experiments.

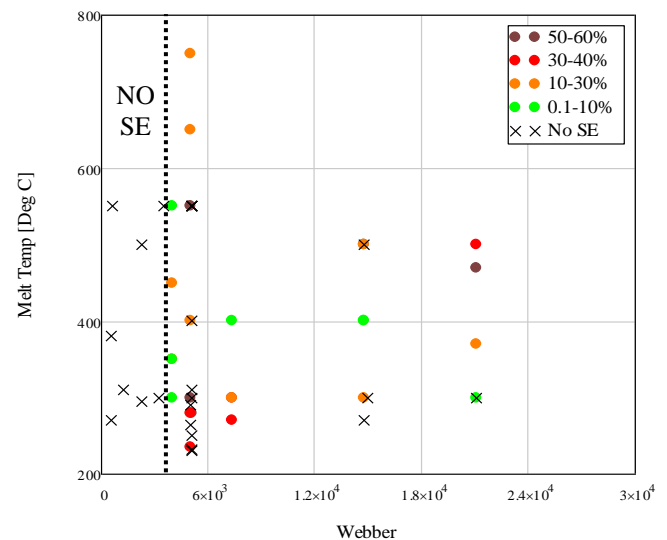


Fig.5. Tin melt percentage splattered from the crucible versus melt temperature and Weber number from G. Widenfeld^[1] experiments. Jet temperature is around **25°C**.

Further, it was found that SE occurs even beneath the melting point at the interface temperature in both experiments, suggesting that jet inertial forces influencing the triggering mechanism.

Using a combination of dynamic and TIZ maps may draw, more accurate initial conditions leading towards SE event. Therefore, further testing of parameters such as Weber and Froude numbers shows that dynamic properties have to be treated. Fig.2. Shows the melt initial temperature of tin, versus Weber number. "x" signs indicate no SE event and the colour scheme representing the percentage of melt splattered from the crucible, that may implies on the explosion intensity. No explosions appeared below jets with Weber number of 3900, indicating that a minimal inertial force is required to generate SE. The theoretical breakup length matching this Weber value is 7.5 mm for tin – water system. From Y. Perets^[3] images of the melt surface, it was found that at low flow rates the water jet could not penetrate the melt surface. Examinations of the splattered melt percentage (as shown in fig.2) shows that SE intensity is not a function of jet dynamic properties or melt temperature.

A further examination of β value was done. Figure 3 shows melt to melting point ratio as function of β for studies [1-4]. It was found (see Fig.3.) that the non-self-triggered materials (aluminium and zinc) sharing low β values (0.014) and melting points above HN temperature. While materials (tin and lead bismuth mixture) with β higher then 0.04 and melting point below the HN temperature generates spontaneous SE. Further experimental data is required in order to confirm that β may consider as occurrence conditions.

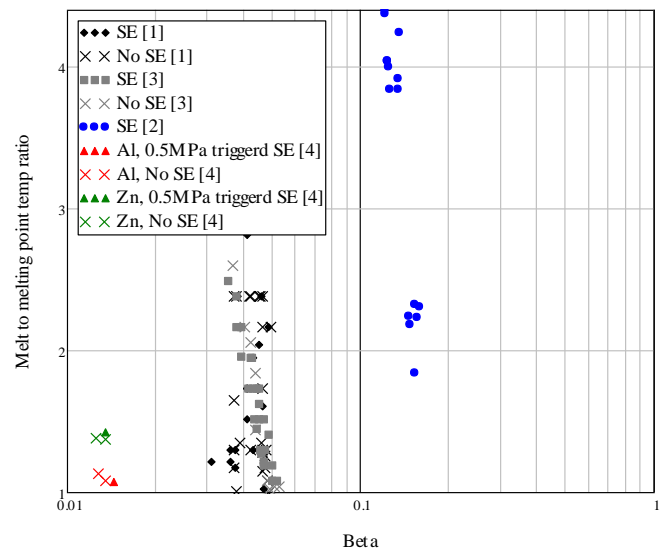


Fig.3. Different regions of triggering mechanism map for different materials

Conclusions

In this study, data from four different studies was cross-referenced by comparing jet parameters, initial temperatures and material properties for different melts. It was found that TIZ boundaries varied with the jet dynamic properties. Weber number was found as a minimum limit for dynamic occurrence condition. This study shows that analyse the SE occurrence conditions solely by the TIZ map, will not be accurate for CI mode. From dynamic properties, analyse together with the TIZ map the ability to predict SE events increases. Further experimental data required to understand the complete effects of jet properties on the occurrence conditions.

REFERENCES

- [1] G. Widenfeld, Y. Aharon, R.Harari, I. Hochbaum and Y. Weiss, Steam Explosion Induced by Water Injection onto Molten Metal, 29th Israel Conf. of Mechanical Engineering, 2003.
- [2] Y .Sibamoto, Y. Kukita And H. Nakamura. "Small-scale Experiment on Subcooled Water Jet Injection into Molten Alloy by Using Fluid Temperature-Phase Coupled Measurement and Visualization." *Journal of NUCLEAR SCIENCE and TECHNOLOGY*, Vol. 44, No. 8, p. 1059–1069 (2007)
- [3] Perets, Yaron. Thermal Reaction By Impinging Coolant on Liquid Metal - Vapor Explosion. Thesis, Beer Sheva: Ben Gurion University of the Negev, Department of Mechanical Engineering, 2003.
- [4] Yutaka Abea, Hideki NARIAI and Yukihiko HAMADA. "The Trigger Mechanism of Vapor Explosion." *Journal of NUCLEAR SCIENCE and TECHNOLOGY*, 39, no. 8 (August 2002): 845-853.

Posters (Wednesday, February 12, 2014 15:30)

Geological Disposal of Radioactive Waste

A. Dody, O. Klein Ben David

NRCN, Israel

INTRODUCTION

Disposal of radioactive waste imposes complicated constraints on the regulator to ensure the isolation of radioactive elements from the biosphere. The IAEA (1995) states that "The objective of radioactive waste management is to deal with radioactive waste in a manner that protects human health and the environment now and the future without imposing undue burdens on future generation". The meaning of this statement is that the operator of the waste disposal facilities must prove to the regulator that in routine time and in different scenarios the dose rate to the public will not exceed 0.3 mSv/y in the present and in the future up to 10,000 years.

For low and intermediate level waste (LILW), these constraints can be accommodated using near surface repositories. However, for high level waste (HLW), transuranics waste (TRU) and spent fuel; these conditions cannot be fulfilled by near surface repositories, which depend strongly on the nature of their engineered barriers, climate and the intensity of geomorphology processes. Such construction (e.g. cements, steel etc.) have a life span of hundreds to thousands of years. In the case of HLW the activity after such periods of time can still be many orders of magnitudes above the clearance level. Additionally, The IAEA recommends an institutional control period of 300 years after the disposal site's closure, including passive and active monitoring. This period may be too short regarding the long lived and toxic radionuclides (RNs). Moreover, climate changes and erosion processes can impose strong constraints on the life-span of engineered barriers and on contamination migration from them.

Thus the IAEA (2006) recommended deep geological disposal as long-term solution for HLW, such as TRU and spent fuel. A geological disposal is defined as: "isolating long lived radioactive waste from human environment by placing them deep underground in repositories located in host rocks characterized by high stability and low or no groundwater flow" (IAEA, 2003). A geological repository is considered as the best approach to ensure the isolation of the HLW from the biosphere. Construction, operation and closing of geological repository require considerable technical and scientific background in the design, engineering and safety assessment of such a facility (IAEA, 2003).

The depth of a geological formation and its characteristics are the ultimate barriers between the waste and the environment in the long run. Thus, to accommodate these characteristics a relevant geological formation must have: 1) Low hydraulic conductivity. 2) Low fractures and joint density. 3) High distribution coefficient (K_d) for RN contaminants. 4) Low or no groundwater flow.

There are three major lithologies that were investigated and considered as adequate for a deep disposal site. Clay-rich formations are considered adequate principally because of their very low permeability and high adsorption coefficients (K_d) for most RNs. Salt rock, when under hyper saline solution conditions, is insoluble and highly impermeable. Finally, crystalline rocks (e.g. granite), when unfractured, also have low permeability and relatively high K_d .

IMPLEMENTATION OF GEOLOGICAL DISPOSAL AROUND THE WORLD

Today, no country has an authorized and operating geological disposal facility. The main obstacles in the regulation process arise public acceptance issues and stakeholders approval, together with the regulatory and authorization applied requirements. Specifically, the demand for retrievability of the buried waste in the future, in some countries (e.g. France) imposes much safety, regulatory and engineering challenges. Additionally, far future (i.e. 10^5 y) modeling and speculation create large uncertainties and difficulties in communicating with the public.

Nevertheless, most of the western countries have taken significant steps towards the implementation of such repository, examples of which are given below.

USA: Waste Isolation Pilot Plant (WIPP) is operating in New Mexico at 655 m depth in a 600 m thick salt formation that has been stable for more than 2000 million years. It is defined as storage and not as final

burial site. The site is aimed for military TRU waste only. On the other hand, 30 years of research into the implementation of geological disposal site in Yucca Mountain, Nevada in a tuff formation have been ended in extinguishing the project and in search for a new location for the site/France: The French National Radioactivity Management Agency (ANDRA) is constructing a deep disposal site at about 500 m depth in clay-argillite of Callovo-Oxfordian formation. At the Meuse/Haute-Marne Underground Research Laboratory (URL) located at Bure (300 km east of Paris). The site is expected to become operational in 2020.

Belgium: A clay formation (boom clay) at a depth of about 240 m in north east of the country is being considered as a possible disposal site, but so far no final decision has been made.

Germany: The Gorleben salt dome was investigated for its feasibility as a repository since the mid-1980s. In 2000 a moratorium was imposed on the Gorleben site and it was re-opened for investigation in 2010. Decision about the future use the site is expected in 2020.

Sweden: A site in granite bedrock about 500 m below surface was located at Fosmark. The site is expected to be opened in 2025 and to be in full use in 2027.

Finland: Finland is constructing a national repository named Onkalo in a crystalline bedrock formation. The repository is located in Olkiluoto at a depth of 400-500 m. An underground rock characterization facility was established at the site. The repository is expected to be operational by 2020.

Switzerland: Two active undergrounds research labs were established. One in an Opalinus clay formation (Mont Terri) and one in granite rock (Grimsel). No decision has been made on the final location the repository.

Other countries: Russia and Hungary have sited specific locations and defined the geological formation and aimed for suitable kind of disposal. The UK and Canada are in the stage of approaching local communities for consent to entrain geological repository.

In summary, it can be seen that most western countries involved in nuclear activity are in the process of locating, investigation and acquiring public acceptance in their quest towards geological disposal implementation.

THE ISRAELI CASE – PRELIMINARY RESULTS

The small size of Israel, the large population density in the central and northern parts and the proximity to an active fault zone (the Dead Sea Rift) make the choice of suitable site difficult. Additionally, the common target rocks for geological disposal (e.g. salt, clay, and granite) are unavailable in Israel in thick, depth and un-fractured formations.

The Yamin Plateau (YP) in the north east of the Negev holds the Israeli national site for radioactive waste since the 1969th. LLW is disposed in near surface trenches. However, other waste forms (i/e. spent fuel) are stored as being inadequate for near surface disposal. The government of Israel gave the NRCN through the IAEA the mandate to examine the possibility of locating a geological waste disposal site in YP. The marl and chalk lithologies of the Mount Scopus Group are being examined for their suitability to serve as host rocks for geological repository. These lithologies are characterized by low hydraulic conductivity and high retardation capacity for RNs. It should be noted the Judea and Kurnub aquifers (Fig. 1) reside 200-300 m below the target formation.

Four boreholes of 3" diameter perpendicular to the geological structure (Figs. 1, 2) were drilled down to 300 m depth in order to investigate the stratigraphy, depth and thickness of the target units. The presence, direction and joints' density were studied using a unique camera (TeleViewer). Cores were sent for geotechnique analyses to check the parameters of mass rock quality. In-situ inspections within boreholes were conducted to measure the hydraulic conductivity values, using "double packer" technique, and the bulk densities of the rocks unit through P and S seismic velocities. Additionally, primary estimation of the rocks retardation capacity for the expected contamination (through their stimulants) was done, yielding satisfactory values. So far, the main finding is that none of these measured parameters negate the possibility of geological waste disposal in those deep formations, but more research is needed

REFERENCES

- IAEA, 2006. Geological Disposal of Radioactive Waste. SR. No. WS-R-4.
- IAEA. 2003. Scientific and Technical Basis for Geological Disposal of Radioactive Wastes. Technical Reports Series No. 4.
- IAEA, 1995. Principles of Radioactive Waste Management. Safety Series No. 111-F.

Safety Issues of the LORELEI Test Device

R. Sarusi⁽¹⁾, L. Ferry⁽²⁾, D. Drapeau⁽²⁾, M. Szanto⁽³⁾, N. Moran,
M. Katz⁽¹⁾, Y. Weiss⁽¹⁾

(1) NRCN, P.O.Box 9001 Beer Sheva, , Israel

(2) CEA, Cadarache, France

(3) Rotem Industries LTD, Mishor Yamin, D.N Arava 86800 Israel

1. INTRODUCTION

The LORELEI (Light-Water One-Rod Equipment for LOCA Experimental Investigation) test device is dedicated for the study of fuel during a Loss of Coolant Accident (LOCA).

The safety of this project is been done with a collaboration between the Israeli and the French teams and will have to be authorized by the French regulation authority (ASN).

The main challenges in safety are:

1. Preparing a safety reports according to the French regulations and standards.
 2. Learning and obtaining knowledge on the safety philosophy of experimental devices in French.
2. The safety approach include:

2.1. Identification of all the dangers from the device in all the working situations:

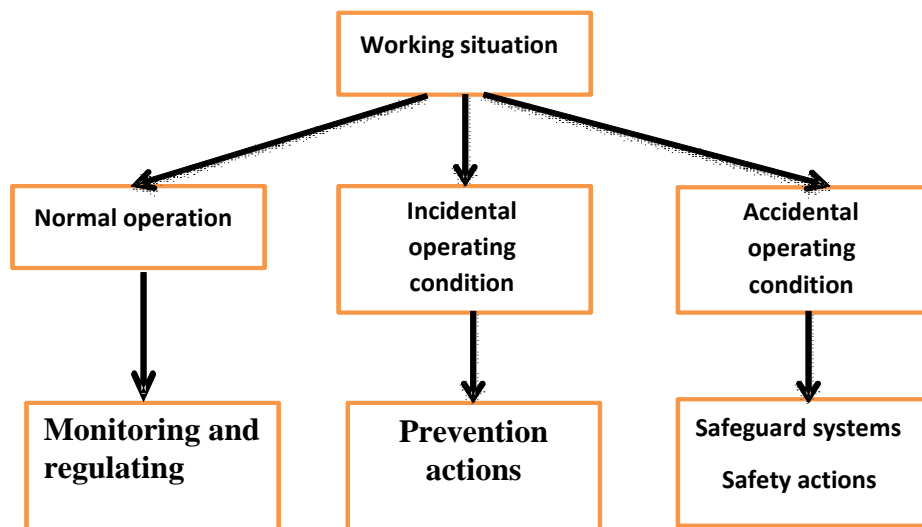


Figure 1: Classification of working situation

2.2. Identification of the number of barriers needed:

2.2.1. The term barrier refers to a physical envelope of the device design to contain the effects of “dangerous sources” due to the device itself.

2.2.2. The recommended approach aims at identifying the barriers for the in-Core section of the device which is directly exposed to flux and/or Capable of leading to interactions with the reactor core.

2.3. Identification of the anti fly-off systems needed:

2.3.1. A hypothetical total failure of the in-core section of the device- is considered as the retraction of the in-core device which can lead to a reactivity insertion depending on the configuration.

2.3.2. Consequently, the reactivity of the device and any possible causes of fly-off must be examined.

3. Safety analysis is based on FMEA (Failure Mode and Effect Analysis) method:

- 3.1. A systematic technique that takes all the components of the device and analyzed them in normal and accidental situations.
- 3.2. Bottom- up technique.
- 3.3. Evaluate the means (defense lines) that needed in each component failure.

4. Defense in Depth approach is adopted:

	Level of defence in depth	Objective of the level	Essential means	Associated Plant condition categories
Original design of the plant	Level 1	Prevention of abnormal operation and failure	Conservative design and high quality in construction and operation	Normal operation
	Level 2	Control of abnormal operation and failure	Control, limiting and protection systems and other surveillance features	Anticipated operational occurrences
	Level 3	Control of accident within the design basis	Engineered safety features and accident procedures	Design basis accidents (postulated single initiating events)
Beyond design situations	Level 4	Control of severe plant conditions that were not explicitly addressed in the original design of currently operating plants owing to their very low probabilities	Complementary measures and accident management	Multiple failures Severe accidents
Emergency planning	Level 5	Mitigation of radiological consequences of significant releases of radioactive materials	Off-site emergency response	-

In SF-1 published in 2006, the IAEA stressed that independency effectiveness of the different levels of defence is a necessary element of DiD concept.

Table 1: Defense in Depth approach

- 5. The approach of the experimental devices is deterministic.
- 6. There are 5 stages to prepare the hazard analysis:
 - 6.1. Classification of the components to ISE1...ISE3 – table of classification.
 - 6.2. Evaluation the consequences of a component failure (according to his functions)- the result is the working situation- table WS1...WS4.
 - 6.3. Checking if the safety classification of the components (ISE1...ISE3) is relevant with the classification of the working situation WS1...WS4.
 - 6.4. Determination of the means (options) needed for the device according to the Defense in Depth criteria (level 1...level 4).
 - 6.5. Possible actions from LORELEI device for the control of the experiment

The analysis scheme

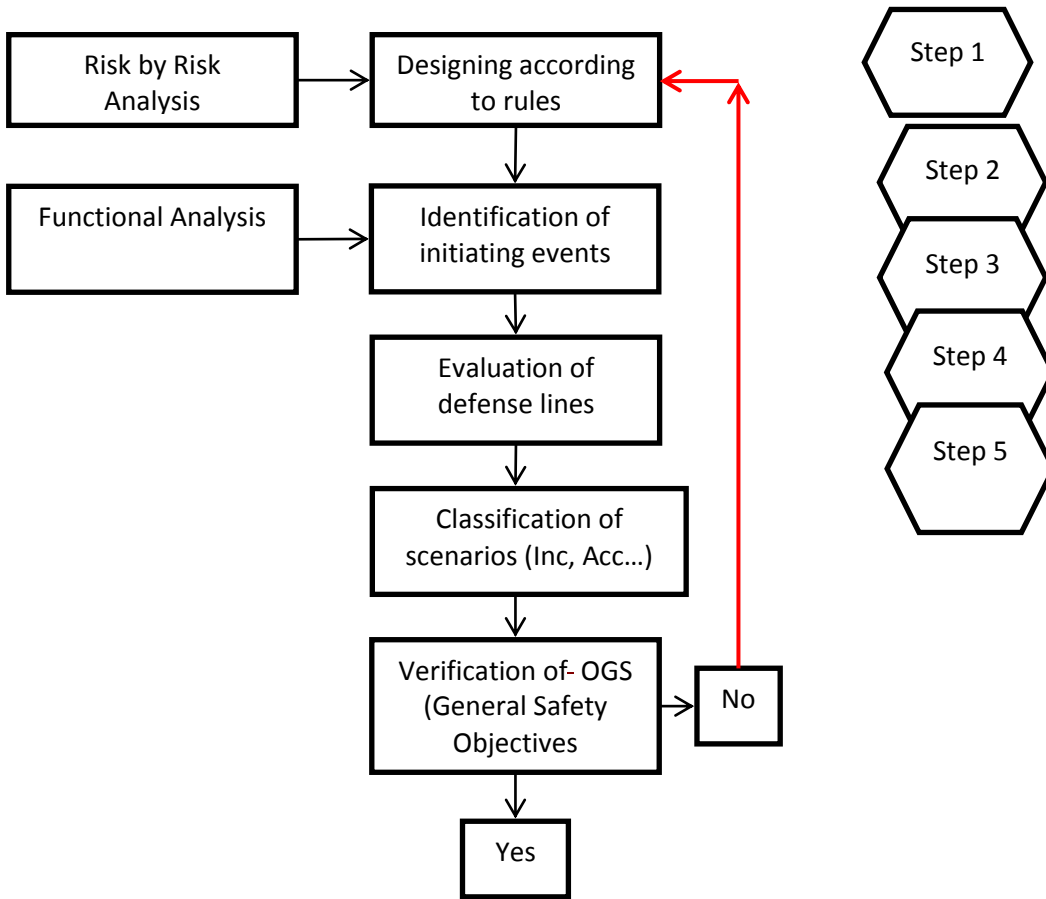


Figure 2: Hazard Analysis scheme

